New Jersey Institute of Technology
Digital Commons @ NJIT

Dissertations | Electronic Theses and Dissertations

Spring 5-31-1997

Design, simulation, fabrication and testing of microprobes for a new MEMS wafer probe card

Yanwei Zhang
New Jersey Institute of Technology

Follow this and additional works at: https://digitalcommons.njit.edu/dissertations

Part of the Electrical and Electronics Commons

Recommended Citation
Zhang, Yanwei, "Design, simulation, fabrication and testing of microprobes for a new MEMS wafer probe card" (1997). *Dissertations*. 1035.
https://digitalcommons.njit.edu/dissertations/1035

This Dissertation is brought to you for free and open access by the Electronic Theses and Dissertations at Digital Commons @ NJIT. It has been accepted for inclusion in Dissertations by an authorized administrator of Digital Commons @ NJIT. For more information, please contact digitalcommons@njit.edu.

Copyright Warning & Restrictions

The copyright law of the United States (Title 17, United States Code) governs the making of photocopies or other reproductions of copyrighted material.

Under certain conditions specified in the law, libraries and archives are authorized to furnish a photocopy or other reproduction. One of these specified conditions is that the photocopy or reproduction is not to be "used for any purpose other than private study, scholarship, or research." If a, user makes a request for, or later uses, a photocopy or reproduction for purposes in excess of "fair use" that user may be liable for copyright infringement,

This institution reserves the right to refuse to accept a copying order if, in its judgment, fulfillment of the order would involve violation of copyright law.

Please Note: The author retains the copyright while the New Jersey Institute of Technology reserves the right to distribute this thesis or dissertation

Printing note: If you do not wish to print this page, then select "Pages from: first page # to: last page #" on the print dialog screen

NJIT
New Jersey's Science & Technology University

The Van Houten library has removed some of the personal information and all signatures from the approval page and biographical sketches of theses and dissertations in order to protect the identity of NJIT graduates and faculty.

ABSTRACT

DESIGN, SIMULATION, FABRICATION AND TESTING OF MICROPROBES FOR A NEW MEMS WAFER PROBE CARD

by
Yanwei Zhang

A new type of MEMS cantilever wafer probe card consists of an array of microcantilevers individually actuated by bimorph heating to make contact with the test chip was designed and fabricated. This probe card is called the CHIPP (Conformable, High-Pin count, Programmable) card and can be designed to contact up to 800 I/O pads along the perimeter of a 1 cm^2 chip with a microprobe repeat distance of ~50 μm. Each microcantilever had an internal heater and a separate electrode carrying the signal under test and contained four separate layers plus a fifth material for the contact tip region.

Different versions of micro-actuators have been designed and made in this Ph.D. research. Ohmic contacts were made with the lowest contact resistance of 250 mΩ. The deflection efficiency varied from 5.23 to 9.6 μm/mW for cantilever length from 300-500 μm. The maximum reversible deflection was in the range of 270 μm. Video recordings made inside the SEM clearly show that ohmic contact was made to a stationery tungsten electrode. A full dynamic deflection (180 μm) for a 50 x 500 μm cantilever occurred in response to input frequency up to nearly 50 Hz. The motion was damped at higher frequencies, with a strong resonance (for a 50 x 500 μm device) at 8160 Hz. Heat loss for devices operating in air was found to be substantially higher than for vacuum operation with a heat loss ratio of about 2/1 for a heater inside the structure; and 4.25/1 for a structure with the heater as an outer layer of the cantilever.

DESIGN, SIMULATION, FABRICATION AND TESTING OF MICROPROBES FOR A NEW MEMS WAFER PROBE CARD

by
Yanwei Zhang

A Dissertation
Submitted to the Faculty of
New Jersey Institute of Technology
in Partial Fulfillment of the Requirement for the Degree of
Doctor of Philosophy

Department of Electrical and Computer Engineering

May 1997

Copyright © 1997 by Yanwei Zhang
ALL RIGHTS RESERVED

APPOVAL PAGE

DESIGN, SIMULATION, FABRICATION AND TESTING OF MICROPROBES FOR A NEW MEMS WAFER PROBE CARD

by

Yanwei Zhang

Dr. Robert B. Marcus, Dissertation Advisor — Date
Professor of Electrical and Computer Engineering, NJIT

Dr. William N. Carr, Committee Member — Date
Professor of Electrical and Computer Engineering,
and Professor of Physics, NJIT

Dr. Ken K. Chin, Committee Member — Date
Professor of Physics and Director of NJIT/Rutgers-Newark
Joint M.S./Ph.D. Programs, NJIT

Dr. Peter Engler, Committee Member — Date
Associate Professor of Electrical and Computer Engineering, NJIT

Dr. Nuggehalli M. Ravindra, Committee Member — Date
Associate Professor of Physics, NJIT

APPOVAL PAGE
(Continued)

DESIGN, SIMULATION, FABRICATION AND TESTING OF MICROPROBES FOR A NEW MEMS WAFER PROBE CARD

by

Yanwei Zhang

Dr. Roy H. Cornely, Committee Member | Date
Professor of Electrical and Computer Engineering
and Director of Drexler Thin Films Microelectronics Laboratory, NJIT

BIOGRAPHICAL SKETCH

Author: Yanwei Zhang

Degree: Doctor of Philosophy

Undergraduate and Graduate Education:

- Doctor of Philosophy in Electrical Engineering
  New Jersey Institute of Technology, Newark, NJ, 1997

- Master of Science in Electrical Engineering
  Chinese Academy of Space Technology, Beijing, China, 1985

- Bachelor of Science in Materials Science
  Lanzhou University, Gansu, China, 1982

Major: Electrical Engineering

Presentations and Publications:

Yanwei Zhang, Yongxia Zhang, Dan Morrow,
Dan Worsham and Robert B. Marcus,
"A New MEMS Wafer Probe Card",
Proceedings of IEEE 10th International workshop on MEMS,
pp. 395, Nagoya, Japan, January 26-30, 1997.

Yongxia Zhang, Yanwei Zhang, T. S. Sriram
and Robert B. Marcus,
"Formation of Single Tips of Oxidation-Sharpened Si",
Applied Physics Letter, vol. 69, pp. 4260, December, 1996.

Yongxia Zhang, Yanwei Zhang and Robert B. Marcus,
"Formation of Single Tips of Atomically Sharp Silicon",
Proceedings of 43rd America Vacuum Society National Symposium,
Philadelphia, pp. 44, October 14-18, 1996.

Yanwei Zhang, Yongxia Zhang, and Robert B. Marcus,
" 'CHIPP' Probe - A New MEMS Wafer Probe Card",
Emerging Technologies Symposium, Princeton, New Jersey, October 26, 1995.

Yongxia Zhang, Yanwei Zhang, and Robert B. Marcus,
"A New High Resolution AFM Thermal Probe",
Emerging Technologies Symposium, Princeton, New Jersey, October 26, 1995.

Yanwei Zhang, and Paul D. Ronney,
"Lewis Number Effects on Flame Spreading Over Thin Solid Fuels",
Combustion and Flame, vol. 90, pp. 71, 1992.

This dissertation is dedicated
to my wife, Su Wang
to my son, Chao Zhang

ACKNOWLEDGMENT

I wish to express my sincere gratitude to my advisor, Professor Robert. B. Marcus , for his great guidance, friendship, and moral support throughout whole research project. Without his support I could never complete this hard research project.

Special thanks to the other members of committee: Dr. William Carr, Dr. Peter Engler, Dr. Ken K. Chin, Dr. Nuggehalli M. Ravindra, and Dr. Roy H. Cornely for their careful review, productive comments and helpful discussions.

I would also like to thank Dr. Dentcho Ivanov, Mr. John Koons and Mr. Ken O'Brien for all their helps in the Microelectronics Clear Room and Prof. R. Levy for use of his RF sputtering laboratory, Prof. W. Carr for use of his probe station and Prof. K. Chin for use of his probe station and deposition system.

I am grateful to Yongxia Zhang and other fellow students who shared their valuable ideas and experiences with the author.

Finally I would like to thank my family and friends for their continuous encouragement and best wishes, especially my wife, whose love, care and support made this work possible.

TABLE OF CONTENTS

Chapter **Page**

1 INTRODUCTION 1

1.1 Probe Card: Function 1

1.2 This Research Objective 4

2 MEMS MICROACTUATION 5

2.1 Thermal Actuation 5

2.1.1 Bimorph Actuation 6

2.1.2 Thermal Driven Cantilever Flexure 7

2.2 Electrostatic Actuation 9

2.2.1 Electrostatic Cantilever Actuation 9

2.2.2 Electrostatic Microbridge Actuation 11

2.2.3 Magnetic and Piezoelectric Actuation 12

3 CONCEPT AND DESIGN OF MEMS PROBE CARD 14

3.1 CHIPP Probe Card 14

3.1.1 Concept of CHIPP Probe Card 14

3.1.2 Design of Prototype CHIPP Probe Card 17

3.2 CHIPP Microprobe 20

3.2.1 Physical Design of CHIPP Microprobe 20

3.2.2 Heater Design of CHIPP Microprobe 27

3.3 Ohmic Contact Issues and Solutions 32

3.3.1 Contact Forces Required 32

TABLE OF CONTENTS
(Continued)

Chapter **Page**

3.3.2 Ohmic Contact 32

4 MODELING AND SIMULATION 36

4.1 Analysis of Bimorph Structures 36

4.1.1 Analysis of Bimorph Cantilever with Two Free Ends 36

4.1.2 Analysis of Bimorph Cantilever with Left End Free and Right End Fixed. 39

4.1.3 Force Analysis of One End Fixed Cantilever 40

4.1.4 Equivalent Stiffness for Multi-Cantilever Layers 42

4.2 Simulation of Motion of Bimorph Cantilever Structure 44

5.2.1 Basic Assumption 44

5.2.2 Simulation of the Effect of Cantilever Thickness 45

5.2.3 Simulation of the Deflections at the Probe Tip 47

5.2.4 Forces Applied by Cantilever Tips 52

5 FABRICATION 58

5.1 Fabrication of Al-SiO_2 Type Probe Card 58

5.2 Fabrication of W-SiO_2 Type Probe Card 65

5.2.1 Gold and Tungsten Tip Structures 65

5.2.2 Conducting Diamond Tip Structure 68

5.3 Mask Design 73

5.4 Adhesion Consideration and Experiments 73

TABLE OF CONTENTS
(Continued)

Chapter **Page**

6 RESULTS AND DISCUSSION 76

6.1 General Results of Fabrication of the CHIPP Probe Card........ 76

6.2 Switch Characteristics of CHIPP Microprobe........ 85

6.2.1 Rest Position of the Microprobe Tips 85

6.2.2 Deflection of the Microprobe........ 90

6.2.3 Response Frequency and Time of the Microprobe 96

6.3 Ohmic Contact of CHIPP Microprobe........ 100

6.3.1 Ohmic Contact 100

6.3.2 Contact Force 107

6.4 Heat Loss of CHIPP Microprobe 111

6.5 Failure Analysis and Device Improvement 116

7 CONCLUSIONS 119

8 REFERENCES........ 121

LIST OF TABLES

Table **Page**

3.1 Physical characteristics of microprobe cantilever layers..23

3.2 Dimension parameters of component layers of CHIPP microprobes......................24

3.3 Dimension parameters of CHIPP microprobes..31

3.4 Dimension parameters of tips of CHIPP microprobes...35

6.1 Structure parameters of fabricated CHIPP probe card 78

6.2 Rest position of the tips for different microprobes 87

6.3 Data of thermal driven cantilevers 91

6.4 Measured contact resistance of CHIPP microprobes.. 100

6.5 Force efficiency α_p for various values of W and L for bimorph with 1 μm Al and 1 μm SiO_2 108

LIST OF FIGURES

Table		Page
2.1	Bimorph cantilever actuation structure	7
2.2	Horizontal heat-drive actuator	8
2.3	Basic electrostatic cantilever actuator	11
2.4	Resonant microbridge/switch structure	12
3.1	Microprobe making ohmic contact with the surface of a test chip	16
3.2	Illustration of prototype CHIPP probe card showing microprobes positioned about a center opening. The test chip is mounted face-down over the probe card	18
3.3	Illustration of arrangement of MEMS microprobes for contacting interior pads	19
3.4	Illustration of microprobe with heater inside the cantilever	25
3.5	Illustration of microprobe showing heater as the bottom layer of the cantilever	26
3.6	A bimorph cantilever structure with heater on the bottom layer showing the heat loss from the heater directly to air	28
3.7	Details of heater inside the cantilever showing heat flow	29
3.8	Heater designs used in CHIPP microprobe	30
3.9	Illustration of tip of CHIPP microprobe	34
4.1	Deflection of a bimorph cantilever with uniform heating	37
4.2	Cantilever deflection with left end free and right end fixed	40
4.3	External forces applied near the tip of the cantilever with one end fixed	42
4.4	Equivalent cross section of CHIPP microprobe with three layers	43
4.5	Cantilever tip deflection as a function of ratio of bimorph thickness t_{oxide}/t_{metal} for L=400 μm, $\Delta T=100\ ^{o}C$, and $t_{metal}=1$ μm	46
4.6	Tip deflection as a function of temperature rise ΔT for Al-SiO_2 cantilever at L=400 μm, and $t_{oxide}/t_{metal}=0.5$ and three different Al thicknesses	48

LIST OF FIGURES
(Continued)

Figure **Page**

4.7 Tip deflection as a function of temperature rise ΔT for Al-Si cantilever at L=400 μm, and t_{oxide}/t_{metal}=0.3 and three different Al thicknesses 49

4.8 Tip deflection as a function of temperature rise ΔT for Cu-SiO_2 cantilever at L=400 μm, and t_{oxide}/t_{Cu}=0.6 and three different Cu thicknesses 50

4.9 Tip deflection as a function of temperature rise ΔT for W-SiO_2 cantilever at L=400 μm, and t_{oxide}/t_W=1.1 and three different W thicknesses 51

4.10 Forces applied by tip as a function of temperature rise ΔT for Al-SiO_2 cantilever with three Al thicknesses 53

4.11 Forces applied by tip as a function of temperature rise ΔT for Al-Si cantilever with three Al thickness 54

4.12 Forces applied by tip as a function of temperature rise ΔT for Cu-SiO_2 cantilever with three Cu thickness 55

4.13 Forces applied by tip as a function of temperature rise ΔT for W-SiO_2 cantilever with three W thickness 56

4.14 Forces applied by tip as a function of the cantilever width for four different bimorph cantilevers 57

5.1 Fabrication flows for a prototype probe card using Al-SiO_2 cantilever with gold tip 64

5.2 Fabrication flows for a prototype probe card using W-SiO_2 cantilever with gold and tungsten tips 66

5.3 Fabrication flows for a prototype probe card using W-SiO_2 cantilever with conducting diamond tip 72

6.1 A prototype CHIPP probe card mounted in a ceramic header (6.2x) 79

6.2 SEM photo showing two adjacent 50 x500 μm microprobes with Al-SiO_2 bimorph structure (150x) 80

6.3 SEM photo showing three adjacent 40 x 400 μm microprobes with Al-SiO_2 bimorph structure(149x) 81

LIST OF FIGURES
(Continued)

Figure **Page**

6.4 SEM photo showing two adjacent 50 x 300 μm microprobes with Al-SiO_2 bimorph structure and gold tips(150x) 82

6.5 An array of four adjacent 30 x 200 μm microprobes with Al-SiO_2 bimorph structure and gold tips(100x) 83

6.6 An array of four adjacent 30 x 200 μm microprobes with W-SiO_2 bimorph structure and conducting diamond tips (48.5x) 84

6.7 Cantilever tip rest position as a function of cantilever length with four different cantilever structures. Zero is the probe card surface 88

6.8 The rest position of microprobe tips as a function of cantilever thickness with three different cantilever sizes. Zero is the probe card surface 89

6.9 Tip deflection vs. applied power with Al (1.0 mm)-SiO2 (1.0mm) bimorph cantilever. Inset shows cantilever widths and lengths for five devices 92

6.10 Tip deflection vs. Applied power with W (1.0 mm)-SiO2 (1.2mm) bimorph cantilever. Inset shows cantilever widths and lengths for three devices 93

6.11 SEM side view of a 60 x 500 μm Al-SiO_2 cantilever at unpowered rest state(b) and actuated to a flat position (a). Photo were taken from a video tape during dynamic testing 94

6.12 SEM side view of a 40 x 400 μm Al-SiO_2 cantilever at unpowered rest state(b) and actuated to a upward position (a). Photo were taken from a video tape during dynamic testing 95

6.13 Dynamic deflection of a Al-SiO_2 cantilever as a function of input signal frequency with square wave input 98

6.14 Dynamic deflection of a Al-SiO_2 cantilever as a function of input signal time with fixed square wave input of 1 Hz. This is the same cantilever described in Figure 6.13 99

6.15 A gold contact tip at a Al-SiO_2 cantilever with 0.5 μm gold film 102

6.16 A conducting diamond tip at a W-SiO_2 cantilever 103

LIST OF FIGURES
(Continued)

Figure **Page**

6.17 SEM photo showing crystals of conducting diamond (5000x) 104

6.18 A SEM photo showing a side view of an Al-SiO2 cantilever probe unpowered, at rest, with the tungsten electrode (bright) above tip 105

6.19 A SEM photo showing same cantilever with Figure 6.18, fully deflected and making ohmic contact with the tungsten electrode (electrode is dark due to "voltage contrast") 106

6.20 Force as a function of tip motion for various combination of aluminum and SiO_2 cantilever widths and lengths 109

6.21 Force as a function of applied power for various combination of aluminum and SiO_2 cantilever widths and lengths 110

6.22 Photo showing the inside heater structure 112

6.23 Tip deflection vs. applied power inside SEM vacuum and in air for Al-SiO_2 cantilever with heater inside. Cantilever length L=400μm, width W=50 μm and t_{Al}=1.5 μm 113

6.24 Photo showing the outside heater structure 114

6.25 Tip deflection vs. applied power inside SEM vacuum and in air for Al-SiO_2 cantilever with heater on the bottom. Cantilever length L=500μm, width W=40 μm and gap D=10 μm 115

6.26 SEM photo showing a tip immediately after breaking 117

6.27 SEM photo showing the same tip as Figure 6.26 a 33 ms later 118

CHAPTER 1

INTRODUCTION

1.1 Probe Card: Function

Wafer probing technology has been under development and use for several decades [1],[2]. It began with manual probe stations and has expanded to semi-automatic probe card tools for analytical work. Manual probe stations usually have three to four probes to contact the pads of test devices. Ohmic contact is formed through manually moving the probe to scrape through surface oxide films and make contact with the contact pads. Because it is difficult to control and work with a large number of test probes, test work using this probe station is time consuming and even impossible if many pads need to be probed.

As device sizes decreased and device pads increased, manual type probe stations no longer met basic the requirements of the semiconductor industry, and the concept of a probe card was developed. The first probe card, called a needle/epoxy ring probe card was developed and patented by Rucker & Kools (a company makes probing stations) in 1969 [2]. The early probe card was based on an epoxy ring technology in which a few tens to hundreds of tiny cantilever needles were manually mounted on a probe card through an epoxy ring and arranged according to the pad positions of the test chip. The probe card is designed with I/O connection which can be connected directly to a control head of the mechanical probing station. The ohmic contact between needles on probe card and pads on test chip can be obtained through either probe card or test chip movement. As soon as the connections are made, testing could be started through a switch matrix to

control inputs and outputs. The epoxy ring probe card realized semi-automatic LSI testing and greatly increased test ability and efficiency.

As VLSI technology developed smaller and smaller semiconductor devices, this probe card technology has fallen behind. Test and wafer handling capabilities have progressed at a very rapid pace over the years, yet the bulk of the world's wafer production is still being probed with a traditional wire/needle probe card arrangement—a technology that was basically developed more than 25 years ago. Based on this technology a minimum distance between two probes is limited to 125 μm and number of pads is limited to 500. And contact pressure is not uniform from probe to probe with varying cantilevers because probe needles contacting corner pads are shorter, and probe needles contacting the center pads are longer. Additionally, planarization is difficult to maintain because each needle must be pushed or pulled with tweezers. Generally a planarization no better than +/- 18 μm is achievable [3].

At the 1988 International Test Conference, both Hewlett-Packard and Tecktronix [2] presented papers on different membrane probe cards, made by deposition and etching onto polyimide. The membrane card, however, appears to be an IBM invention, dating from 1969, which the computer giant never developed commercially. Apparently HP never sold its membrane cards outside the company. Tektronix, though, reportedly sold and delivered more than 25 membrane cards in 1988-89. Now other companies have picked up on the technology. Packard-Hughes Interconnect and Probe Technology Corporation has become a major supplier of membrane cards. In 1992 Mark Beiley, Justin Leung and S. Simon Wong of Stanford University [4-7] developed a membrane probe card using silicon wafer process technology.

The membrane probe card uses a flexible membrane with lithography-defined micro-strip transmission lines that terminate in contact bumps [8]. It improved needle type probe card limitation. The minimum distance between two probes was reduced to 100 μm [2]. The planarization of the membrane probe card became easy to maintain due to using lithography processes instead of mechanical processes. Additionally, the membrane card was noted for its improved electrical performance, achieving bandwidths of over 2.3 GHz [2].

However membrane probe cards also have some limitations. First, all probe points on a probe card must contact the chip simultaneously with a single applied force. This becomes increasingly problematic as chip complexity and number of contacts increase, and as the incidence of non-coplanarity of contact surface increases. Next, both cards must be custom-designed for specific chip designs, since each new I/O pad layout requires a new probe layout. This drives up the cost for the probe card technology. Additionally the minimum distance between two probes is limited to 100 μm due to mechanical consideration [2]. Finally there are also planarity problem with a large die, because the membrane is curved and bowed in order to contact the test chip. As the die gets larger, the membrane needs also to become much larger. Added to this problems is the newer complexities offered by Multi-Chip Modules (MCMs) where contact pads or bump may no longer be co-planar requiring the test probe points to adjust to test surfaces of varying heights.

1.2 This Research Objective

These problems mentioned in the above section can be solved through the creation of a new type of wafer probe card which consisting of an array of micro-cantilever probes individually actuated by bimorph heating to make contact with the testing pads [9], [10]. Each individual microprobe in the probe card could be used not only as a contact probe but also as a micro switch during testing which makes the probe card more generally useful. Actuation of the microprobes is created by cantilever bending through Joule heating of a bimorph film element on the cantilever. This probe card could also be designed with a generic layout and served as a multi-user probe card. This new type of probe card offers a Conformable, HIgh Pad-count Programmable test system capability and is called the CHIPP probe card. This Ph.D. dissertation will discuss the development, design, simulation, fabrication and testing of the microprobes essential to the formation of a CHIPP probe card.

CHAPTER 2

MEMS MICROACTUATION

Because probe card technology requires moving probes to make ohmic contact, it is necessary to have a method of producing accurate, small-scale forces to move probes in at least one direction. Basic forces used for micromechanical actuation in order to achieve individual probing action are electrostatic, thermal bending, magnetic, and piezoelectric forces. Numerous Micro Electro Mechanical Systems (MEMS) structures have been realized and commercialized based on these actuation techniques [11-14].

2.1 Thermal Actuation

Actuation based on a thermal drive method has been achieved for many different MEMS applications [16-20]. The reasons for the popularity of thermal actuation are many: First, thermal actuation has allowed many applications to achieve large deflections (greater than 100 μm) with voltages comparable to those used in standard microelectronic circuits (less than 10 volts) [15-19]. Next, the fabrication process is fully compatible to standard IC process steps. Finally, the mechanical force available is large and the transducer elements exhibit a high mechanical rigidity. However, thermal devices are usually characterized by high power consumption, and precise control motion may not be easily implemented. However, thermal actuation remains useful for a number of application requiring large forces and displacements.

2.1.1 Bimorph Actuation

The most common type of heat-driven device is the bimorph actuation structure (see Figure 2.1). The bimorph actuator consists of two or more materials with differing coefficients of thermal expansion. When the materials are uniformly heated, the coefficients of thermal expansion mismatch between the two or more materials forces a displacement directly related to the amount of applied thermal energy. The method used to heat the actuator depends on the application, but the most common method consists of using a heater integrated in the device.

A simple device that uses the bimorph structure is the cantilever beam as shown in Figure 2.1 [15]. Deflection distances of up to 100 μm with input power about 200 mW have been achieved using such cantilevers composed of a gold-silicon sandwich, which is 500 μm in length, 100 μm in width and 4 μm in height [15]. A motion of the cantilever could be optically observed up to a frequency of 35 Hz [15].

A more complex thermal bimorph structure which can have bistable operating states was developed by Hirotsugu Matoba [19]. The cantilever formed from three thin-film layers: (polysilicon, silicon dioxide, and polysilicon) is made to buckle as a result of strong axial force from a built-in tension. Joule heating in one of the two polysilicon layers of the buckled cantilever gives rise to a snapping action that moves the cantilever end +/- 6 μm in a direction perpendicular to the underlying silicon substrate.

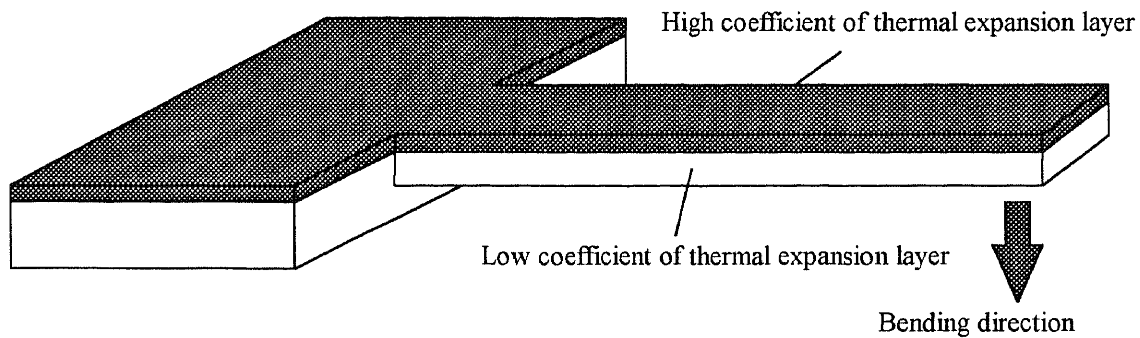

Figure 2.1 Bimorph cantilever actuation structure.

2.1.2 Thermal Driven Cantilever Flexure

Another device utilizing thermal actuation is the thermal driven beam flexure [20]. Rather than using a bimorph structure to generate a force through thermal expansion mismatch between materials, the thermal driven beam flexure uses differential heating of the same material created by running a current through a loop of conductive material of varying width (Figure 2.2). The variation in resistance caused by the changes in width causes a temperature difference, which can generate bending force in the low temperature direction

due to the reason that the narrower sections in the beam are hotter and thermally expand to a greater degree than the wider sections. A thermal driven beam flexure formed from nickel with a length (L) of 1000 μm, height (h) of 50 μm and widths of 4 μm (W1) and 8 μm (W2) has achieved a tip deflection of over 100 μm with 100 mA of applied current [20].

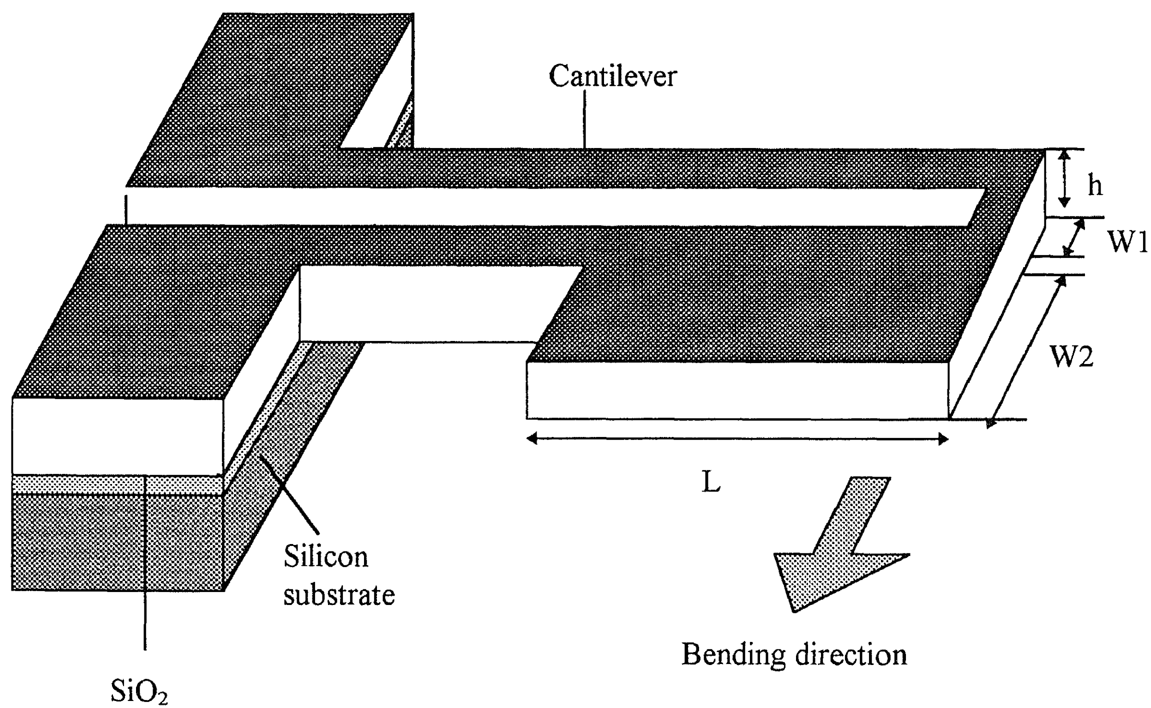

Figure 2.2 Horizontal heat-drive actuator.

2.2 Electrostatic Actuation

Electrostatic actuation has been widely used in MEMS devices [21-27] because these forces can be implemented using static voltages requiring only insulative and conductive thin films which are available using conventional IC fabrication techniques. For MEMS device designed with feature sizes achievable in current lithography techniques, electrostatic force are quite large when small capacitive gaps are used. Additionally, electrostatic forces can achieve precise control of the actuation force by fine tuning the applied actuation voltage with fast response times down into the microsecond range. The power dissipation is also very small (near zero) because there is only leakage current. Despite these advantage, however, electrostatic device generally give lower maximum actuation distances than can be achieved with other actuation methods because the electrostatic force is inversely proportional to the square of the distance between electrodes [28]. As a result, electrostatic devices usually have gap distances smaller than 5 μm. Additionally, the moving directions of the electrostatic actuators usually limited on the substrate surface due to the limitation of a small actuation distance. Finally, there also are important limitations related to the electrostatic hysteresis due to the electron charge on the insulator layer of the switch type devices.

2.2.1 Electrostatic Cantilever Actuation

The simplest structure that can be achieved using electrostatic actuation is the cantilever actuator (Figure 2.3). Once a cantilever has been fabricated, the cantilever and the substrate drive electrode form a simple parallel plate capacitor. Therefore, any deflection

in the cantilever approximately follows the parallel plate capacitor arrangement (assuming the slight deformations of the cantilever are negligible).

The relation between force, voltage and cantilever deflection is given by

$$\overline{F} = \frac{1}{2}V^2\frac{dC}{dx}\overline{x} = \frac{A}{2}\varepsilon_0\varepsilon \cdot \frac{V^2}{(d-x)^2}\overline{x} \tag{2.1}$$

Where A is cantilever area (assume the area of the drive electrode is larger than cantilever area A), V is voltage applied between the cantilever and the drive electrode, ε is dielectric constant, ε_o is permitivity of free space, x is the cantilever deflection due to electrostatic force, and d is the initial gap between the cantilever and the electrode (see Figure 2.3). Because the electrostatic force is inversely proportional to the square of the distance formed between the cantilever and the drive electrodes, the capacitive force pulling the cantilever increases rapidly as the cantilever deflects. At some critical point, the force is great enough to force the cantilever to deflect instantly for the remaining distance. This critical distance is about 1/3 of the actuation distance [28]. Because the capacitive force becomes very small as the gap increases, electrostatic force method only applies to small gap systems.

Cantilever structures while conceivably useful as actuators have generally been used as resonant sensors. For such applications, the beam is acted upon by outside force and any resulting deflection can be capacitively sensed. Using the same principle, however, it is also possible to force the cantilever to deflect and form a switch by applying a voltage between the cantilever and the drive electrode.

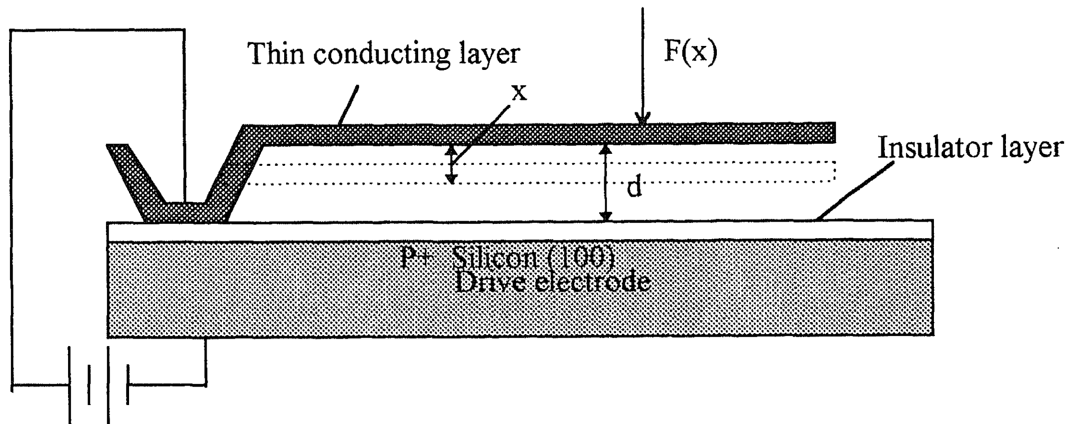

Figure 2.3 Basic electrostatic cantilever actuator.

2.2.2. Electrostatic Microbridge Actuation

Electrostatic microbridges, which operate under the same principle as cantilevers, are also simple to design and fabricate [23-27]. Most microbridges are fabricated in a surface micromachining process using polysilicon or metal as the primary structural material, polyimide, Al or SiO_2 as the sacrificial layer. Beneath the bridge, several conductive regions are either deposited or diffused for use as drive and sense electrodes. For use as a sensor, an alternating voltage is applied between the microbridge and the drive electrodes. The resulting oscillation is sensitive to parameters such as ambient temperature and pressure. By capacitively sensing the oscillation of the bridge it is possible to sense

differences in ambient conditions. For use as a microswitch, a d.c. voltage of sufficient magnitude between the microbridge and drive electrodes can force the microbridge to touch the sense electrode, thus allowing a connection to be made. The microbridge structures (Figure 2.4) usually have applied voltages between 10-100v depended on the device structures [24], [26].

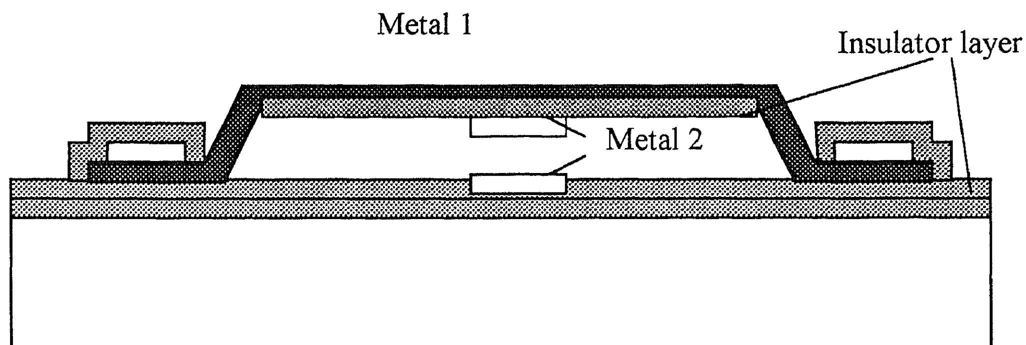

Figure 2.4 Resonant microbridge/switch microbridge.

2.3 Magnetic and Piezoelectric Actuation

The last methods of micromechanical actuation, magnetic and piezoelectric, are less popular, but have been used for very specific applications. In order to implement magnetic actuation, a magnetic field on the MEMS scale must be produced. This can be done by using small permanent magnets or by developing a MEMS sized electromagnet. The former has been performed [29], [20], but the size limitation and fabrication

difficulties preclude the use of permanent magnets for most MEMS devices. The latter is more feasible, but presents its own array of difficulties. Magnetic actuation involves persistent conduction losses due to the currents required for static excitation as well as hysteresis and eddy current losses at higher actuation speeds [20].

Piezoelectric actuation [31], [32] shares many similarities with electrostatic actuation. Piezoelectric actuators operate utilizing the property that when a voltage is applied across a piezoelectric material, a small deformation can be created. Because piezoelectric materials can be deposited and lithographically patterned, it is possible to create small-scale devices if voltages large enough to achieve the desired motion are employed. However, thin film piezoelectric actuation shares many of disadvantages of magnetic actuation.

Comparing with magnetic or piezoelectric actuation which has many limitations, electrostatic and thermal devices are preferable due to easy actuation, simply structure and compatibility with commercial microelectronics fabrication processes [33].

CHAPTER 3

CONCEPT AND DESIGN OF MEMS PROBE CARD

In chapter 1 we have compared two different current probe card technologies. These two technologies have some inherent advantages but also limitations. First, the needle/epoxy probe card technology has a maximum 500 pin count limitation, and its minimum spacing between two probes is also limited to ~ 125 μm. The membrane probe card technology has improved the maximum 500 pin count limitation of the needle/epoxy probe card, but it is also limited to a minimum spacing of ~100 μm between two probes. Both type of probe cards have planarization problems. Finally, both probe cards must be custom-designed for specific chip designs since each new I/O pad layout requires a new probe layout. This limits probe card applications. In order to solve these limitation a new concept of MEMS cantilever probe card has been developed [9], [10] and described in this chapter.

3.1 CHIPP Probe Card

3.1.1 Concept of CHIPP Probe Card

A new probe card concept is developed through the creation of an array of micro-cantilever probes individually actuated by bimorph heating to make contact on the test pads of a device chip during wafer-stage testing [9]. Bending action is created through Joule heating of a bimorph film element on the cantilever. The probe movement is controlled by heating current. At room temperature the cantilever is initially balanced at zero stress position. When the cantilever is heated, the metal layer which has a large thermal expansion coefficient will expand more than the low thermal expansion material layer, generating a thermal stress between two layers, causing the cantilever to bend,

contact is thus made to the device pad. Because the bending distance (deflection) of a micro cantilever linearly depends on the input power, contact can be made at different heights of testing pads through controlling the input power.

An illustration of one of these microprobes contacting a test chip is shown in Figure 3.1. Thermal actuation of a bimorph is used instead of electrostatic actuation because each microprobe must move away from the surface of the probe wafer toward the test chip instead of toward the substrate surface, and the moving distance is large (about 20-40 μm). Thus the bimorph structure must be fabricated with the higher expansion material deposited before deposition of the lower expansion material, unlike most other bimorph actuators with a cantilever configuration [16-20].

This new probe card is called a CHIPP (Conformable, High Pad-count, Programmable) probe card. Compared with the existing probe card technologies, the CHIPP probe card has many advantages. Because the CHIPP probe card uses IC process technology through a silicon wafer substrate, the minimum repeat distance between two probes has been decreased to 50-60 μm (cantilever width of 40-50 μm + gap of 10 μm). Additionally, the probe array can be designed for general testing on generic designs since each cantilever probe is individually actuated. Finally, the CHIPP probe card can be used for testing pads with varying heights; this expands the test applications of the probe card.

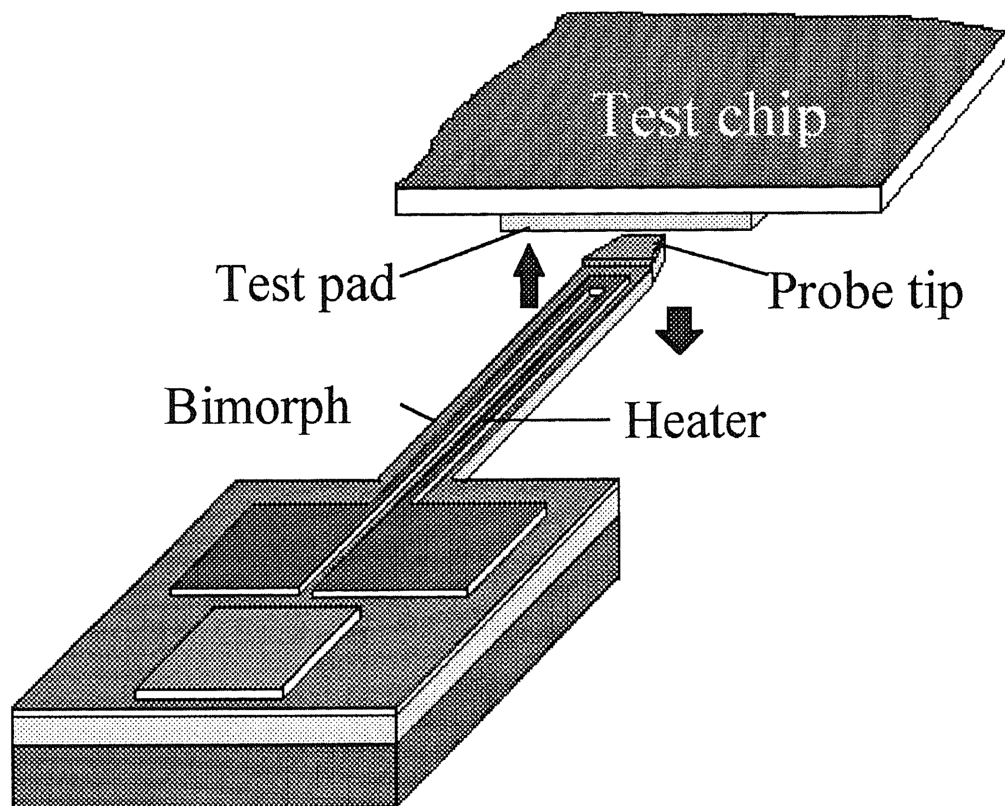

Figure 3.1 Microprobe making ohmic contact with the surface of a test chip.

3.1.2 Design of Prototype CHIPP Probe Card

The CHIPP probe card can be designed to be any size and forming an opening in the silicon substrate according to a customer's requirement. A total of 800 microprobes can be arranged along the edges of a $1cm^2$ chip. Figure 3.2 illustrates a structure of a CHIPP probe card. A bulk micromachining method is used for releasing the cantilever probe. The Si (100) wafer is serves as the probe card frame and substrate. Because the contact pads are usually designed along the periphery of the chip the array of microprobes are placed along the edge of the opening. However, this design could also be used for interior type device pads by using a small opening under each micro cantilever (see Figure 3.3).

This experimental prototype probe card was designed to address a $1cm^2$ size chip. The shapes and sizes of the cantilever and heater varies for experimental purposes. The prototype has 58 cantilever microprobes in 12 different shapes, with 4-5 probes for each shape. In addition the shape of the heater varies for different types of micro probes. The microprobes are positioned around a 1 cm^2 center opening which can be used as a device alignment window. The cantilever probes in this prototype test probe card have 3 large pads (200 μm) near each cantilever for making electrical connection to the contact region at the tip (1 pad) and heater (2 pads). For real probe card designs the pads will be replaced with metal micro-strips which lead the wire to the I/O pads on the edge of the wafer. In this way the probe density will be increased to over $1000/cm^2$.

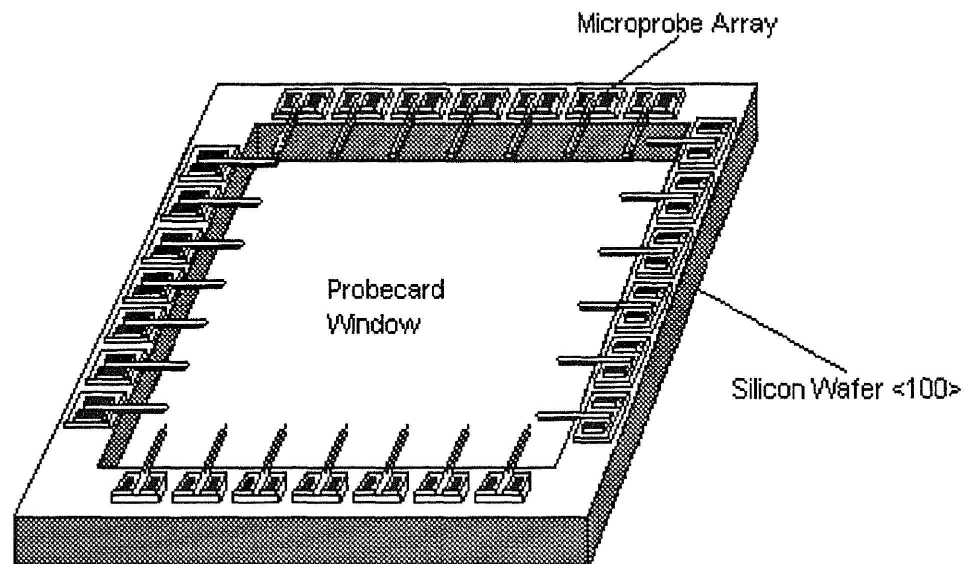

Figure 3.2 Illustration of prototype CHIPP probe card showing microprobes positioned about a center opening. The test chip is mounted face-down over the probe card.

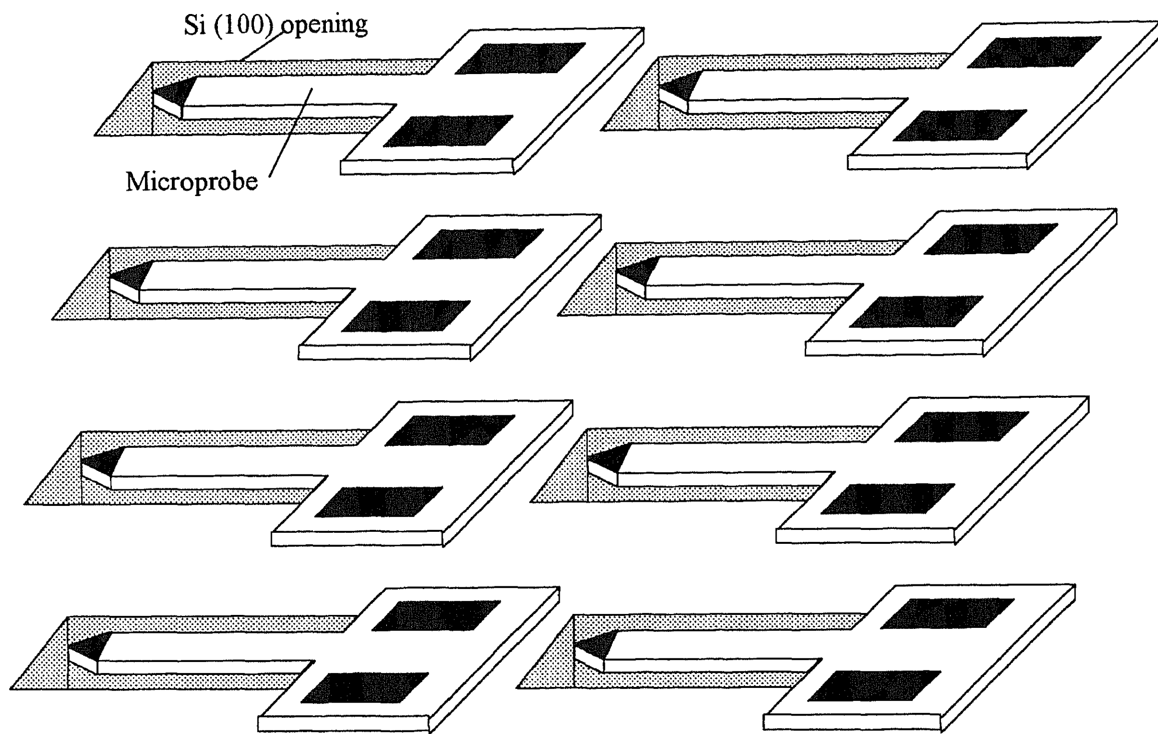

Figure 3.3 Illustration of arrangement of MEMS microprobes for contacting interior pads.

3.2 CHIPP Microprobe

The microcantilever probe is a key element for successful probe card. In order to obtain effective probing action, the microprobe has to be designed so that it can move the cantilever large distances to contact chip pads, it consumes little power, and it can provide a large force to help in making ohmic contact.

3.2.1. Physical Design of CHIPP Microprobe

The bimorph cantilever materials are carefully considered to provide good adhesion and large bending ability. The adhesion of grown and deposited films used in device processing must be excellent, both after deposition, and after subsequent processing. If the film lifts from the substrate, device failure can result, and thus poor adhesion represents a potential reliability problem.

Thermal-driven actuation is based on the stress of the cantilever structure. Nearly all films are found to be in a state of internal stress, regardless of the means by which they have been produced. The stress may be compressive or tensile. Compressively stressed films would like to expand parallel to the substrate surface, and in the extreme, films in compressive stress will buckle up on the substrate. Film in tensile stress, on the other hand, would like to contract parallel to the substrate, and may crack if their elastic limits are exceeded. The total stress, σ, in a cantilever is the sum of: a) any external stress, $\sigma_{ext,}$ on the cantilever; b) thermal stress, σ_{th}; and c) the intrinsic stress, σ_{int}. The total stress is written as:

$$\sigma = \sigma_{ext} + \sigma_{th} + \sigma_{\text{int}} \tag{3.1}$$

Thermal stress results from the difference in the coefficients of thermal expansion between the two films. The thermal stress is due to the constraint imposed by the two film bonding and is given by:

$$\sigma_{th} = (\alpha_1 - \alpha_2) \cdot \Delta T \cdot E_f \tag{4.2}$$

where, α_1 and α_2 are the average coefficients of thermal expansion for the bimorph films; ΔT is the temperature of film growth minus the temperature of measurement; and E_f is the average Young's modulus of the films. The σ_{th} can be of either sign (positive is tensile, negative is compressive), based on the relative values of α_1 and α_2.

The intrinsic stress reflects the film structure in ways not yet completely understood. It has been observed that the intrinsic stress in a film depends on thickness, deposition rate, deposition temperature, ambient pressure, method of film preparation and type of substrate used, among other parameters [34]. At low deposition temperature, metal films tend to exhibit tensile intrinsic stress. This decreases with increasing deposition temperature (often in a linear manner), finally going through zero to compressive.

The external stress σ_{ext} in films also not yet understood. It is obvious that the external stress depends on interface materials, diffusions, and deposition temperature.

In the general design of a microprobe, the initial total stress must be kept small. A large initial stress will cause initial bending of the released cantilever, thus require a extra power to move the cantilever up to the original position. In addition a large difference of coefficients of thermal expansion between two bimorph materials is required for a large thermal driven deflection because the thermal stress mainly depends on the difference of thermal expansion coefficients and Young's modulus from equation (3.1). When the cantilever is heated, the thermal stress is built up, internal and external stresses are also changed, although their changes are usually smaller than thermal stress. Because the internal and external stresses are not yet completely understood, their bending direction may not be known in advance; this is another reason why we chose a strong thermal stress system.

A series of experimental bimorph systems have been chosen. The first set of devices was designed with a gold contact and an aluminum-SiO_2 bimorph system. Aluminum has a high thermal expansion coefficient of 23 x 10^{-6} /K (see Table 3.1), good adhesion with SiO_2 which has very small thermal expansion coefficient of 0.4 x 10^{-6} /K; a large tip motion is expected. The second bimorph system used was W-SiO_2. Tungsten has a relatively small thermal expansion coefficient of 4.4 x 10^{-6} /K, but it has a high Young's modulus of 411 GPa and high melting point, and good adhesion with SiO_2.

Many different cantilever structures were also designed for an experimental purposes because deflections and tip forces of the micro probe cantilever strongly depend on its sizes and materials. A total 12 different cantilevers were made with two types of heaters inside (Figure 3.4) and outside (Figure 3.5) structures are listed in Table 3.2. The cantilever structure with heater inside has length L and width W, and the cantilever

structure with heater outside has length L, width W forming a electrical loop with a loop gap D (see Figure 3.5). A detailed analysis of the cantilever performance as a function of sizes and materials will be given in Chapter 4.

Table 3.1 Physical characteristics of microprobe cantilever layers[35-37].

Cantilever layer	Coefficient of thermal expansion (10^{-6}/K)	Young's modulus ($10^{11} N/m^2$)	Thermal conductivity (W/mK)	Melting point (°C)	Resistivity (μΩ.cm)
SiO_2(LTO)	0.4	0.73	2.66	unknown	unknown
Al	23	0.69	238	660	2.67
Cu	17	1.2	397	1083	1.698
Si_3N_4	2.8	1.55	18.5	unknown	10^{21}
W	4.4	4.11	178	3400	5.3
Si	2.6	1.62	170	1412	500
Ta	6.5	1.85	57.55	2980	13.5
Ti	8.9	1.2	21.6	1667	54

Table 3.2 Dimension parameters of component layers of CHIPP microprobes*.

Number	Cantilever type	Cantilever length L (μm)	Cantilever width W (μm)	Cantilever gap D (μm)
1	Heater inside the cantilever	500	50	
2	Heater inside the cantilever	500	60	
3	Heater inside the cantilever	400	40	
4	Heater inside the cantilever	400	50	
5	Heater inside the cantilever	300	40	
6	Heater inside the cantilever	300	50	
7	Heater inside the cantilever	200	30	
8	Heater inside the cantilever	200	35	
9	Heater outside of cantilever as bottom layer	500	40	10
10	Heater outside of cantilever as bottom layer	400	40	10
11	Heater outside of cantilever as bottom layer	300	40	10
12	Heater outside of cantilever as bottom layer	260	40	10

* L, W, D see Figure 3.4 and 3.5.

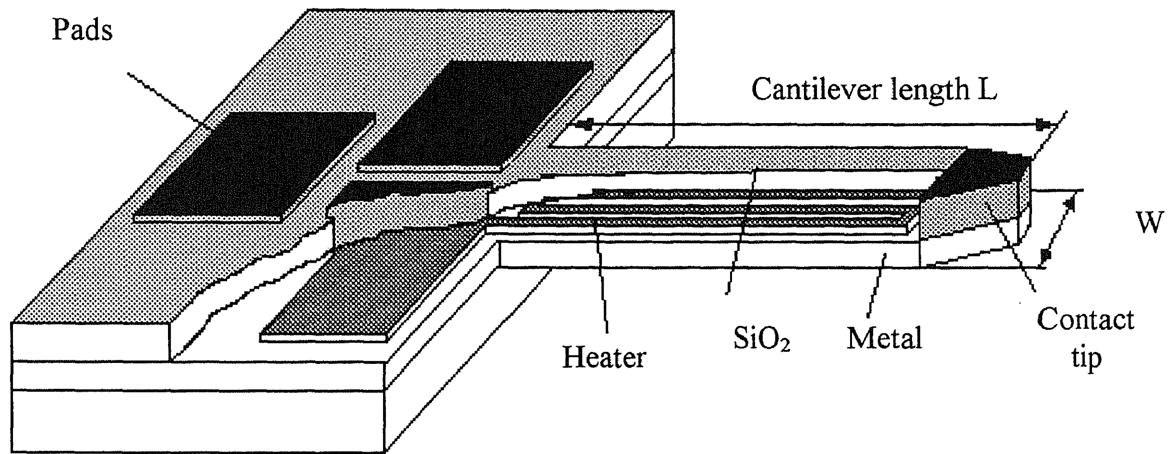

Figure 3.4 Illustration of microprobe with heater inside the cantilever.

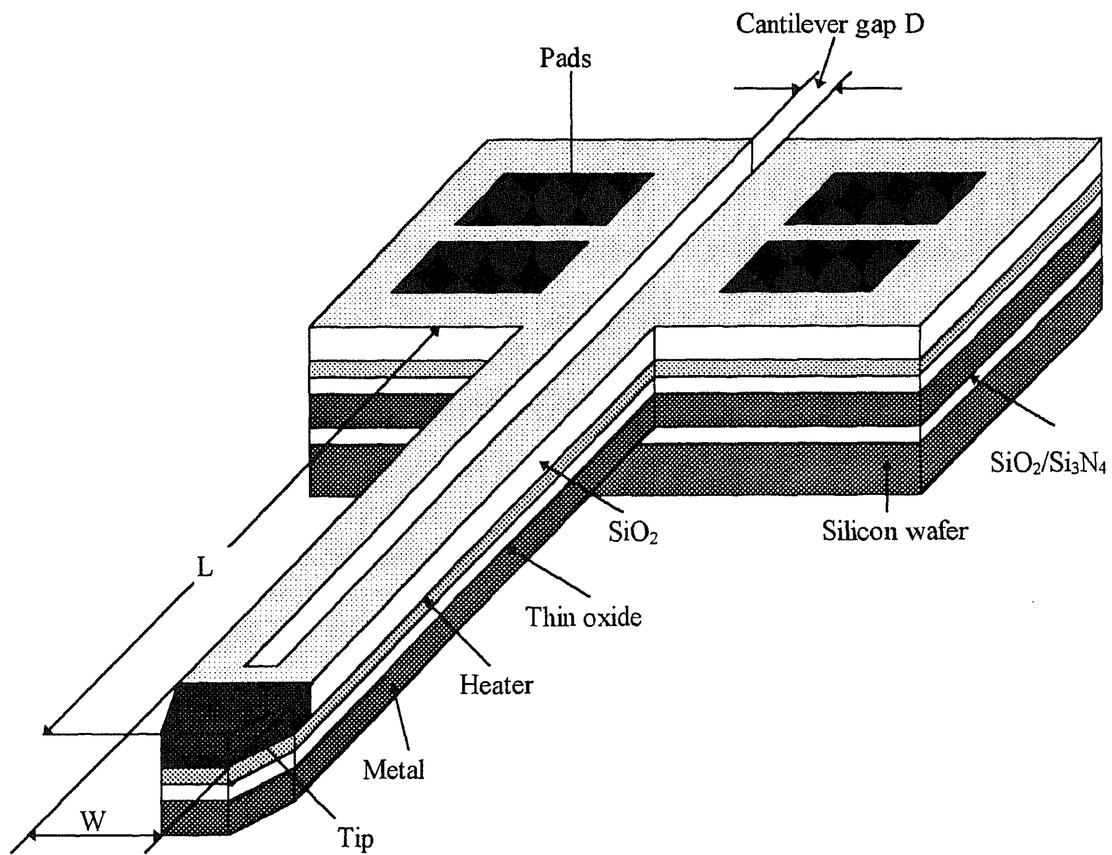

Figure 3.5 Illustration of microprobe showing heater as the bottom layer of the cantilever.

3.2.2. Heater Design of CHIPP Microprobe

A simple bimorph cantilever structure consists basically of two or three layers, with one of the cantilever layers serving as the heater located either on the top or bottom of the cantilevers, depending on the moving direction. However, this type of heat structure (see Figure 3.6) experiences a large amount of heat loss from air convection and radiation during Joule heating of the cantilever because the heater is in direct contact with air. In order to reduce the heat loss, a sandwich heater structure is designed. The structure of the sandwich cantilever is schematically illustrated in Figures 3.4 and 3.7. The two components of the bimorph cantilever are metal and SiO_2, and the heater is built inside the SiO_2 layer. This design can effectively reduce heat loss compared with traditional design, because heat flow now has to pass through the SiO_2 layer to reach the outside, and SiO_2 has very small thermal conductivity. In order to compare the two different cantilever structures a outside heater cantilever structure was also designed (see Figure 3.5).

The size and shape of the heater also has an important effects on heat loss because it changes heater resistance and heater area. Two major heater structures with 12 different sizes and contact tips (Table 3.3 and Figure 3.8) were used.

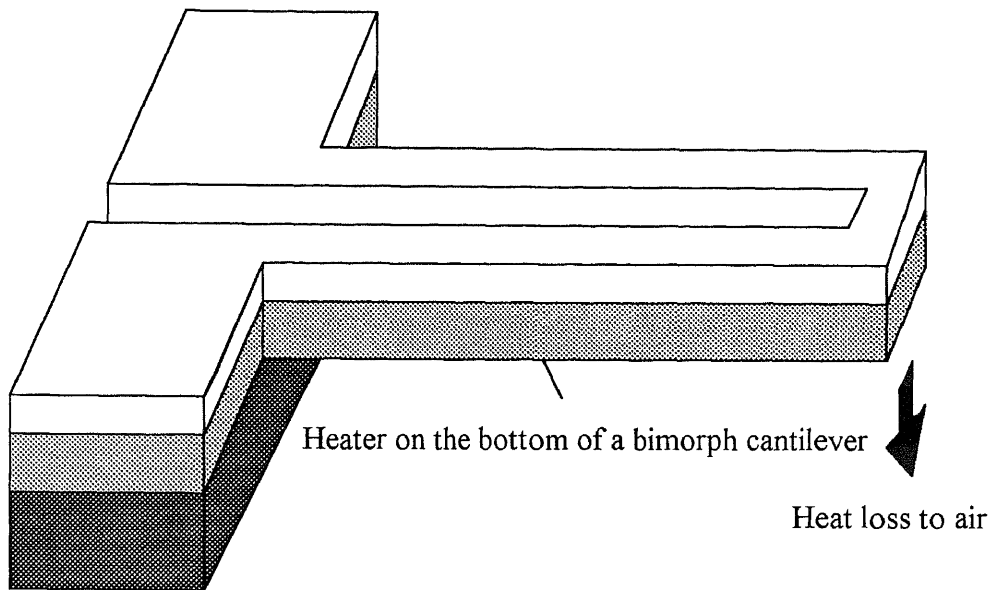

Figure 3.6 A bimorph cantilever structure with heater on the bottom layer showing the heat loss from the heater directly to air.

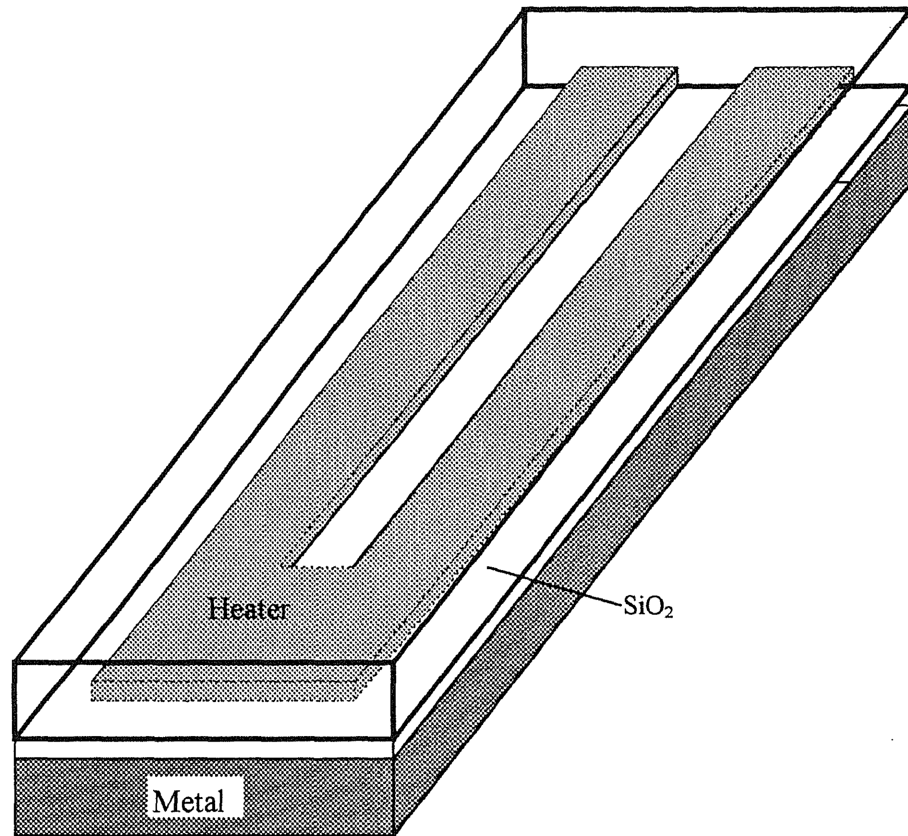

(a) Side view of a heater inside cantilever showing a half cantilever

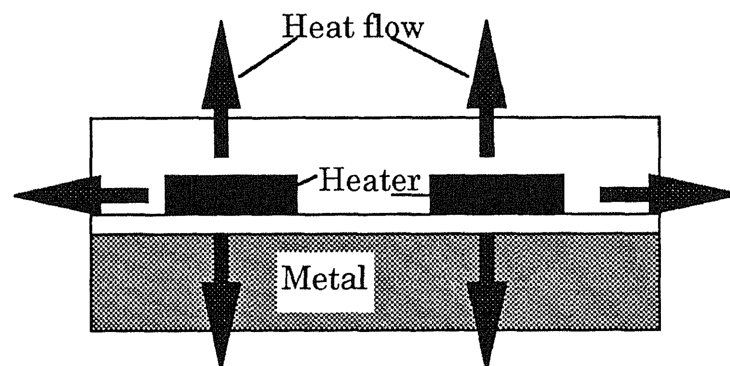

(b) A cross section of the cantilever showing diffusion barriers to heat loss to air.

Figure 3.7 Details of heater inside the cantilever showing heat flow.

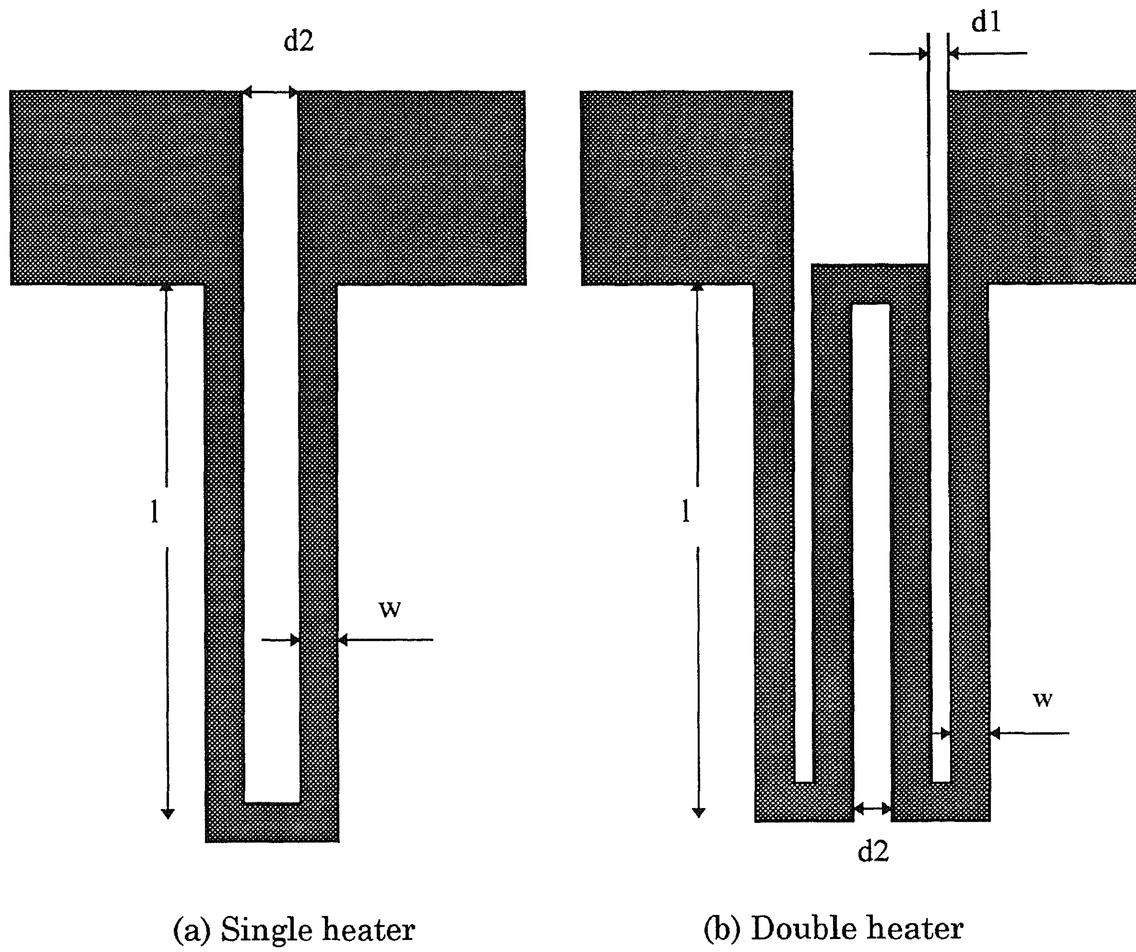

Figure 3.8 Heater designs used in CHIPP microprobe.

Table 3.3 Dimension parameters of CHIPP microprobes *

Cantilever type	Cantilever sizes (μm)			Heater sizes (μm)			
	L	W	D	l	w	d1	d2
Double heater inside cantilever	500	50		470	7	5	6
Double heater inside cantilever	500	60		460	7	5	6
Double heater inside cantilever	400	40		368	5	5	4
Double heater inside cantilever	400	50		360	7	5	6
Double heater inside cantilever	300	40		280	5	5	4
Double heater inside cantilever	300	50		270	7	5	6
Single heater inside cantilever	200	30		188	10		4
Single heater inside cantilever	200	35		188	12		5
Single heater on the bottom of cantilever	500	40	10	500	15		10
Single heater on the bottom of cantilever	400	40	10	400	15		10
Single heater on the bottom of cantilever	300	40	10	300	15		10
Single heater on the bottom of cantilever	260	40	10	260	15		10

*Parameters L, W and D see Figure 3.4, Figure 3.5 and l, w, d1, and d2 see Figure 3.8.

3.3 Ohmic Contact Issues and Solutions

3.3.1 Contact Force Required

An ohmic contact between the microprobe and the test pad is sometimes difficult to make because of a thin metal-oxide film on some metal surface due to oxidation. An extra sliding force (called "scrub") is needed to scrape through the oxide films before ohmic contact can be made. The force required for ohmic contact is difficult to model because of two factors: the uncertainty of the contact area, and the effect of interfacial insulating layers such as oxide or hydrocabon contamination.

A range of applied forces has been reported, depending on the circumstance. Forces of ~0.1 N are reported for conventional spreading resistance probe contacts where the contact area is assumed to be a disc of 5 μm diameter [38-39], the force required to make ohmic contact between two larger gold contacts [40] (of unspecified area) is more than 10 μN and the force required for contact between an AFM tip and a metal-coated surface [41] is less than 1μN.

3.3.2. Ohmic Contact

Ohmic contact between clean metal surfaces such as gold does not require scrub and contact forces are expected to be small. Contact to aluminum which grows a thin aluminum oxide film quickly when exposed to air is more difficult and a scrub action in the probe tips may be required.

The CHIPP probe card is designed with three different tips, gold, diamond and tungsten. Gold tips are used for contacting to the clean metal pads, and conducting diamond tips are used for scrubbing metal pads covered with thin metal-oxide films.

Probe scrub is created through lateral motion of the cantilever tip over the pad surface. The shapes and sizes of the microprobe tips are shown in Figure 3.9 (a) and Table 3.5. The bending force on the cantilever tip can be separated into two components; one toward the pad surface called F_{press}, and the other is parallel to the pad surface called F_{scrub}. The force F_{scrub} causes the probe tip to scrub the thin oxide along the pad surface, the force F_{press} cause the probe tip to push into the pad surface along the vertical direction, breaking through thin oxide film on the metal surface.

When contact is made continued force will cause tip to bend (see Figure 3.9(b)). The bending curvature depends on the tip shape, with narrow tips producing more bending curvature than wide tips. Scrub force also depends on the tip curvature because tip curvature determines the contact force angle. 12 different tip shapes are designed for experimental purpose (see Table 3.5). Conducting diamond is highly boron doped diamond which is grown at 900-1000°C by sp^3, Inc. [42]. Diamond is used because it is very hard and abrasive. The diamond crystals, which are 0.1 to 1 μm in size, have very sharp angles which scrub through the thin metal-oxide film on the test pad surface. The diamond can be best be grown on a tungsten surface, so tungsten tips are used.

Tungsten has excellent fatigue resistance and good hardness, therefore it is used as a probe tip in conventional probe card. In this probe card design tungsten is also selected as tip material and as a candidate for making ohmic contact.

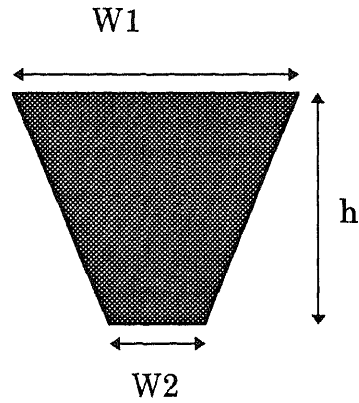

(a) Tip shape of CHIPP microprobes.

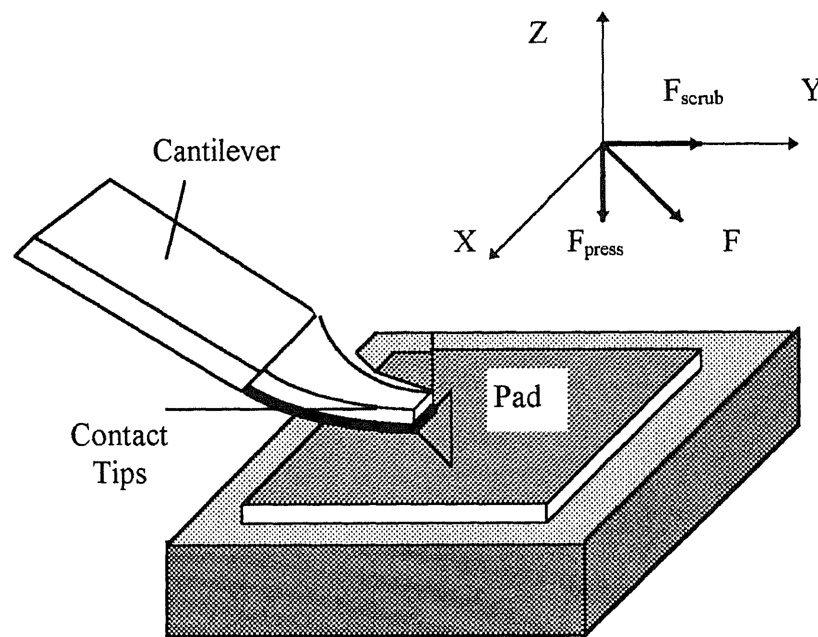

(b) Microprobe tip making contact on test pad.

Figure 3.9 Illustration of tip of CHIPP microprobe.

Table 3.4 Dimension parameters of tips of CHIPP microprobes.

Cantilever type	Cantilever sizes (mm)			Tips sizes		
	L	W	D	W1 (μm)	W2 (μm)	h (μm)
Double heater inside cantilever	500	50		50	24	35
Double heater inside cantilever	500	60		60	30	44
Double heater inside cantilever	400	40		40	20	33
Double heater inside cantilever	400	50		50	20	50
Double heater inside cantilever	300	40		40	20	23
Double heater inside cantilever	300	50		50	30	34
Single heater inside cantilever	200	30		30	14	20
Single heater inside cantilever	200	35		35	19	20
Single heater on the bottom of cantilever	500	40	10	40	20	29
Single heater on the bottom of cantilever	400	40	10	40	16	31
Single heater on the bottom of cantilever	300	40	10	40	16	31
Single heater on the bottom of cantilever	260	40	10	40	16	31

CHAPTER 4

MODELING AND SIMULATION

In chapter 3 a structure of the thermal bimorph cantilever has been discussed. Based on this structure a cantilever probe array has been designed as a CHIPP probe card. In this chapter the bimorph cantilever with different boundary conditions will be analyzed and simulated according to a general theory of thermal stress and bending for the bimorph structure.

4.1 Analysis of a Bimorph Structure

4.1.1 Analysis of a Bimorph Cantilever with Two Free Ends

The following analysis is based on a general theory [18], [43] of bending of a bimorph cantilever with a uniform heating. It is assumed that the difference in the coefficients of thermal expansion remains constant during the heating.

Let a narrow cantilever consisting of two materials be uniformly heated from t_0 °C to t °C. If the coefficient of linear expansion of these materials be different the heating will produce bending of the cantilever. Let α_1 and α_2 denote the coefficients of thermal expansion of the two layers (1) and (2) (see Figure 4.1).

Consider an element cut out from the middle of the cantilever (see Figure 4.1). If $\alpha_2 > \alpha_1$ the deflection will be convex down, as shown in Figure 4.1. All the forces acting over the section of the layer (1) on the concave side can be represented by an axial tensile force P_1 and bending moment M_1. For layer (2) on the convex side all forces acting on the cross-section can be represented by an axial compressive forces P_2 and bending

moment M_2. Due to the fact that there are not external force acting on the cantilever, all forces acting over any cross-section of the strip must be in equilibrium, therefore,

$$P_1 = P_2 = P \tag{4.1}$$

$$\frac{P(t_1 + t_2)}{2} = M_1 + M_2 \tag{4.2}$$

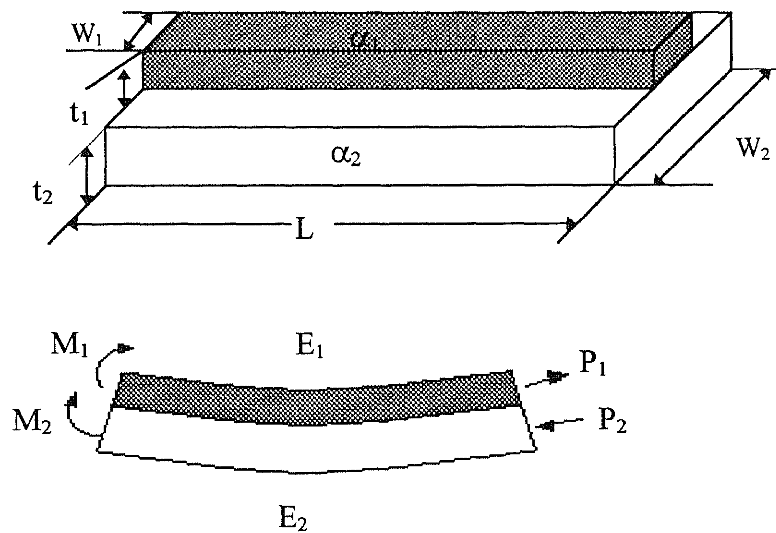

Figure 4.1 Deflection of a bimorph cantilever with uniform heating.

Letting R = radius of curvature of cantilever,

$E_1 I_1$ = the flexural rigidity of the layer (1)

$E_2 I_2$ = the flexural rigidity of the layer (2), then,

$$M_1 = \frac{E_1 I_1}{R} \tag{4.3}$$

$$M_2 = \frac{E_2 I_2}{R} \tag{4.4}$$

Substituting in (2)

$$\frac{P(t_1 + t_2)}{2} = \frac{E_1 I_1 + E_2 I_2}{R} \tag{4.5}$$

Another equation for calculating P and R will be obtained from the consideration of deformation. On the bearing surface of both metals the unit elongation occurring in the longitudinal fibres of layers (1) and (2) must be equal, therefor,

$$\alpha_1 (t - t_o) + \frac{P_1}{E_1 W_1 t_1} + \frac{\alpha_1}{2R} = \alpha_2 (t - t_o) - \frac{P_2}{E_2 W_2 t_2} - \frac{\alpha_2}{2R} \tag{4.6}$$

Using (4.5) and (4.6) ,

$$(\alpha_2 - \alpha_1)(t - t_o) = \frac{(t_1 + t_2)}{2R} + \frac{2(E_1 I_1 + E_2 I_2)}{(t_1 + t_2)R}(\frac{1}{E_1 W_1} + \frac{1}{E_2 W_2}) \tag{4.7}$$

Here I_1 = $W_1/12$ and $I_2=W_2/12$ and finally, the expression for the cantilever curvature 1/R is given:

$$\frac{1}{R} = \frac{6 W_1 W_2 E_1 E_2 t_1 t_2 (t_1 + t_2)(\alpha_2 - \alpha_1)\Delta T}{(E_1 W_1 t_1^2)^2 + (E_2 W_2 t_2^2)^2 + 2 W_1 W_2 E_1 E_2 t_1 t_2 (2t_1^2 + 3t_1 t_2 + 2t_2^2)} \tag{4.8}$$

Assuming a constant radius of curvature R for a cantilever length L we obtain the displacement δ of the cantilever tip at small deflection angle:

$$\delta = \frac{1}{2}\frac{L^2}{R} \tag{4.9}$$

4.1.2 Analysis of Bimorph Cantilever with Left End Free and Right End Fixed

Although equation (4.8) and (4.9) are deduced from both end free case, this equations are also true for one end free and the other fixed case [44]. According to W. C. Young [43] and M. Mehragany [18] the same deflection equation can be obtained :

$$\delta = \frac{3W_1W_2E_1E_2t_1t_2(t_1+t_2)(\alpha_2-\alpha_1)\Delta T(L^2-x^2)}{(E_1W_1t_1^2)^2+(E_2W_2t_2^2)^2+2W_1W_2E_1E_2t_1t_2(2t_1^2+3t_1t_2+2t_2^2)} \tag{4.10}$$

Maximum deflection value is achieved when x = 0:

$$\delta_{\max} = \frac{3W_1W_2E_1E_2t_1t_2(t_1+t_2)(\alpha_2-\alpha_1)\Delta T\cdot L^2}{(E_1W_1t_1^2)^2+(E_2W_2t_2^2)^2+2W_1W_2E_1E_2t_1t_2(2t_1^2+3t_1t_2+2t_2^2)} \tag{4.11}$$

Where x is the distance from cantilever tip to the point where deflection is considered. The other parameters are the same as above.

The Slope of the cantilever (see Figure 4.2) can be given:

$$\theta = \frac{-3W_1W_2E_1E_2t_1t_2(t_1+t_2)(\alpha_2-\alpha_1)\Delta T(L-x)}{2\{(E_1W_1t_1^2)^2+(E_2W_2t_2^2)^2+2W_1W_2E_1E_2t_1t_2(2t_1^2+3t_1t_2+2t_2^2)\}} \tag{4.12}$$

Maximum slope of the cantilever can be obtained let x = 0:

$$\theta_{\max} = \frac{-3W_1W_2E_1E_2t_1t_2(t_1+t_2)(\alpha_2-\alpha_1)\Delta T\cdot L}{2\{(E_1W_1t_1^2)^2+(E_2W_2t_2^2)^2+2W_1W_2E_1E_2t_1t_2(2t_1^2+3t_1t_2+2t_2^2)\}} \tag{4.13}$$

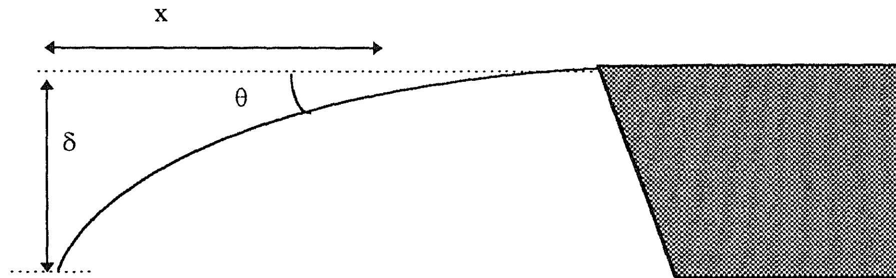

Figure 4.2. Cantilever deflection with left end free and right end fixed.

4.1.3 Force Analysis of One End Fixed Cantilever

A cantilever beam fixed at the right end and carrying a concentrated load F at the point x away from the lift free end is shown in Figure. 4.3. The deflection caused by the external load F is d which cam be obtained [45] as following equation:

$$\delta_F = -\frac{1}{6}\frac{F}{EI}(2L^3 - 3L^3 x + x^3) \qquad (4.14)$$

The maximum deflection happens at x=0, and given as follows:

$$\delta_{F\max} = -\frac{1}{3}\frac{F}{EI}L^3 \tag{4.15}$$

In our cantilever deflection case the cantilever probe is firstly moved a distance d_0, then contact the test pad, which is the same cause as external force added at d_0. Therefore a deflection balance formula can be obtained :

$$\delta_F = \delta - \delta_0 \tag{4.16}$$

A general force equation caused by cantilever bending can be obtained using equation (4.10), (4.14) and (4.15):

$$F = \frac{18EI \cdot W_1 W_2 E_1 E_2 t_1 t_2 (t_1 + t_2)(\alpha_2 - \alpha_1)\Delta T (L^2 - x^2)}{(E_1 W_1 t_1^2)^2 + (E_2 W_2 t_2^2)^2 + 2W_1 W_2 E_1 E_2 t_1 t_2 (2t_1^2 + 3t_1 t_2 + 2t_2^2)(L^3 - 3L^3 x + x^3)} + \frac{6EI}{(2L^3 - 3L^3 x + x^3)}\delta_0 \tag{4.17}$$

The equation (4.17) is reduced to (4.18) at x=0, which is the case probe tip to make contact.

$$F = \frac{18EI \cdot W_1 W_2 E_1 E_2 t_1 t_2 (t_1 + t_2)(\alpha_2 - \alpha_1)\Delta T}{(E_1 W_1 t_1^2)^2 + (E_2 W_2 t_2^2)^2 + 2W_1 W_2 E_1 E_2 t_1 t_2 (2t_1^2 + 3t_1 t_2 + 2t_2^2)L} + \frac{6EI}{L^3}\delta_0 \tag{4.18}$$

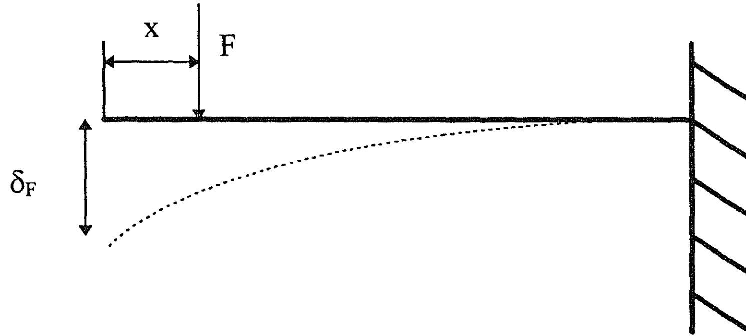

Figure 4.3 External force applied near the tip of the cantilever with one end fixed.

4.1.4 Equivalent Stiffness for Multi-Cantilever Layers

According to Young[44] cantilevers that are constructed of more than two materials can be treated by using an equivalent width technique if the maximum stresses in each of the several materials remain within the proportional limit. An equivalent cross section is developed in which the width of each component parallel to the principal axis of bending is increased in the same proportion that the modulus of elasticity of that component makes with the modulus of the assumed material of the equivalent cantilever. Figure 4.4 shows the cantilever with three different material layers.

For this equivalent cross section the centroid must be located and the moment of inertia determined for the centroidal axis. The centroid can be obtained as follows:

$$\bar{y} = \frac{W_1E_1t_1(t_1/2+t_2+t_3)+W_2E_2t_2(t_2/2+t_3)+W_3E_3t_3(t_3/2)}{W_1E_1t_1+W_2E_2t_2+W_3E_3t_3} \tag{4.19}$$

The moment of inertia can be given:

$$I_x = \frac{W_1 t_1^3 + W_2 t_2^3 + W_3 t_3^3}{12} + W_1 t_1 (\frac{t_1}{2} + t_2 + t_3 - \bar{y})^2 + W_2 t_2 (\frac{t_2}{2} + t_3 - \bar{y})^2 + W_3 t_3 (\frac{t_3}{2} - \bar{y})^2 \quad (4.20)$$

and finally the equivalent cantilever stiffness is achieved as (4.21):

$$EI = E_1 I_x = E_1 [\frac{W_1 t_1^3 + W_2 t_2^3 + W_3 t_3^3}{12} + W_1 t_1 (\frac{t_1}{2} + t_2 + t_3 - \bar{y})^2 + W_2 t_2 (\frac{t_2}{2} + t_3 - \bar{y})^2 + W_3 t_3 (\frac{t_3}{2} - \bar{y})^2] \quad (4.21)$$

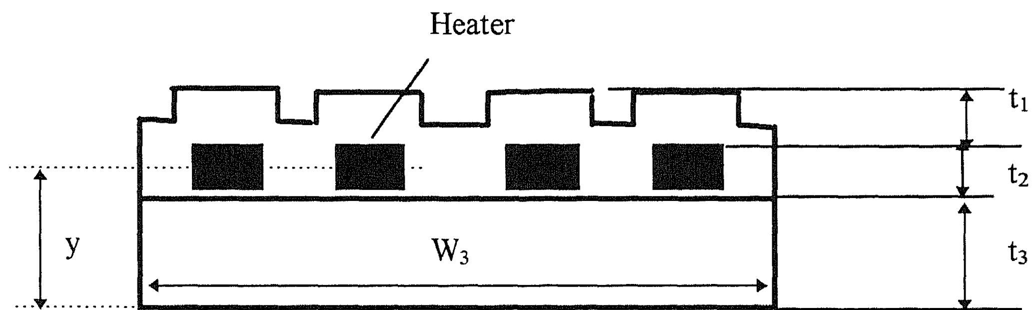

(a) Cross section of CHIPP microprobe

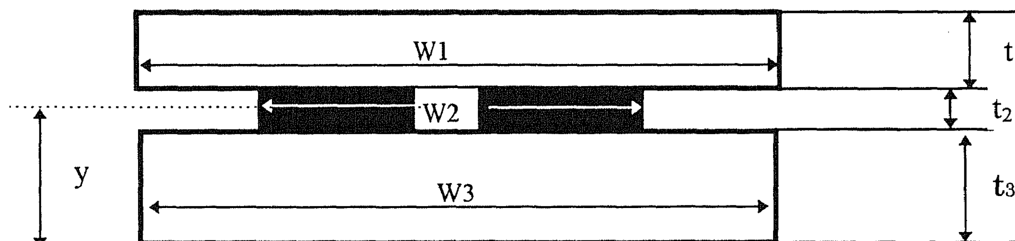

(b) Equivalent cross section of CHIPP probe

Figure 4.4 Equivalent cross section of CHIPP microprobe with three layers.

Similarly the equivalent stiffness for bimorph cantilever is given [44] for which the which the cross section is shown in Figure 4.1:

$$EI = \frac{wt_2^3 t_1 E_1 E_2}{12(E_1 t_1 + E_2 t_2)} K \tag{4.22}$$

$$K = [4 + 6\frac{t_1}{t_2} + 4(\frac{t_1}{t_2})^2 + \frac{E_1}{E_2}(\frac{t_1}{t_2})^3 + \frac{E_2 t_2}{E_1 t_1}] \tag{4.23}$$

4.2 Simulation of Motion of Bimorph Cantilever Structure

4.2.1 Basic Assumption

Cantilever simulation is based on the assumptions at section 4.1 and . Firstly, the cantilever is heated uniformly, temperature gradient due to the heating is neglected. Secondly, only the bimorph cantilever structure is considered, and the heater structure inside the cantilever is simplified using a equivalent cantilever stiffness EI_{eq}. Thirdly, the cantilever original position is assumed at zero - a flat cantilever. For an initially bent cantilever an non-zero value should be subtracted from the total simulated deflections. Finally, only the thermal stress is considered, the external stress and the intrinsic stress is small compared with thermal stress and is neglected.

Jandel Sigmaplot Graphics is used to simulate different cantilever structure based on the formulas in section 4.1 and similar work see reference [46].

Four cantilever structures (Al-SiO_2, Al-Si, Cu-SiO_2 and W-SiO_2) have been used for fabrication of the CHIPP microprobe and are selected for simulations. The parameters of the bimorph cantilever have been listed in Table 3.1 and will be used in the simulations.

4.2.2 Simulations of the Effect of Cantilever Thickness

In design of CHIPP probe card a maximum deflection with a given temperature (or a given input power) is required for the probes moving a distance to make ohmic contact. In order to complete the simulation, the equation (4.11) can be reduced to the following equation:

$$\delta = \frac{3 \cdot \Delta\alpha \cdot \Delta T(1+\frac{t_1}{t_2})L^2}{t_2\{(\frac{W_1}{W_2}\frac{E_1}{E_2})(\frac{t_1}{t_2})^3 + \frac{W_2}{W_1}\frac{E_2}{E_1}(\frac{t_2}{t_1}) + 2[2(\frac{t_1}{t_2})^2 + 3(\frac{t_1}{t_2}) + 2]\}} \tag{4.24}$$

The maximum deflections of the bimorph cantilevers with different materials are simulated as a function of the thickness ratio of two cantilever layers and shown in Figure 4.5.

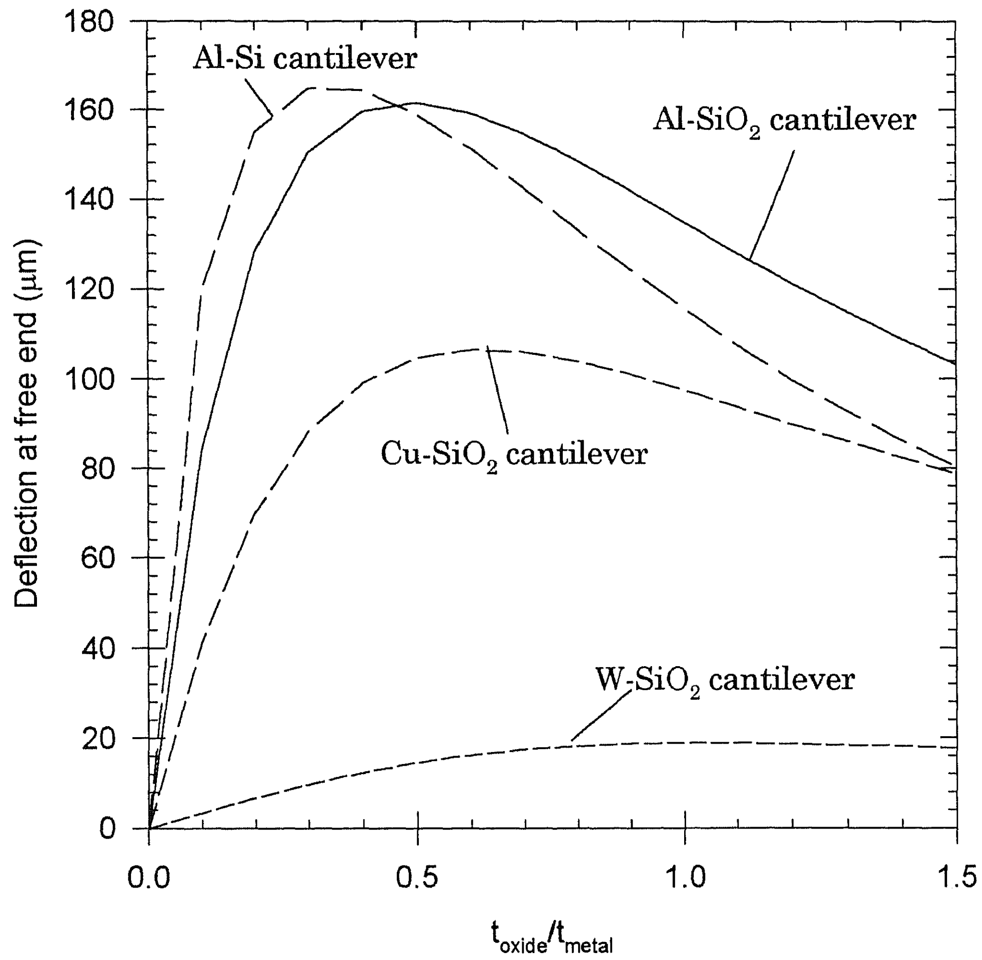

Figure 4.5 Cantilever tip deflection as a function of ratio of bimorph thickness t_{oxide}/t_{metal} for L=400 μm, ΔT=100 °C, and t_{metal}=1 μm.

From Figure 4.5 we can see the deflection δ has a maximum value for a fixed cantilever temperature and length. A very interested thing is that the maximum value of the deflections is not only a function of the cantilever materials but also the ratio of the thicknesses of the bimorph layers. This ratio for the maximum deflection changes when the materials are changed but the other conditions are maintained. The ratio with maximum deflection condition is 0.5 for Al-SiO_2, 0.3 for Al-Si, 0.6 for Cu-SiO_2 and 1.1 for W-SiO_2. In addition, the values of the maximum deflections for different materials depend on both the difference $\Delta\alpha$ of thermal expansion and Young's modulus E. As a result, the Al-Si cantilever has a largest maximum deflection value due to the large Young's modulus of silicon, although the system only has the second large $\Delta\alpha$ compared with the Al-SiO_2 bimorph. The Al-SiO_2 system obtains the second large maximum deflection value. Cu-SiO_2 and W-SiO_2 cantilevers give smaller maximum deflection as expected.

4.2.3 Simulation of the Deflections at the Probe Tip

In real probe card operation the probes are controlled by input power. The deflections at the probe tips have been simulated as a function of the cantilever temperature with four cantilever structures using equation (4.42). The simulation results are shown in Figures 4.6-4.9. The results show that the deflection of the cantilever is linearly proportional to the temperature rise ΔT, but inversely proportional to the thickness of the metal and oxide. The Al-Si cantilever system has largest deflection range (reaching 400 μm at 250°C) compared with the other cantilever systems at the same conditions of cantilever length,

thickness and temperature. The W-SiO_2 cantilever system has a smallest deflection range (about 50 μm at 250°C).

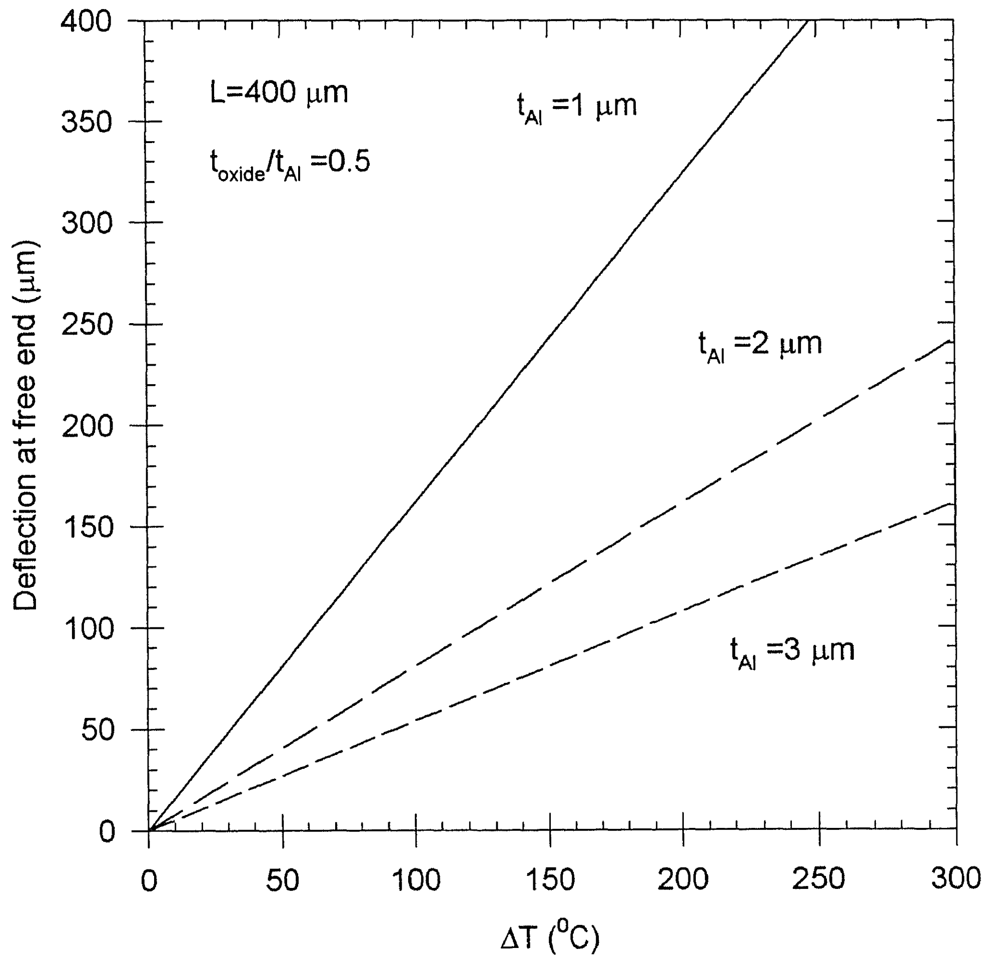

Figure 4.6 Tip deflection as a function of temperature rise ΔT for Al-SiO_2 cantilever at L=400 μm, t_{oxide}/t_{metal}=0.5 and three different Al thicknesses.

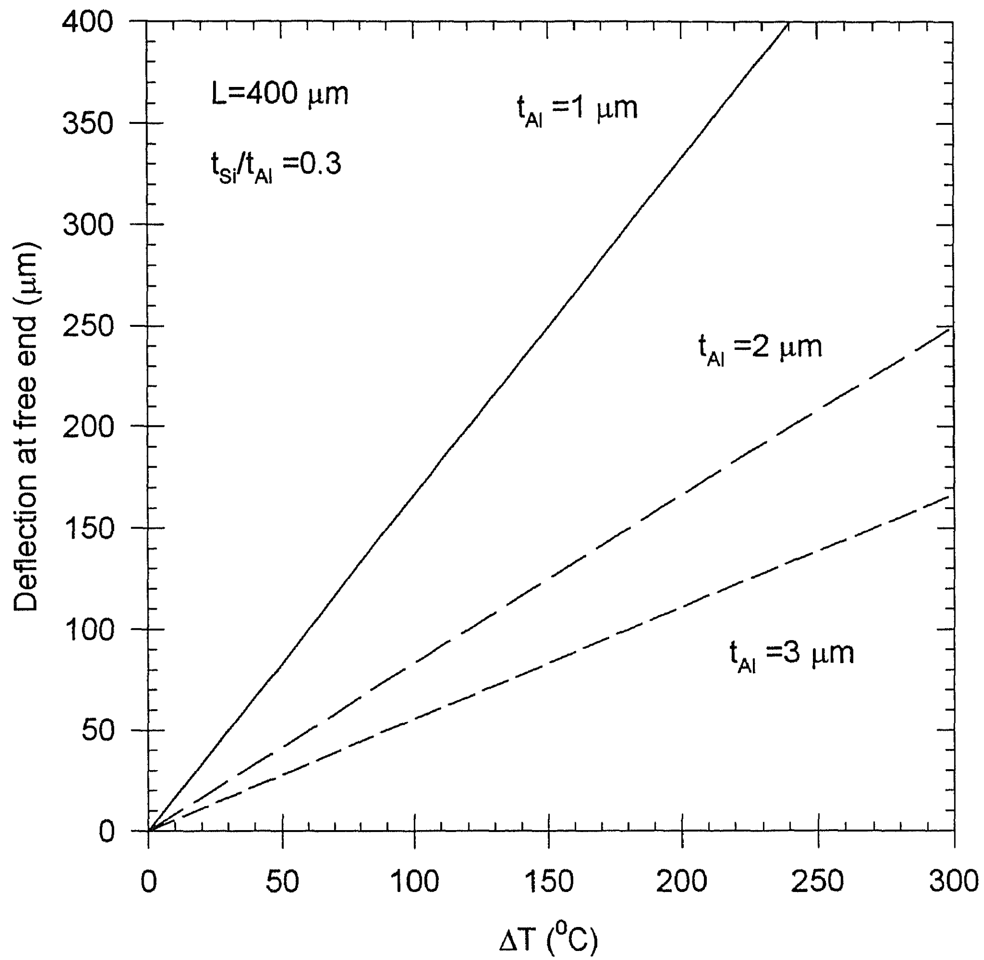

Figure 4.7 Tip deflection as a function of temperature rise ΔT for Al-Si cantilever at L=400 μm, t_{si}/t_{Al}=0.3 and three different Al thicknesses.

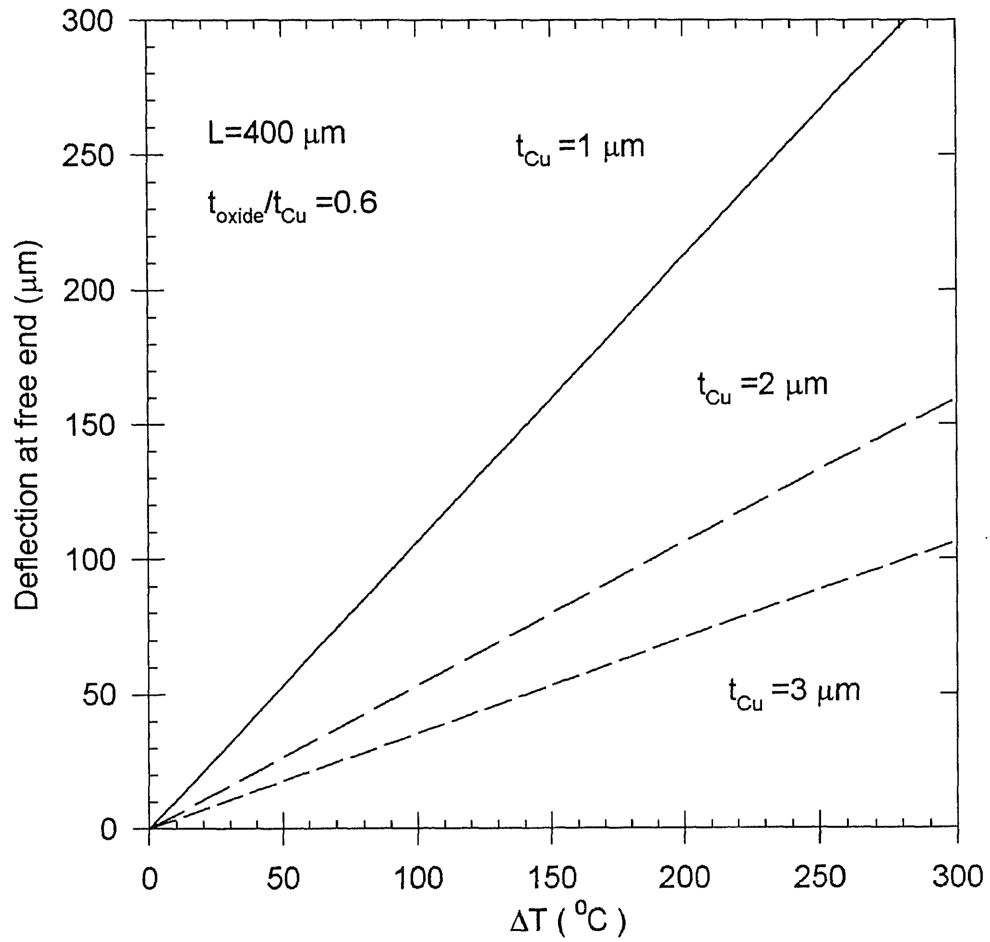

Figure 4.8 Tip deflection as a function of temperature rise ΔT for Cu-SiO_2 cantilever at L=400 μm, t_{oxide}/t_{Cu}=0.6 and three different Cu thicknesses.

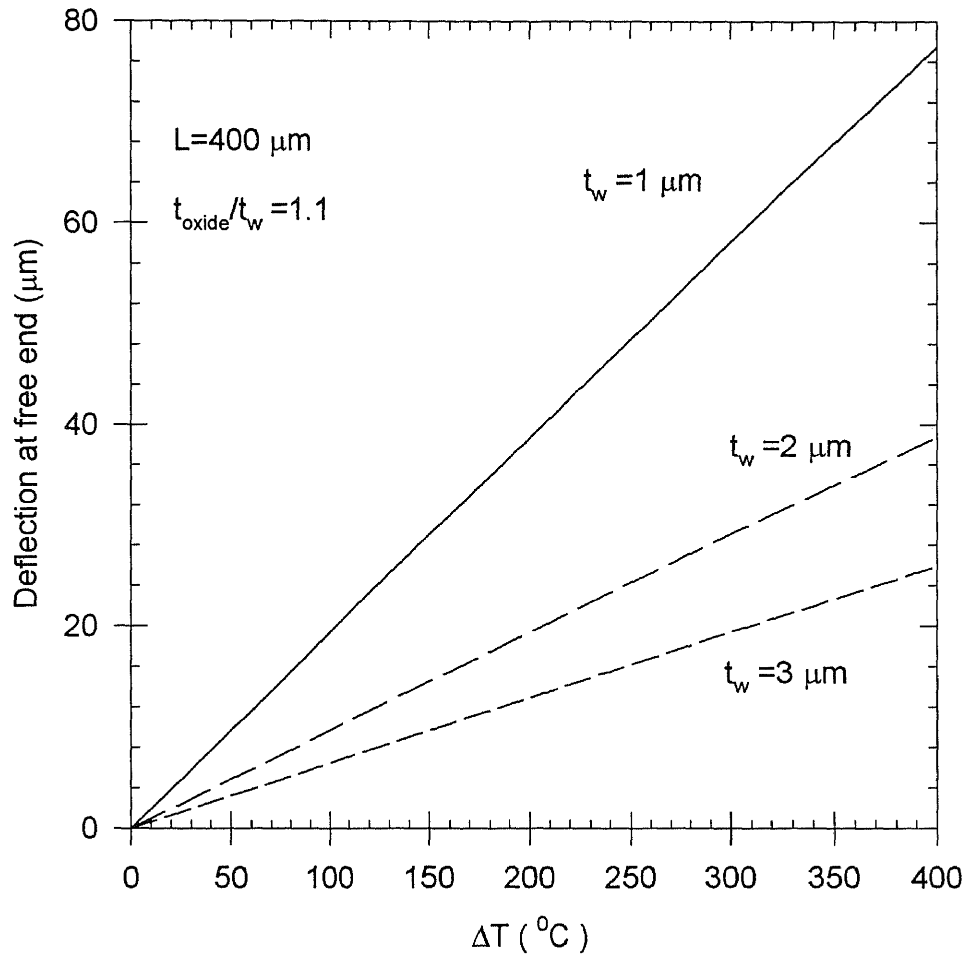

Figure 4.9 Tip deflection as a function of temperature rise ΔT for W-SiO_2 cantilever at L=400 μm, t_{oxide}/t_W=1.1 and three different W thicknesses.

4.2.4 Forces Applied by Cantilever Tips

The tip force generated by the cantilever is due to the bending moment caused by thermal expansion of the two materials. When the tip of the cantilever is bent to make contact with a test pad, it first touches the test pad, and then the extra force will be applied at the tip with continued bending of the cantilever due to raise of the input power. In order to simplify the simulation, a flat cantilever condition is considered, and a zero moving distance is chosen.

Figures 4.10-4.13 show the force applied by tip as a function of temperature rise ΔT for the Al-SiO_2, Al-Si, Cu-SiO_2 and W-SiO_2 systems with three cantilever thicknesses. The forces at the tips in these figures are linearly proportional to the temperature rise ΔT and the cantilever thickness. The largest force applied at the cantilever tips is still found with the Al-Si bimorph with 500 μN at t_{Al} =3 μm and ΔT=250°C. The smallest force goes to W-SiO_2 with 150 μN at t_{Al} =3 μm and ΔT=250°C.

In order to increase the tip force we can increase ΔT or the cantilever thickness. However, the cantilever deflection is inversely proportional to the cantilever thickness (see Figures 4.6-4.9), increase of the cantilever thickness will cause cantilever deflection decrease. The CHIPP microprobe requires large force (for ohmic contact) and large deflection (for moving distance). This implies a thick cantilever size may not satisfy the deflection requirements although it increase the tip force. A solution which can obtain both large force and large deflection is to increase the cantilever width. The tip force is a function of cantilever width (see Figure 4.14) but the cantilever deflection is not (see equation (4.24 or 4.10)), which means we can increase cantilever tip force through

increasing cantilever width without decreasing cantilever deflection. A large deflection with large tip force is an advantage in design of the CHIPP probe card.

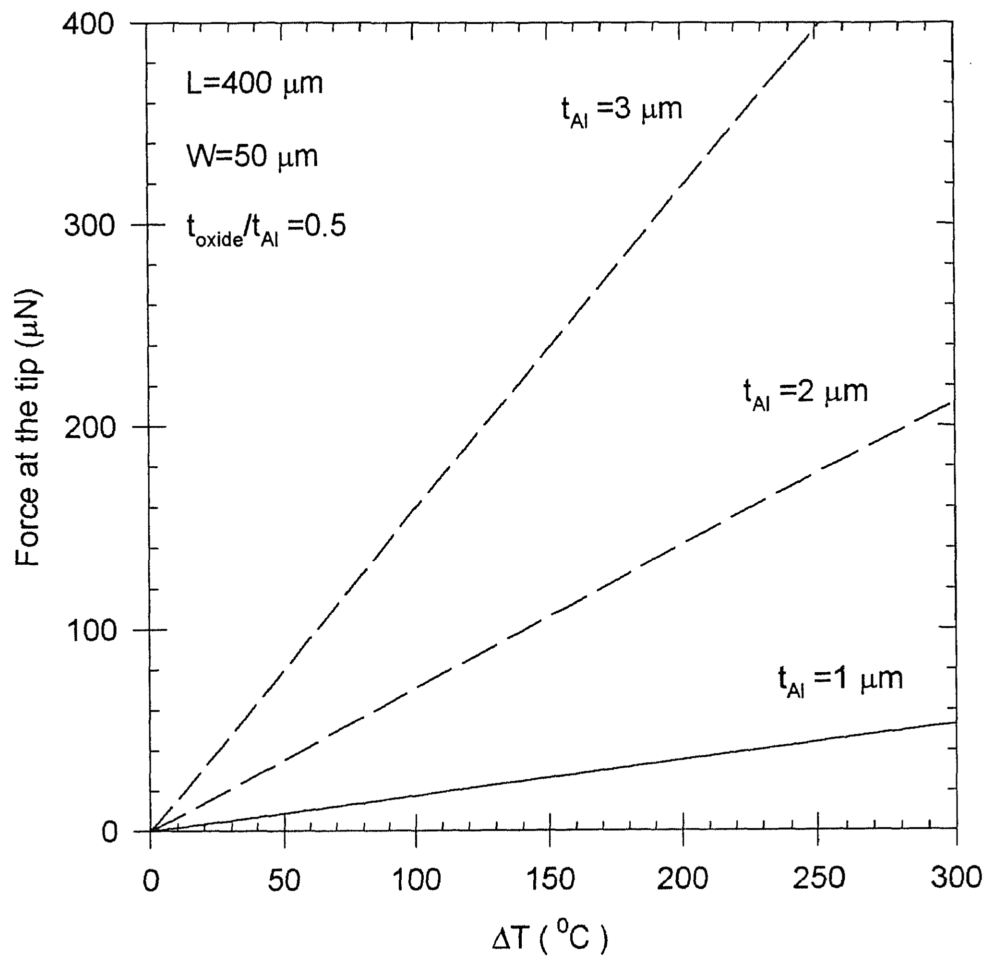

Figure 4.10 Force applied by tip as a function of temperature rise ΔT for Al-SiO_2 cantilever with three Al thicknesses.

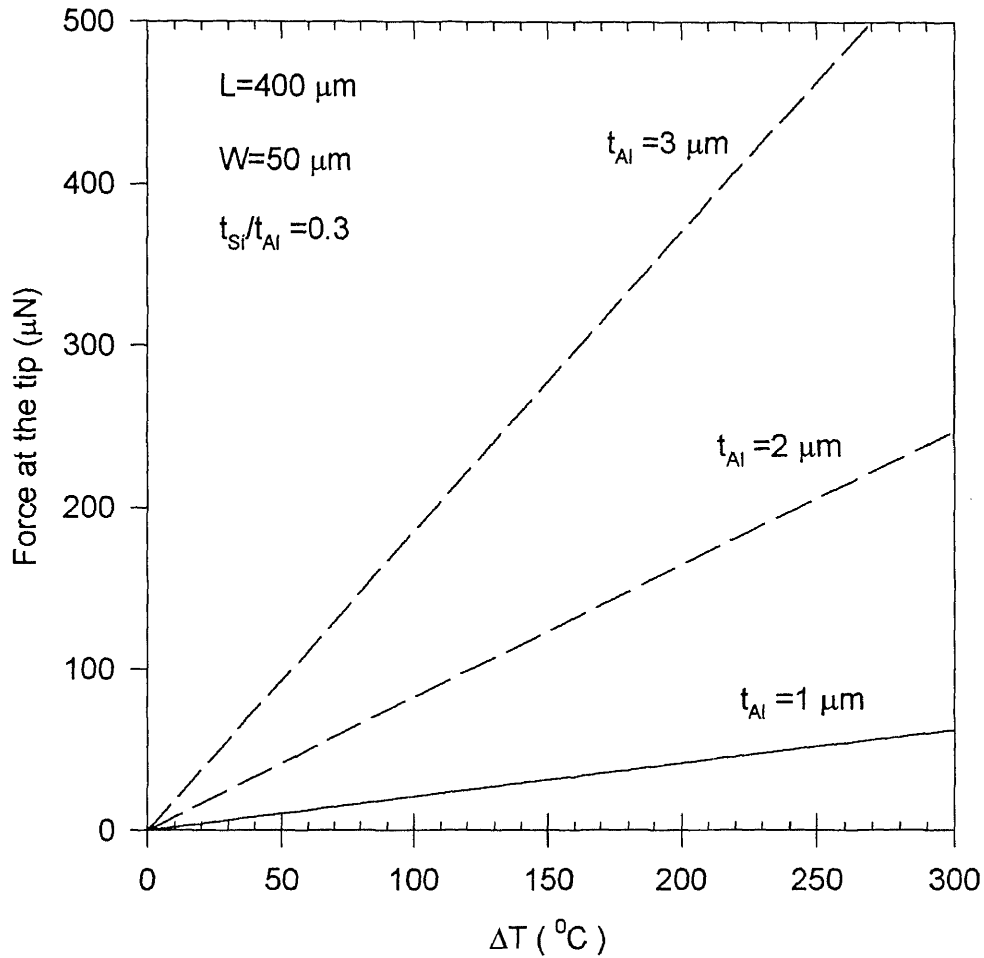

Figure 4.11 Force applied by tip as a function of temperature rise ΔT for Al-Si cantilever with three Al thicknesses.

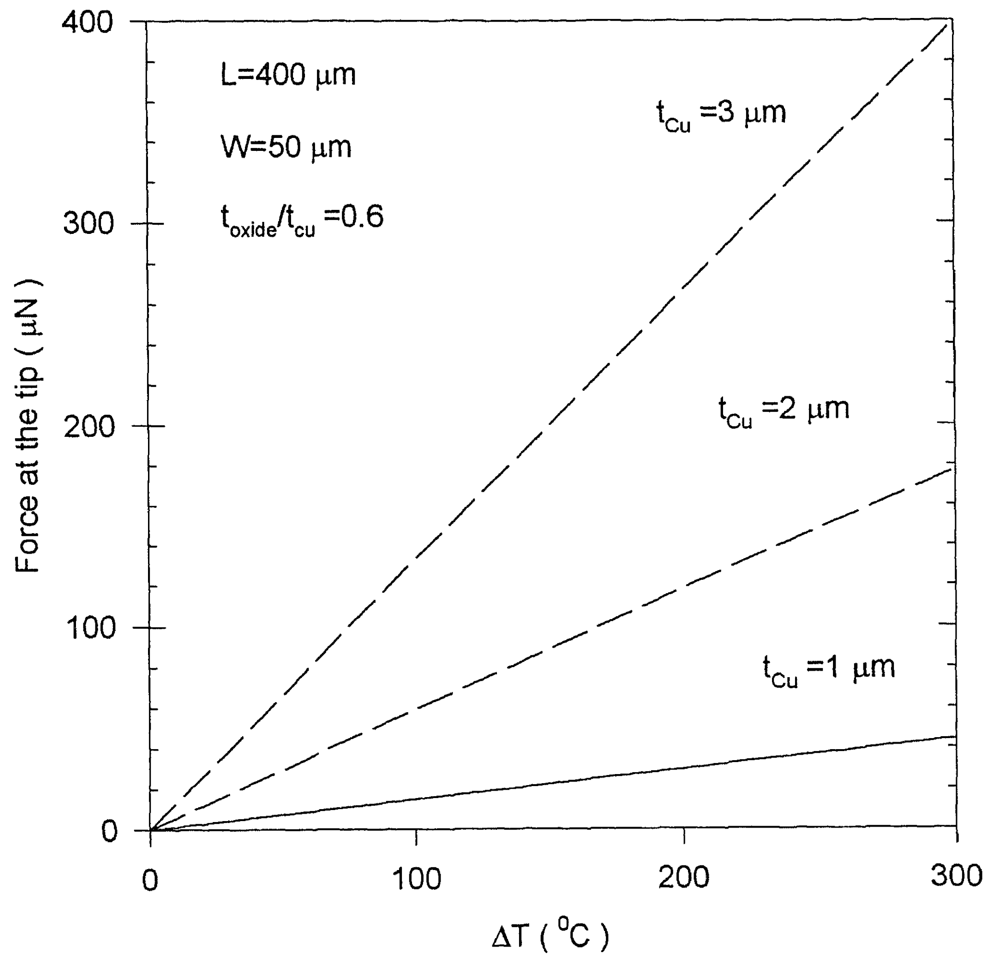

Figure 4.12 Force applied by tip as a function of temperature rise ΔT for Cu-SiO_2 cantilever with three Cu thicknesses.

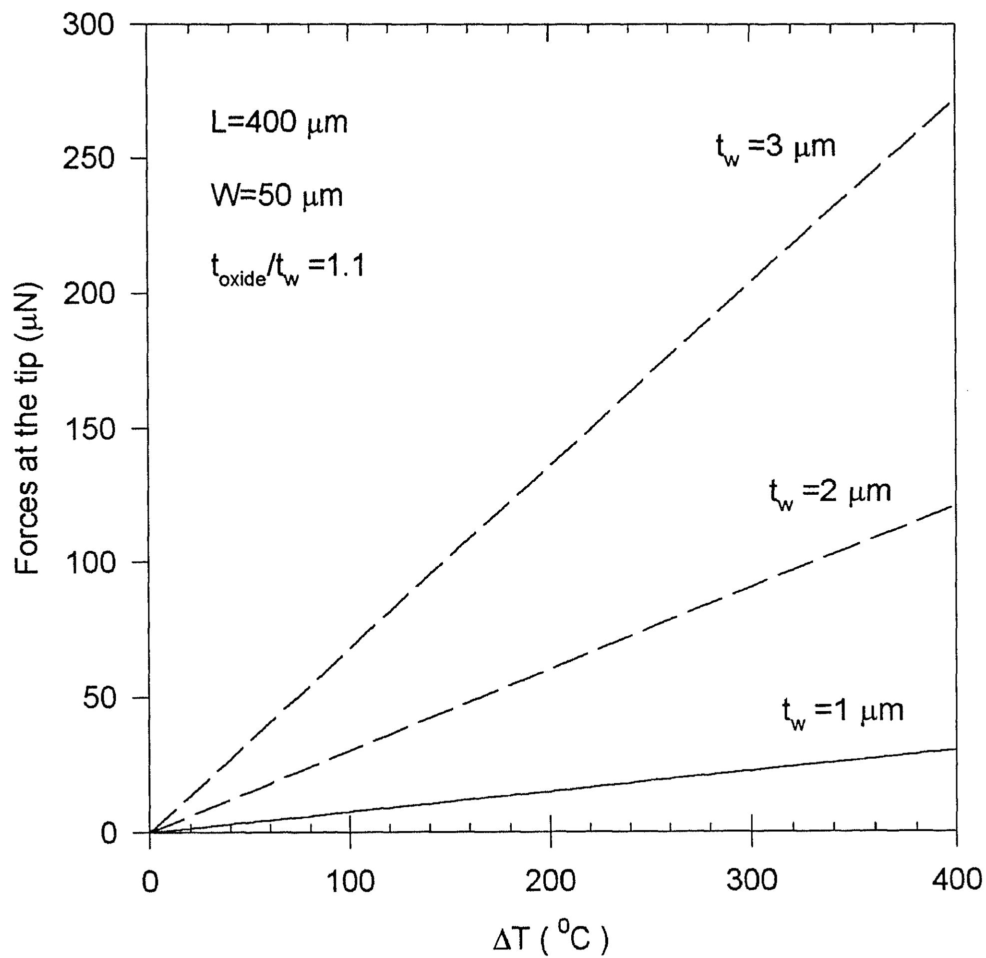

Figure 4.13 Force applied by tip as a function of temperature rise ΔT for W-SiO_2 cantilever with three W thicknesses

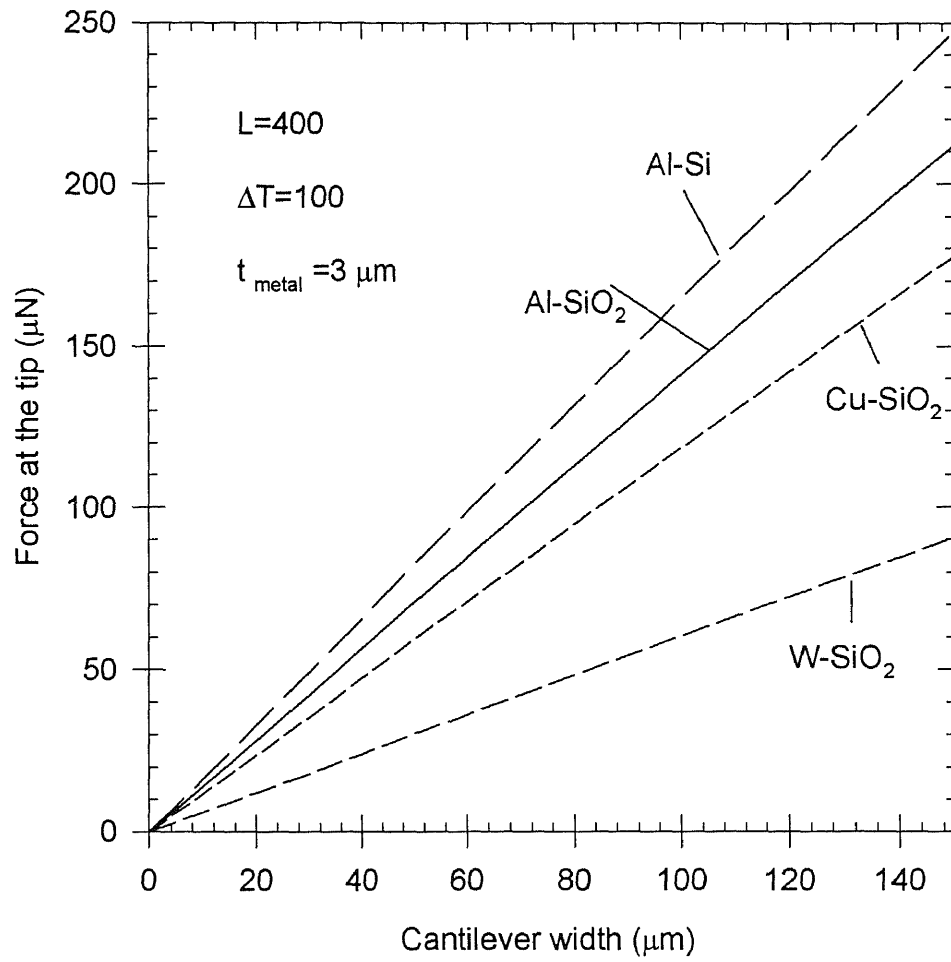

Figure 4.14 Force applied by tip as a function of the cantilever width for four different bimorph cantilevers

CHAPTER 5

FABRICATION

Fabrication was carried out in the class 10 clean room in NJIT. The first device made was a Al-SiO_2 bimorph structure with $TaSi_2$ heater and Au contact tip. Because Al has low a melting point, the Al-SiO_2 cantilever structure cannot used for diamond deposition, which occurs over 900°C. A second device has a W-SiO_2 bimorph structure with W heater and three different contact tip materials: conducting diamond, gold, and tungsten. This fabrication is complicated and difficult due to the conducting diamond and tungsten.

5.1 Fabrication of Al-SiO_2 Type Probe Card

The process flow for a prototype version of Al-SiO_2 probe card is illustrated in Figure 5.1. The cantilevers are made of sputtering aluminum and Low Temperature Oxide (LTO) SiO_2, heaters are sputtering $TaSi_2$, and the probe tips and pads are made of gold.

All of the experiments have been performed on (100) oriented, 100 mm-diameter silicon wafers. The first step is to mask the wafer for future potassium hydroxide (KOH) etch which will be used for the release of the probe card. A low pressure chemical vapor deposition (LPCVD) of silicon nitride (Si_3N_4) is deposited on both sides of wafers, the silicon nitride film on front side is for KOH etch stop and the film on back side is for KOH etch mask. Silicon nitride has an etch rate of almost zero in KOH. The etch rate of lightly to moderately doped silicon is approximately 50 μm/hr at 80°C. A 0.12 to 0.2 μm thick nitride film is sufficient to mask the KOH etch. Because silicon nitride film has high-stress, generally film thickness of larger than 0.3 μm will cause film cracking. Before LPCVD of silicon nitride a thin SiO_2 film of 500A was grown using dry thermal oxidation,

which provides a good adhesion layer for silicon nitride. The following step is to deposit 1-μm LTO SiO_2 for protection layer on both surfaces of the wafers. The SiO_2 film on the front side will be used as a adhesion layer between Si_3N_4 and the metal film, and also used as a protection layer for final dry release. KOH is not uniform, and because the thin Si_3N_4/SiO_2 film cannot withstand the long etch needed to remove all the silicon, some silicon may still remain on backside of the wafer after KOH etch. This remaining silicon has to be etched using SF_6 based RIE. The SF_6 plasma may damages the tungsten metal, and the SiO_2 film which has 6:1 selectivity with silicon during SF_6 RIE etch is used to protect the tungsten metal. The SiO_2 is etched using CF_4-CHF_3 based plasma which dose not etch tungsten. The SiO_2 film on the backside is to prevent mechanical damage during wafer processing.

The aluminum metal that will form the cantilever beam and signal line is deposited next. Sputtering deposition is used in different thickness from 0.6 μm to 3 μm. The aluminum is patterned and then etched with H_3PO_4.

A second layer of LTO is then deposited on the front side of the wafer. This film is 0.3 - 0.4 μm thick and serves as an insulation layer between the aluminum signal line and heater. The insulation layer of 0.3 μm is minimum because Al may diffuse to LTO at 425°C. A diffusion barrier layer may be required to block the aluminum diffusion such as PECVD SiO_2 instead of LTO. A tungsten layer is usually deposited and serve as a diffusion barrier layer before LTO deposition because tungsten has very high melting point. The tungsten layer can be etched with a SF_6-based RIE etch.

The heater layer of 0.5 μm $TaSi_2$ is then deposited by sputtering. The maximum thickness of $TaSi_2$ deposited by sputtering is 0.7-1.0 μm depended on the deposition

temperatures; above this limit the film will crack. $TaSi_2$ is patterned and etched with a two step dry etch process. The $TaSi_2$ is etched with a SF_6 based RIE etch, while the LTO is etched with a CF_4-CHF_3 based RIE etch.

The next step is to deposit the third layer of 1μm LTO that serves as a top insulation layer and a low thermal expansion layer for the bimorph cantilever. The LTO layer is then patterned and etched with CF_4-CHF_3 RIE etch to open windows for the probe pads and tips.

The next step is to deposit gold for the probe contact tips and pads using lift-off. A carefully prepared photoresist with 10 μm thickness is used for lift-off. A 0.5 μm gold film is deposited by sputtering and then lifted off in acetone (2 minutes with ultrasonic vibration; 2-4 hours without ultrasound).

After carefully cleaning, the Si_3N_4 on the back side is patterned to serve as a mask against KOH etching. The probe card device on the front side of the wafer must be properly protected. Great care is taken to prevent any scratches: for example, only plastic holders are used to spin on photoresist on the wafer. For this reason the first step in patterning the wafer is to spin on a protective coating of photoresist on the front side of the wafer. This coating is generally a few micrometers thick, and then hardened with a 115^0C bake for 20min. Conventional IC infrared lithography is then utilized to pattern the photoresist on the back side of the wafer. A CF_4- CHF_3 based RIE is then used to etch the exposed areas on the back side of the wafer, the first layer is 1-μm LTO, the next is 0.12 μm Si_3N_4 and the third layer is 500A thermal SiO_2 . A CF_4 based RIE instead of a CF_6 based RIE is used for Si_3N_4 dry etch because SF_6 based RIE also attacks the Si (100) surface.

After the LTO/nitride layer patterning, the photoresist is stripped prior to the KOH etch. A special holder is used for the device protection on front side of the wafer during KOH etch. The holder is used instead of a conventional LPCVD nitride layer because the deposition temperature of LPCVD nitride is 770^{0}C, too high for metals used in the device. A 4 μm thick photoresist is coated on front side of the wafer with 115^{0}C bake for 30 min prior to the KOH to protect the devices. Another blank silicon wafer coated with thick photoresist without bake on its front side is used to bond with the device wafer face to face, the two wafers are then hardened with a 115^{0}C bake for 60-90 min. This process is used to support a thin nitride film for KOH etch and also to hold the device for dry RIE release in last step.

The KOH etch is a mixture of 45% KOH in water. The solution is heated to 80^{0}C in a Teflon beaker in a stainless steel water bath. A convex lid is placed over the beaker which causes condensation of the solution to be dripped back into the beaker, maintaining a constant chemical composition and therefore constant etch rate. The double polished silicon wafer starts out approximately 450 μm thick. The KOH etch takes approximately 8 h to complete. The wafers are placed vertically, so that the gaseous by-products can escape without hindering the etch. When the wafer is etched through silicon, the etch is stopped on the nitride. Visual inspection is used to tell when the LTO thin film is penetrated. The KOH etch has a very high selectivity between the (100) and (111) plane of silicon. This causes the silicon wafer to be etched at 54.7^0 angle (i.e. along a (111) plane) with respect to the surface of the (100)-oriented wafer.

After KOH etch the wafer is cleaned using DI water. The wafer is then baked at 150C for 30-60 min to harden the bonded wafer prior to the RIE etch. The next step is to

remove the remaining substrate silicon from device cantilever areas. The back side of the wafer is subjected to a SF_6 based RIE etch that has selectivity of 8:1 between silicon and oxide. The etch takes approximately 30-40 min to complete. The first layer of deposited LTO serves as an etch stop to protect the cantilever.

The last step is to release the device. A CF_4- CHF_3 based RIE etch is used to remove the LTO layer, which is protected in aluminum cantilever areas or in photoresist areas on the front side. The cantilevers are still stuck to photoresist of the front wafer during the RIE etch, which protect the front surface of the cantilever without attack by plasma etch. The photoresist is then stripped carefully with M-pyrol and acetone, following DI water and alcohol clean, then baked at 115°C for 5 minutes. A O_2-plasma is used to clear the remaining photoresist. The fabrication of the probe card is then completed.

The sequence of the fabrication procedure can be summarized with the following steps:

1. Wafer clean, thermal oxidation (500A)
2. LPCVD Si_3N_4 deposition (1200-2000A) on both sides of the wafers
3. First LPCVD SiO_2 deposition (1 μm) on both sides of the wafers
4. Al sputter deposition (1-3 μm) on the front side
5. Al patterning and wet etch
6. W sputter (2000A) on the front side of Al for diffusion stop layer
7. Second LPCVD SiO_2 deposition (3000-4000A) on the front side
8. Heater layer of $TaSi_2$ sputter deposition on the front side

9. Heater patterning and RIE $TaSi_2$ and LTO and W
10. Third LPCVD SiO_2 deposition (0.6-1.2 μm)
11. LTO patterning and RIE SiO_2 to open widows
12. Cr\Au sputtering deposition (0.5 μm) and lift-off
13. Metal annealing
14. Backside photo and RIE LTO and Si_3N_4
15. KOH etching
16. RIE Si/Si_3N_4/LTO for cantilever release
17. Photoresist strip
18. O_2 plasma clear

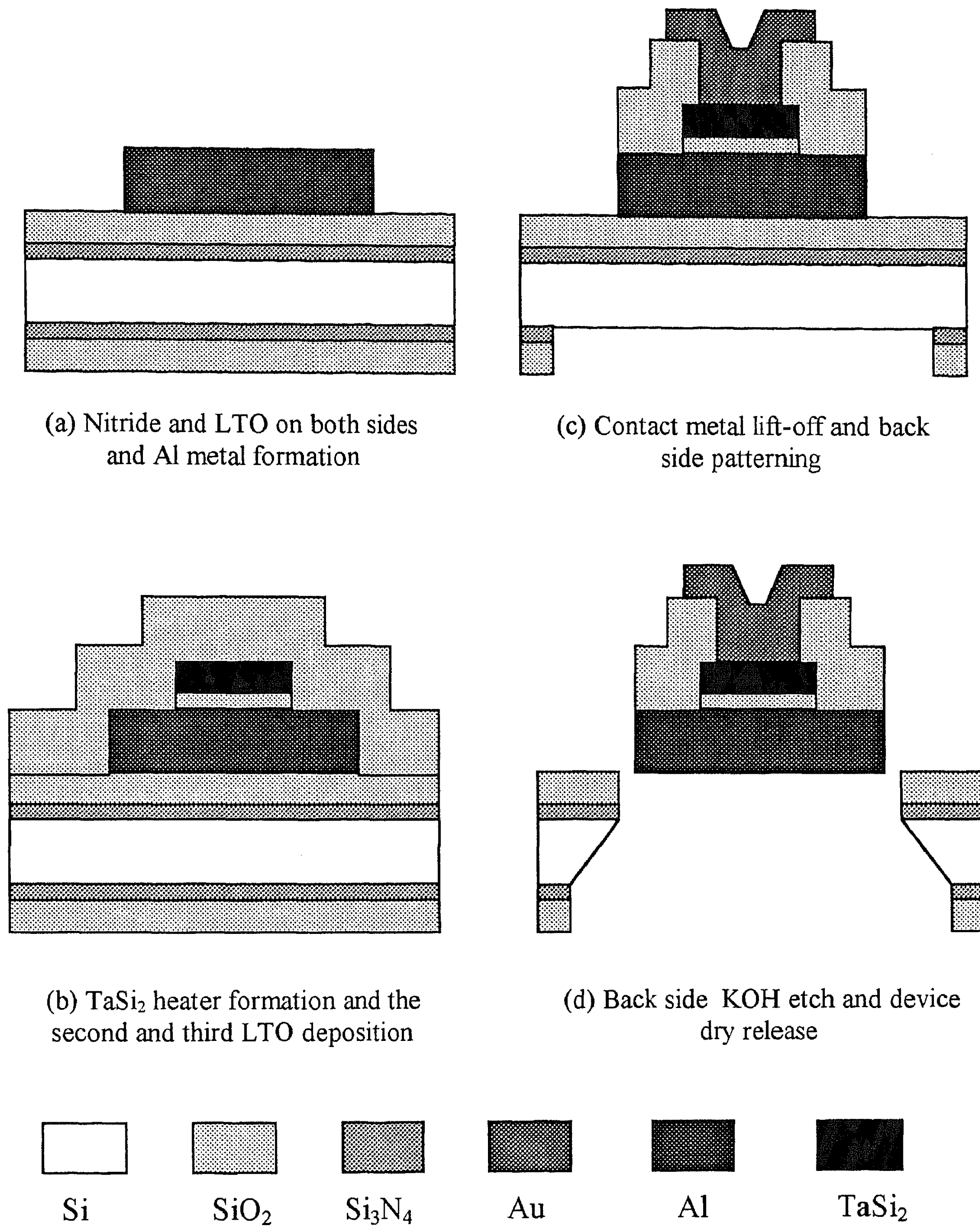

Figure 5.1 Fabrication flow for a prototype probe card using Al-SiO_2 cantilever with gold contact tip.

5.2 Fabrication of W-SiO_2 Type Probe Card

Fabrication of the W-SiO_2 based cantilever probe card is similar to the Al-SiO_2 structure. However the major difference is that tungsten has very high melting point so that conducting diamond deposition is possible. Tungsten also has very high stiffness, which can make scrub possible.

5.2.1 Gold and Tungsten Tip Structure

The process flow for W-SiO_2 probe card with gold and tungsten tips is shown Figure 5.2. The heater material is now changed to tungsten because $TaSi_2$ has larger coefficient of thermal expansion than tungsten, which could reduce cantilever bending force during the cantilever heating. The contact pad material is gold.

The first few process steps are the same as Al-SiO_2 structure except tungsten sputtering deposition is used instead of aluminum deposition. Because tungsten has large stiffness it cracks easily during sputtering. A 0.1 μm titanium adhesion layer is deposited prior to the tungsten deposition for adhesion if Ti thickness is smaller than 0.1 μm the W film may be lift. Because large sputtering power produces a lowering of electrical conductivity in tungsten, the deposition of tungsten uses 200W d.c. power. The tungsten film is 1 μm thick. Maximum thickness is 1.5 μm due to the film cracking.

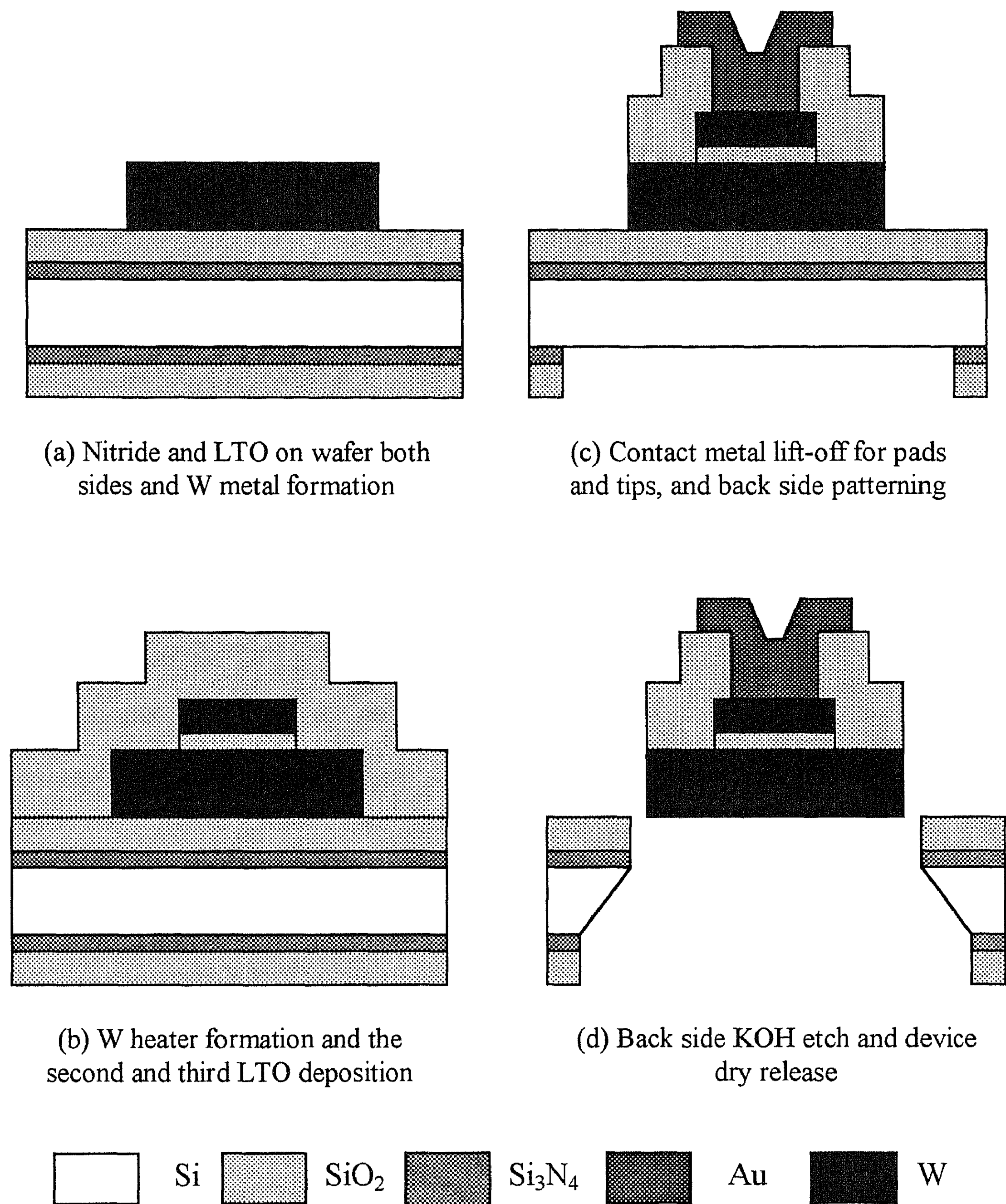

Figure 5.2 Fabrication flow for a prototype probe card using W-SiO2 cantilever with gold and tungsten tips.

After deposition the tungsten metal is annealed at 400 °C for half hour to reduce stress, it is then possible to continue deposition in order to obtain a thicker tungsten film. The tungsten is patterned and then etched with a SF_6-based plasma etch, first through the tungsten then the titanium, finally stopping on the SiO_2 surface.

The heater material is also tungsten with the same process as above but 0.5 μm thickness. The remaining processing steps are the same as Al-SiO_2 with gold contact tips, but with a slight difference. For the tungsten tip structure a separate lift-off process is required, which is first to deposit and lift-off gold metal for pads, then deposit and lift-off tungsten metal for tip.

The process steps are given as follows:

1. Wafer clean, thermal oxidation (500A)
2. LPCVD Si_3N_4 deposition (1200-2000A) on both sides of the wafers
3. First LPCVD SiO_2 deposition (1 μm) on both sides of the wafers
4. W sputtering deposition (1 μm) for the first cantilever layer
5. W patterning and SF_6 based RIE etch
6. Second LPCVD SiO_2 deposition (3000-4000A) for insulation
7. W sputtering deposition for heater
8. Heater patterning and SF_6-RIE W and CF_4-RIE LTO
9. Third LPCVD SiO2 deposition (1.2 μm) for the second cantilever layer
10. LTO patter and RIE SiO2 to open widows
11. Cr\Au sputter deposition (0.5 μm) and lift-off for pads
12. W sputtering deposition (0.5 μm) and lift-off for tips

13. Metal annealing

14. Backside photo lithography and RIE LTO and Si_3N_4

15. KOH etching

16. RIE Si/Si_3N_4/LTO for cantilever release

17. Photoresist strip

18. O_2 plasma clear

5.2.2 Conducting Diamond Tip Structure

Figure 5.3 shows the process flows for a W-SiO_2 cantilever structure with conducting diamond tip. The tungsten is used to serve as a substrate for diamond deposition. The process starts with a Si (100) wafer. The first step is to grow Si_3N_4 and LTO layers on both sides of the wafer for KOH mask and stop layer, similar to the Al-SiO_2 cantilever processes described above. The tungsten metal that forms the bottom part of the bimorph is deposited next. It consists of a 1 μm tungsten film with a 0.1 μm titanium adhesion layer. The metal is patterned and then etched with a two step dry etch process (first tungsten, next titanium) with a SF_6 based plasma etch. Then tungsten is then annealed at 400^0C with forming gas for 30 minutes to reduce film stress.

A second layer of 0.3 μm LTO is then deposited. This LTO film is a protection layer for future diamond RIE etch, and provides an insulating cover for the cantilever. The LTO is patterned and dry etched in a CHF_3-CF_4 based plasma, which provides the small openings in the LTO film to the tip of tungsten cantilever. This openings will be used to serve as a base for diamond film deposition to form diamond/W tips.

The wafers covered by LTO with tungsten windows are carefully cleaned, then sent to sp^3 Inc. in California for diamond deposition. A CVD deposition at 900-1000°C is used to grow about 1.5 μm thick conducting diamond on the front side of the wafer. This diamond film is used to form a micro probe tip for scrub contact.

The patterning of the diamond tip uses a conventional IC photolithography process. The first step is to deposit an aluminum film on front side of the wafer. This film is 0.8 μm thick and serves as a metal masking layer for dry etching the diamond film. The aluminum is patterned and then etched in H_3PO_4. After stripping photoresist the diamond film is etched with an O_2-based plasma. A great care is necessary for diamond etch because the etch is very different from conventional film etching. Conventional etching is basically uniform or faster at the edge of the wafer, however, the diamond film etch is not uniform, and etching in the center of the wafer is faster than at the edge. In the same area, the diamond film etch is also not uniform, and many diamond islands on LTO remain after most of the diamond film are etched away. These islands could be certain diamond crystal orientations. Much longer RIE etch times are needed to clear these diamond islands, and the time could be doubled until islands disappear. Therefore a LTO protection layer must be used for metal surface protection. The LTO film is then removed by CF_4-CHF_3 based plasma. The Al mask is stripped by wet chemical etch.

The next step is to deposit 0.3 μm LTO film for the insulation layer between the W bimorph layer and the heater layer. Then tungsten metal for the heater is deposited by sputtering. The film is 0.5 μm thick. The tungsten film is annealed at 400^0C for 30 minutes following deposition. The tungsten is patterned and dry etched in a SF_6 based plasma.

A fourth layer of LTO is then deposited on the front side of the wafer. This film is 1.2 μm and serve as a top lever of the cantilever. After patterning of the LTO film a CHF_3-CF_4 based RIE is used to open windows for conducting diamond tips and contact pads. Then gold metal is deposited for contact pads using the lift-off method.

The following steps are used to release the device. These steps are similar to the Al-SiO_2 structure process. The whole process flow is summarized as follows:

Process flow for W-SO2 cantilever with conducting diamond tips;

1. Wafer clean, thermal oxidation (500A)
2. LPCVD Si_3N_4 deposition (1200-2000A) on both sides of the wafers
3. The first LPCVD SiO_2 deposition (1 μm) on both sides of the wafers
4. W sputtering deposition (1 μm) for the first cantilever layer
5. W patterning and SF_6 based RIE etch
6. W annealing at 400^0C forming gas for 30 min
7. The second LPCVD SiO_2 deposition (3000-4000A) for RIE protection and insulation
8. LTO patterning and CF_4-CHF_3 based RIE etch to open window for diamond deposition
9. CVD conducting diamond deposition(1.5 μm)
10. Al sputtering deposition for diamond mask (0.8 μm)
11. Al film patterning and wet etch
12. Diamond film etch using O_2 plasma
13. LTO film strip using CHF_3 based plasma
14. Al mask strip through wet chemical etch

15. The third LPCVD SiO_2 deposition (3000-4000A) for insulation

16. W sputtering deposition for heater

17. Heater patterning and SF_6-RIE W and CF_4-RIE LTO

18. The 4 LPCVD SiO_2 deposition (1.0-1.2 μm) for the second bimorph layer

19. LTO patterning and RIE SiO_2 to open widows for tips and pads

20. Cr\Au sputtering deposition (0.5 μm) and lift-off for pads

21. Backside photo lithography and LTO and Si_3N_4 etch through CHF_3 based RIE

22. KOH etching

23. RIE Si/Si_3N_4/LTO for cantilever release

24. Photoresist strip

25. O_2 plasma clear

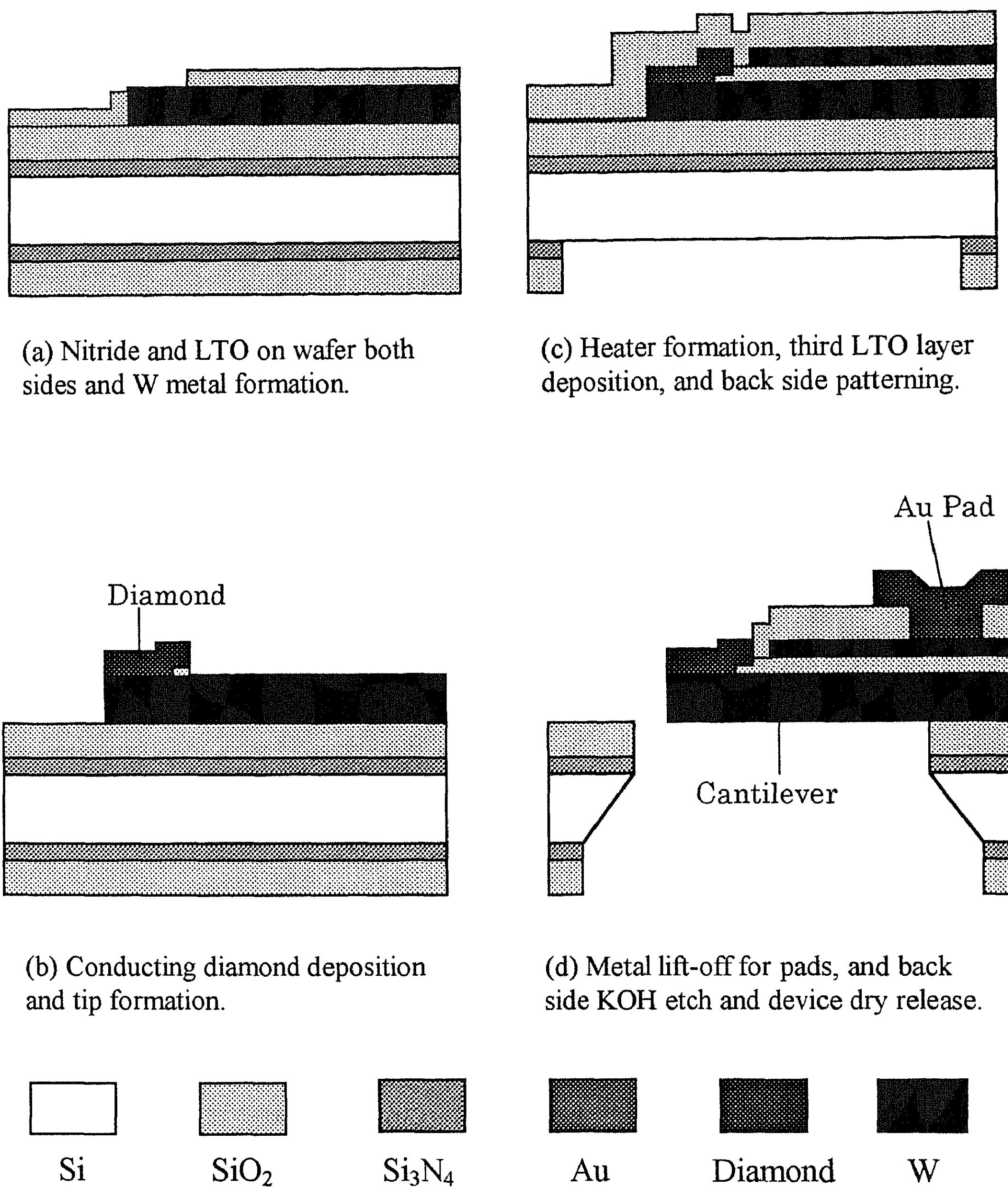

(a) Nitride and LTO on wafer both sides and W metal formation.

(c) Heater formation, third LTO layer deposition, and back side patterning.

(b) Conducting diamond deposition and tip formation.

(d) Metal lift-off for pads, and back side KOH etch and device dry release.

Figure 5.3 Fabrication flow for a prototype probe card using W-SiO2 cantilever with conducting diamond tip.

6.3 Mask Design

Complete processing requires six masks. Masks are designed using a Mentor Graphic IC station. The file is then transferred to gds2 file and sent to a commercial company for fabrication. The first mask is used for cantilever metal patterning. The second mask is used to form the heater. The third is used for the top bimorph formation and also for the device pad and tip openings. The fourth mask is used for the device pad lift off included heater and signal wire pads. The gold lift-off and diamond opening window are achieved by the fifth mask. The final mask is for backside KOH etching.

6.4 Adhesion Consideration and Experiments

The adhesion of grown and deposited films used in the CHIPP probe card must be excellent (both as deposited, and after subsequent processing). If films lift from the substrate device failure can result, and thus poor adhesion represents a potential reliability problem.

Adhesion can be effected by many physical and chemical factors. First for low values of adhesion, it is surmised that the electron shells of the adsorbed atoms remain intact, and these atoms are held to the surface by Van der Waals forces[34]. These forces apply to a bonding energy less than approximately 0.4 eV, and the atoms are said to be physisorbed on the substrate. Above 0.4 eV, sharing of electrons between the film and substrate occurs, and the atoms are chemisorbed. Generally adhesion is greater the higher the adsorption energy of the deposit and /or the higher the number of nucleation centers in early growth stage of the film. Chemisorption due to an intermediate-layer formation that allows a continuous transition from one lattice to the other and results in excellent

adhesion. This particularly true for the adhesion from of strong oxide forms. If intermetallic metal alloys form, adhesion is also improved. Adhesion is also strongly effected by the cleanliness of the substrate. Contamination generally results in reduced adhesion, as does an adsorbed gas layer. Cleaning the substrate prior to deposition is therefore important to insure good adhesion. Finally, substrate surface roughness can also effect adhesion, because a rough substrate exhibits more surface area than a smooth surface, and mechanical interlocking between the film and substrate may occur.

In order to obtain good adhesion between metals and silicon oxide, and between metal and diamond, a large number of adhesion experiments were performed. Diamond deposition temperature is around 900-1000^{0}C, and high melting point metal, like Ta and W are required. Three metals were considered: W, Ta, and Cu.

Ta has been deposited under different conditions. A maximum Ta thickness of 5000A with good adhesion to LTO surface is found with room temperature sputtering. If the Ta thickness is larger than 5000A, poor adhesion results. Maximum stress is located in center of the wafer. A good solution is to include a layer of a strong oxide-forming element between the oxide and the metallization. A titanium adhesion layer is used between the LTO film and the tantalum. The 500A thickness of titanium is a minimum for good adhesion. However, tantalum is very easy to crack and film surface is very rough when the film is thicker than 1.5 μm.

Tungsten can be directly deposited on the LTO surface when the film thickness is less than 6000A at room temperature. The adhesion between W and LTO is also depends on the sputter deposition power and pressure. High sputtering power and/or low deposition pressure will cause poor adhesion but good conductivity. A titanium adhesion

layer can be used to obtain good adhesion between W and LTO but the cracking of tungsten is still found when the tungsten film thickness is larger than 1.5 μm at room temperature sputtering due to the very strong stress of tungsten. Annealing is used to reduce the stress and increase conductivity. A 3μm thick tungsten was obtained through a two-step tungsten deposition process.

Copper could not be directly deposited on the LTO film. An aluminum or titanium adhesion layer is required. However Cu alloy may not be used for diamond deposition because the deposition temperature is too high and the Cu alloy converts to copper oxide.

A chromium or titanium adhesion layer is used to serve as an adhesion layer during gold or platinum deposition; chromium gives better adhesion than titanium.

CHARTER 6

RESULTS AND DISCUSSION

This chapter describes the results of the fabrication and testing for each of the major microprobes and prototype probe card discussed in Chapter 3. First, the general results of fabricated CHIPP probe cards are discussed, followed by device performance results of Al-SiO_2 and W-SiO_2 cantilevers.

6.1 General Results of Fabrication of the CHIPP Probe Card

Nine different types of prototype CHIPP probe cards were successfully fabricated, including four types of the Al-SiO_2 system, two types of the Al-Si system and three types of the W-SiO_2 system. Detailed parameters of the structures and materials used in the fabricated probe cards are shown in Table 6.1.

A SEM photo (Figure 6.1) shows a prototype probe card with a Al-SiO_2 bimorph structure mounted in a ceramic header. The cantilever probes are arranged around a opening of 1 cm^2 with a frame of 2mm wide.

SEM photos showing several adjacent microprobes after the cantilevers have been released through two steps of KOH and dry etch are shown in Figures 6.2-6.5. Figure 6.2 shows 50 x 500 μm microprobe cantilevers with Al-SiO_2 bimorph and gold tips. Figure 6.3 shows 40 x 400 μm microprobe cantilevers. Figure 6.4 shows 50 x 300 μm microprobe cantilevers. Figure 6.5 shows 30 x 200 μm microprobe cantilevers. Figure 6.6 shows an array of four adjacent 35 x 200 μm W-SiO_2 microprobes with conducting diamond tips.

The shapes of the released probe cantilevers are sharply delineated with smooth surface and smooth cantilevers edges as expected. The bending direction is just along the cantilever length; no bending is found along the direction of the cantilever width, even for the widest (60 μm) cantilever. The process for conducting diamond deposition also works well and is compatible a standard IC process through photolithography and plasma dry etch. Each CHIPP probe card unit is connected with the silicon substrate through very thin 200 μm bars which are broken to get a single device. At the four corners of the frame of CHIPP probe card unit (Figure 6.1), a round angle is observed due to corner over etching by KOH; an extra large compensation feature was designed to reduce this corner loss.

The general results show that the fabrication of the CHIPP microprobe is successful, and highly useful for the fabrication of real CHIPP probe cards.

Table 6.1 Structure parameters of fabricated CHIPP probe card.

Probe Type	Lower cantilever layer	Insulation layer	Heater	Top cantilever layer	probe tip
Al-SiO_2	0.6 µm Al at room temp.	0.2 µm SiO_2 at 425°C	0.25 µm $TaSi_2$ sputtering at 100 °C	0.6 µm SiO_2 at 425 °C	0.4 µm Ti/Pt at room temp.
Al-SiO_2	1.0 µm Al at 100 °C	0.3 µm SiO_2 at 425 °C	0.5 µm $TaSi_2$ sputtering at 100 °C	1.0 µm SiO_2 at 425 °C	0.4 µm Cr\Au at room temp.
Al-SiO_2	1.5µm Al at 100 °C	0.3 µm SiO_2 at 425 °C	0.5 µm $TaSi_2$ sputtering at 100 °C	1.2 µm SiO_2 at 425 °C	0.4 µm Cr\Au at room temp.
Al-SiO_2	3 µm Al at 100 °C	0.3 µm SiO_2 at 425 °C	0.5 µm $TaSi_2$ sputtering at 100 °C	1.2 µm SiO_2 at 425 °C	0.4 µm Cr\Au at room temp.
Al-Si	3 µm Al at 100 °C	0.3 µm SiO_2 at 425 °C	0.5 µm $TaSi_2$ sputtering at 100 °C	0.8 µm Si Sputtering at room temp.	0.4 µm Cr\Au at room temp.
Al-Si	0.6 µm Al at room temp.	0.3 µm Si_3N_4 at room temp.	0.4 µm $TaSi_2$ sputtering at room temp.	0.6 µm Si Sputtering at room temp.	0.4 µm Ti\Pt at room temp.
W-SiO_2	1 µm W Sputtering at room temp.	0.3 µm SiO_2 at 425 °C	0.5 µm W Sputtering at room temp.	1.2 µm SiO_2 at 425 °C	0.4 µm Cr\Au at room temp.
W-SiO_2	1 µm W Sputtering at room temp.	0.3 µm SiO_2 at 425 °C	0.5 µm W Sputtering at room temp.	1.2 µm SiO_2 at 425 °C	0.8 µm W at room temp.
W-SiO_2	1 µm W Sputtering at room temp.	0.3 µm SiO_2 at 425 °C	0.5 µm W Sputtering at room temp.	1.0 µm SiO_2 at 425 °C	1.5 µm diamond at 900-1000 °C

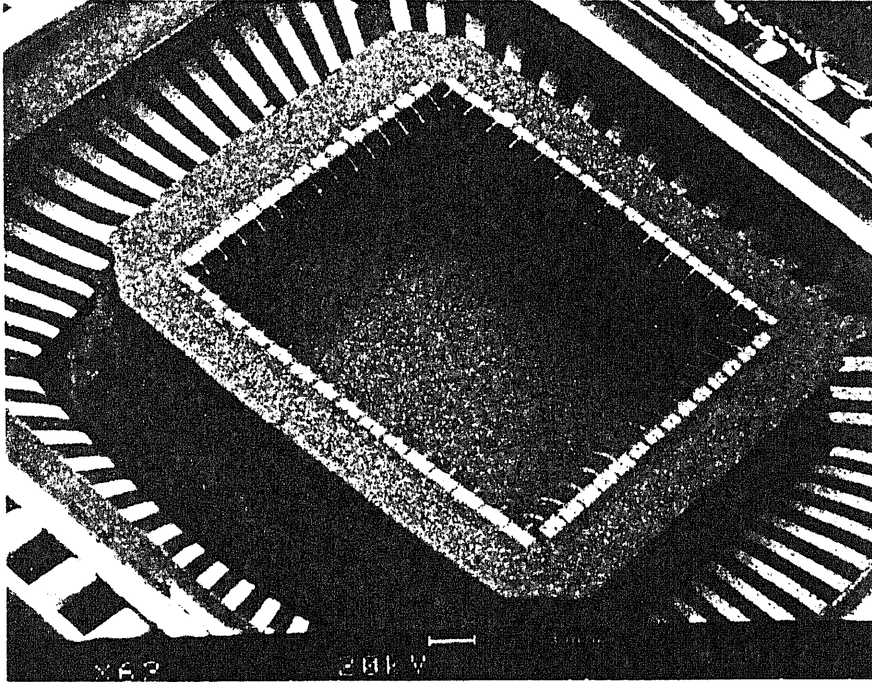

Figure 6.1 A prototype CHIPP probe card mounted in a ceramic header (6.2x).

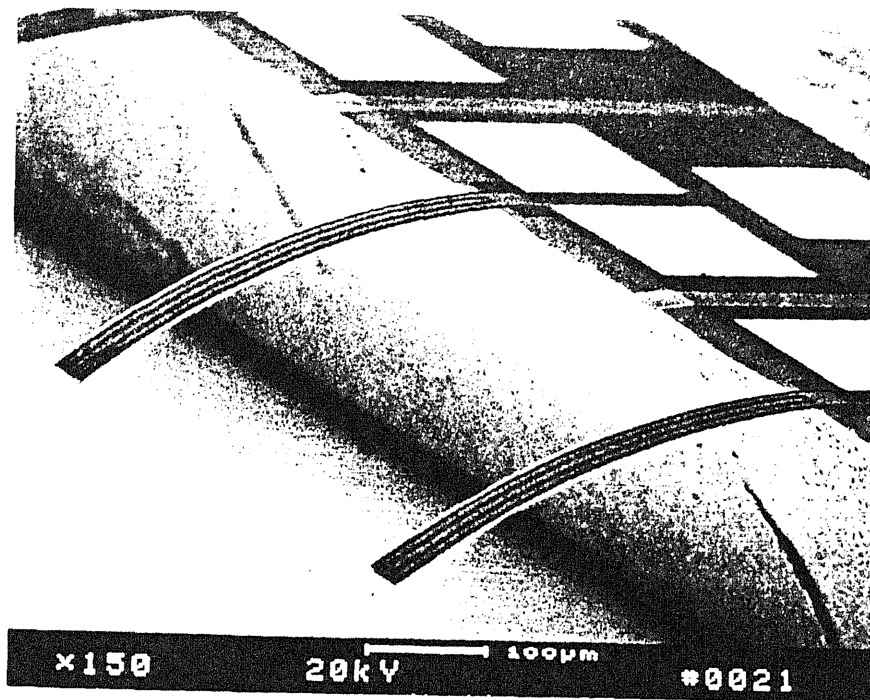

Figure 6.2 SEM photo showing two adjacent 50 x 500 µm microprobes with Al-SiO_2 bimorph structure. (150x)

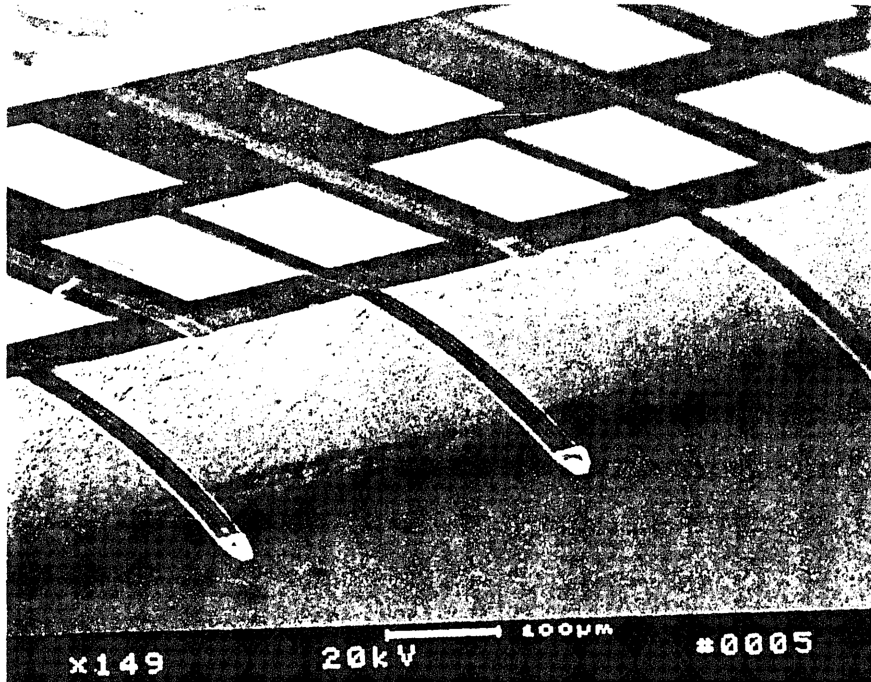

Figure 6.3 SEM photo showing three adjacent 40 x 400 µm microprobes with Al-SiO_2 bimorph structure and gold tips (149x).

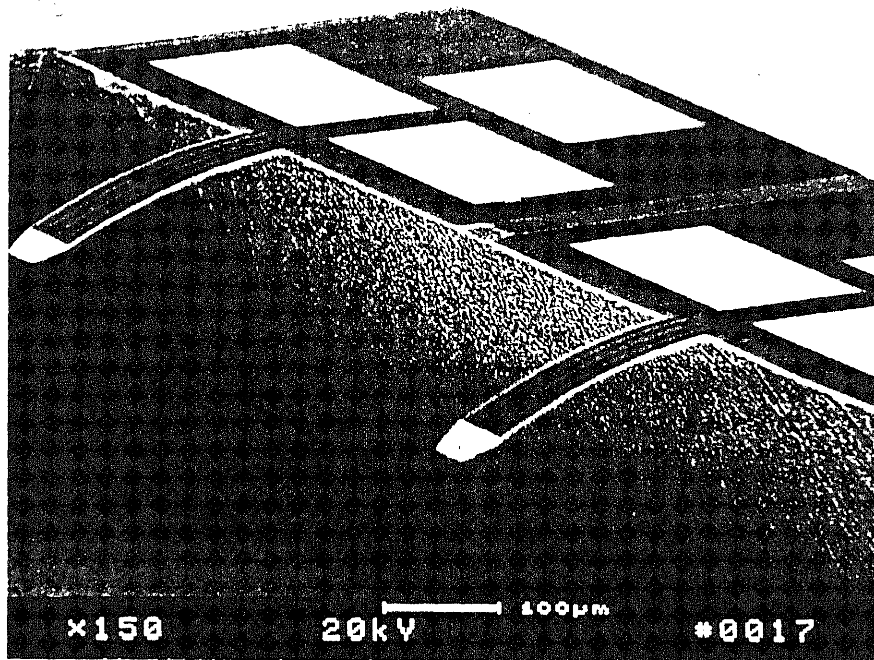

Figure 6.4 SEM photo showing two adjacent 50 x 300 µm microprobes with Al-SiO_2 bimorph structure and gold tips (150x).

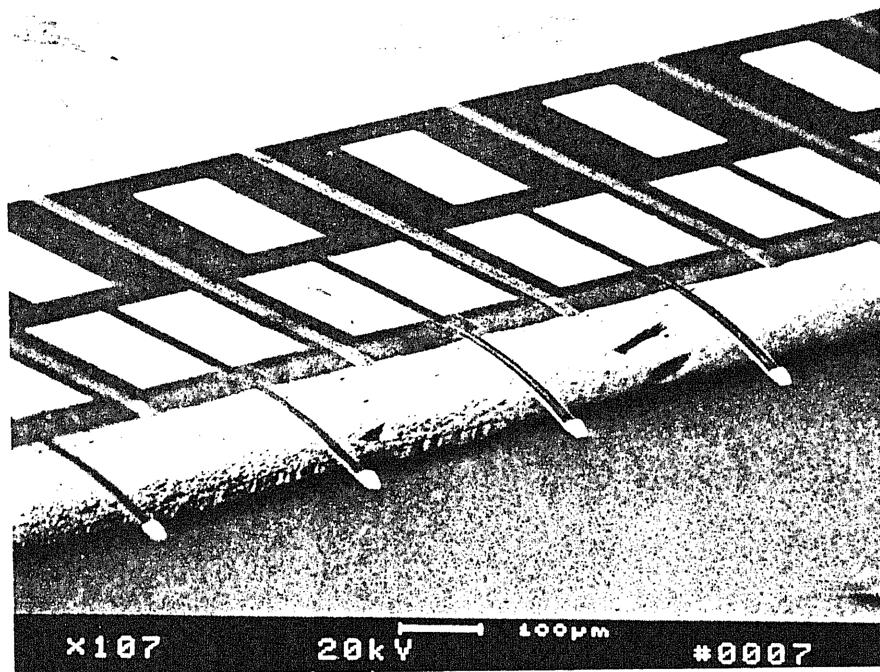

Figure 6.5 An array of four adjacent 30 x 200 μm microprobes with Al-SiO_2 bimorph structure and gold tips (100x).

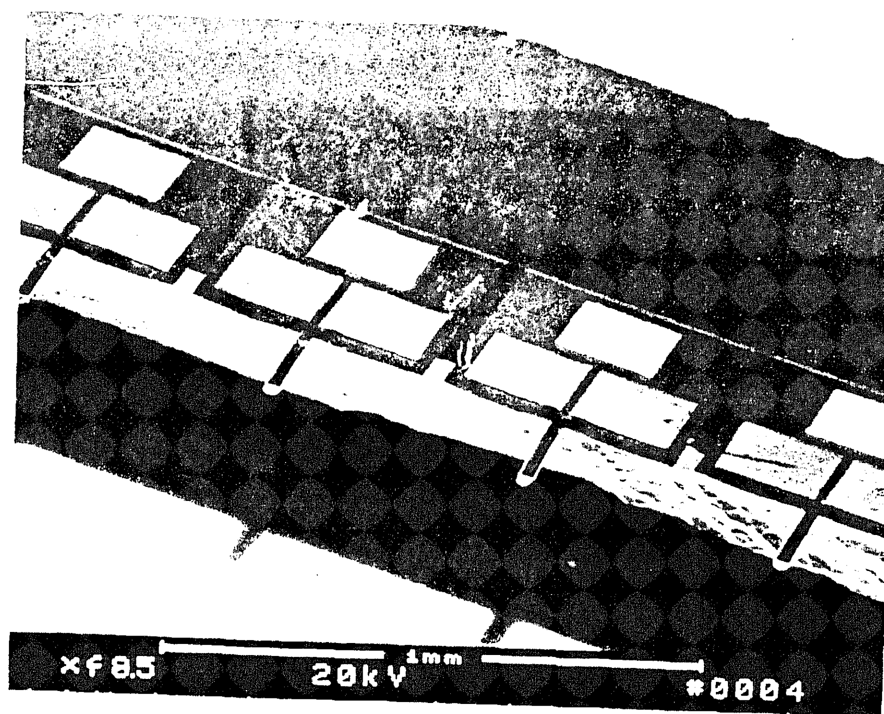

Figure 6.6 An array of four adjacent 30 x 200 μm microprobes with W-SiO_2 bimorph structure and conducting diamond tips (48.5x).

6.2 Switch Characteristics of the CHIPP Microprobes

Each microprobe can be considered to be a microswitch which is "on" when the probe tip is bent up to contact the test pad by increasing the input power, or "off" when the probe tip returns to its original position by decreasing the input power. Therefore the switch characteristics of the microprobes depend on the moving distance, response time and initial positions of the microprobe tips. If the initial position is below the probe card surface, then actuation must supply sufficient force to bring the tips through the surface plane to the other side.

6.2.1 Rest Positions of the Microprobe Tips

The unpowered rest states of the microprobe tips are a distance 20-280 μm below the nominal CHIPP wafer surface due to built in stress during the fabrication. The rest positions of the microprobe tips were found to depend on the cantilever length, width, thickness, materials, deposition temperature, and heat treatment.

Table 6.2 listed four types of the CHIPP probe cards with different cantilever lengths, thicknesses, widths, deposition temperature, and materials. The (-) sign represents the probe tips below the probe card surface. Figure 6.7 shows the rest positions of cantilever tips as a function of cantilever length with three different Al thicknesses for Al-SiO_2 and Al-Si cantilevers. Because four cantilevers with the same width but different lengths were designed in each probe card unit, these probe cantilevers can be used to measure the cantilever rest position as a function of its thickness. Figure 6.8 shows the rest position of cantilever tips as a function of cantilever thickness with the

same deposition temperature, materials, and cantilever sizes. The stress causing the cantilever bending at rest is caused by the internal total stress as discussed in Chapter 3.

From Figure 6.7 the rest positions of the cantilever tips are found to be linearly proportional to the cantilever length for four different bimorph cantilevers. Additionally, the rest position of the probe tips are inversely proportional to microprobe cantilever thickness (Figure 6.8). The cantilever width also affects the rest position of probe tips (Table 6.2), with wide cantilevers have a smaller rest deflection compared with narrow ones. The rest deflection is also a function of deposition temperature (from Table 6.2) and high deposition temperature causes a larger rest deflection (as expected from equation 3.2). However even with sputter depositions done at room temperature, an initial deflection is still found due to intrinsic stress (see Table 6.2).

Table 6.2 Rest positions of the tips for different microprobes.

Cantilever sizes and types (μm)	Heater position	Rest tip position of Al (0.6μm)-SiO_2 (0.6μm) (μm)	Rest tip position of Al(1μm)-SiO_2(1μm) (μm)	Rest tip position of Al(3μm)-SiO_2(1.2 μm) (μm)	Rest tip position of Al(3μm)-Si (0.8 μm) (μm)	Rest tip position of Al (0.6μm)-SiO_2 (0.6μm) (μm)*
30 x 200	inside	-65	-46	-26	-23	-21
35 x 200	inside	-75	-53	-23	-20	-18
40 x 260	outside	-98	-81	-38	-33	-23
50 x 300	inside	-123	-84	-45	-39	-28
40 x 300	inside	-133	-91	-55	-45	-35
40 x 300	outside	-135	-105	-42	-42	-37
40 x 400	inside	-235	-148	-79	-69	-40
50 x 400	inside	-209	-143	-64	-60	-38
40 x 400	outside	-230	-174	-70	-58	-45
60 x 500	inside	-264	-141	-123	-105	-83
50 x 500	inside	-283	-195	-135	-112	-91
40 x 500	outside	-289	-262	-102	-84	-94

* All processes are done at room temperature.

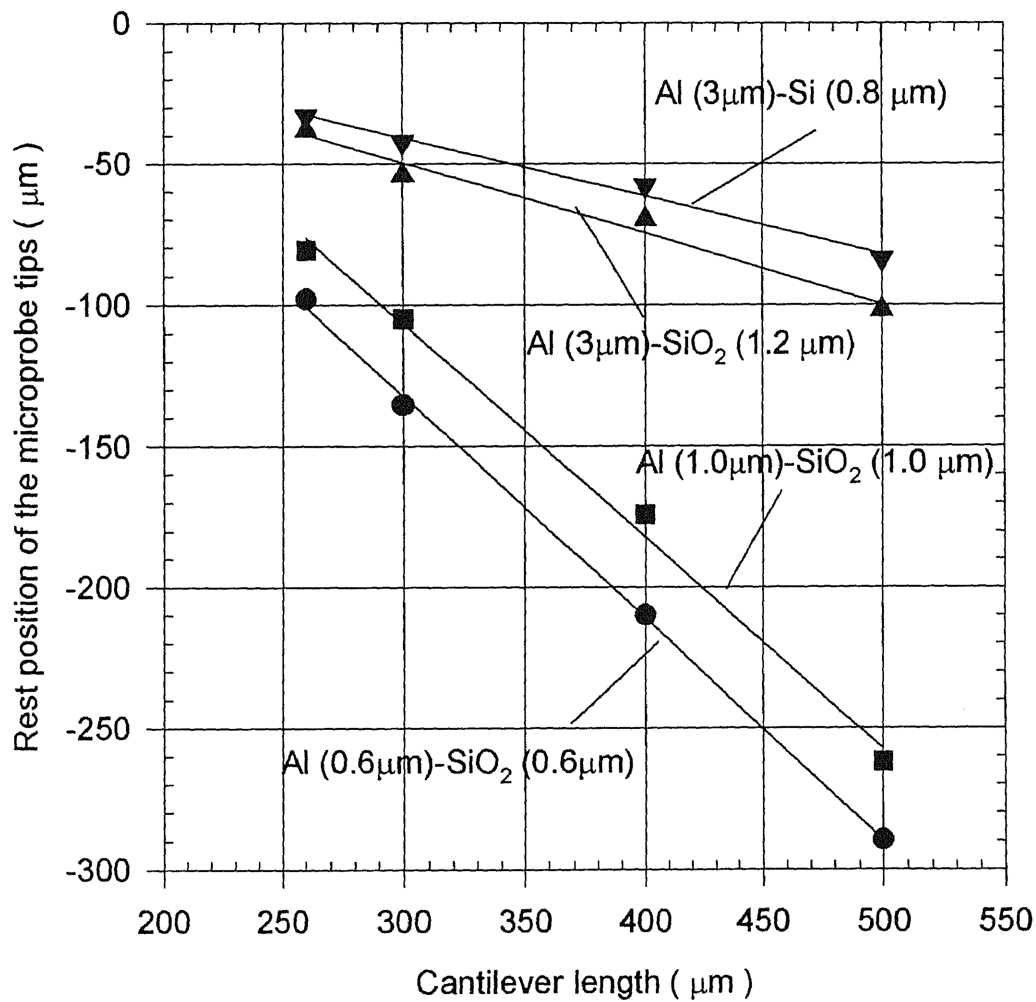

Figure 6.7 Cantilever tip rest position as a function of cantilever length with four different cantilever structures. Zero is the probe card surface.

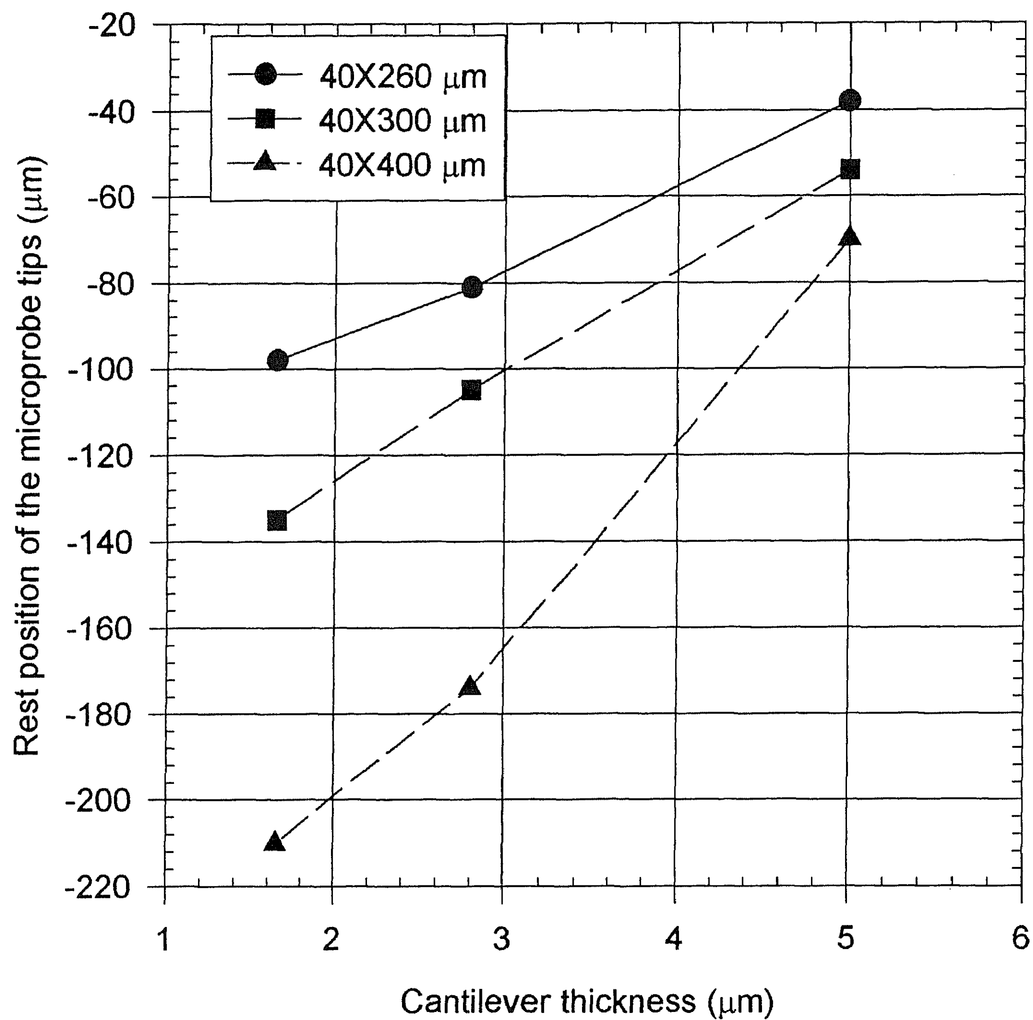

Figure 6.8 The rest position of microprobe tips as a function of the cantilever thickness with three different cantilever sizes. Zero is the probe card surface.

6.2.2 Deflection of the Microprobe

In order to contact the test pads, actuation must supply sufficient force to bring the tip through the surface plane to the other side to contact the test pad surface. Tip deflection has been measured as a function of applied power. The results are plotted in Figure 6.9 for five different Al-SiO_2 bimorph structures and show that the deflection efficiency ($d\delta/dP$) varies over the range 5.23 to 9.6 μm/mW. These results show that a deflection of over 250 μm can be achieved with power levels ranging from 28-53 mW. Figures 6.11 to 6.12 are the SEM photos showing the side view of Al-SiO_2 cantilevers (60 x 500 μm and 40 x 400 μm and t_{Al} =1.5 μm) unpowered, and thermally actuated.

Compared with Al-SiO_2 the deflection range for the W-SiO_2 bimorph structures is smaller (see Figure 6.10) with the deflection efficiency ($d\delta/dP$) varying over the range 2.4 to 2.8 μm/mW. A deflection of 100-150 μm can be reached with power levels ranging from 40-62 mW. The deflection efficiency of W-SiO_2 are about 2-3 times smaller due to a lower coefficient of thermal expansion of tungsten compared with Al.

This results are compared with other published data presented in Table 6.3. A Si-Au cantilever with length of 500 μm, width of 80-100 μm and thickness of 5.8 or 6.5 μm was obtained the deflection efficiency of 0.37-0.57 μm/mW [15] and low deflection range, possibly because the cantilevers were wide and thick. Additionally, the gold metal has a smaller coefficient of thermal expansion than Al. The ratio of the two layer thickness and cantilever structure and materials may be also be far from ideal. Reference [16] reported that a large input energy of 1W was needed to produce a deflection of 108 μm with a

large cantilever (size 1000 x 1000 μm), and deflection efficiency was 0.108 μm/mW. It is clear that the large size of the cantilever consumes a large thermal energy.

Table 6.3 Data of thermal driven cantilevers.

Cantilever size (μm)	Deflection efficiency (μm/mW)	Deflection range (μm)	Reference
Si-Au cantilever with L=500, W_{Si}=100, W_{Au}=80, t_{Au}=1.8 and t_{Si}=4	0.37	0 - 70	[15]
Si-Au cantilever with L=500, W_{Si}=100, W_{Au}=80, t_{Au}=2.5 and t_{Si}=4	0.57	0 - 100	[15]
Si-Al cantilever with L=1000, W=1000, t=25	0.108	0 - 108	[16]
Al-SiO_2 cantilever W=60, L=500, t_{Al}=1, t_{SiO2}=1, and t_{total}=2.8	5.23	0 - 277	this research

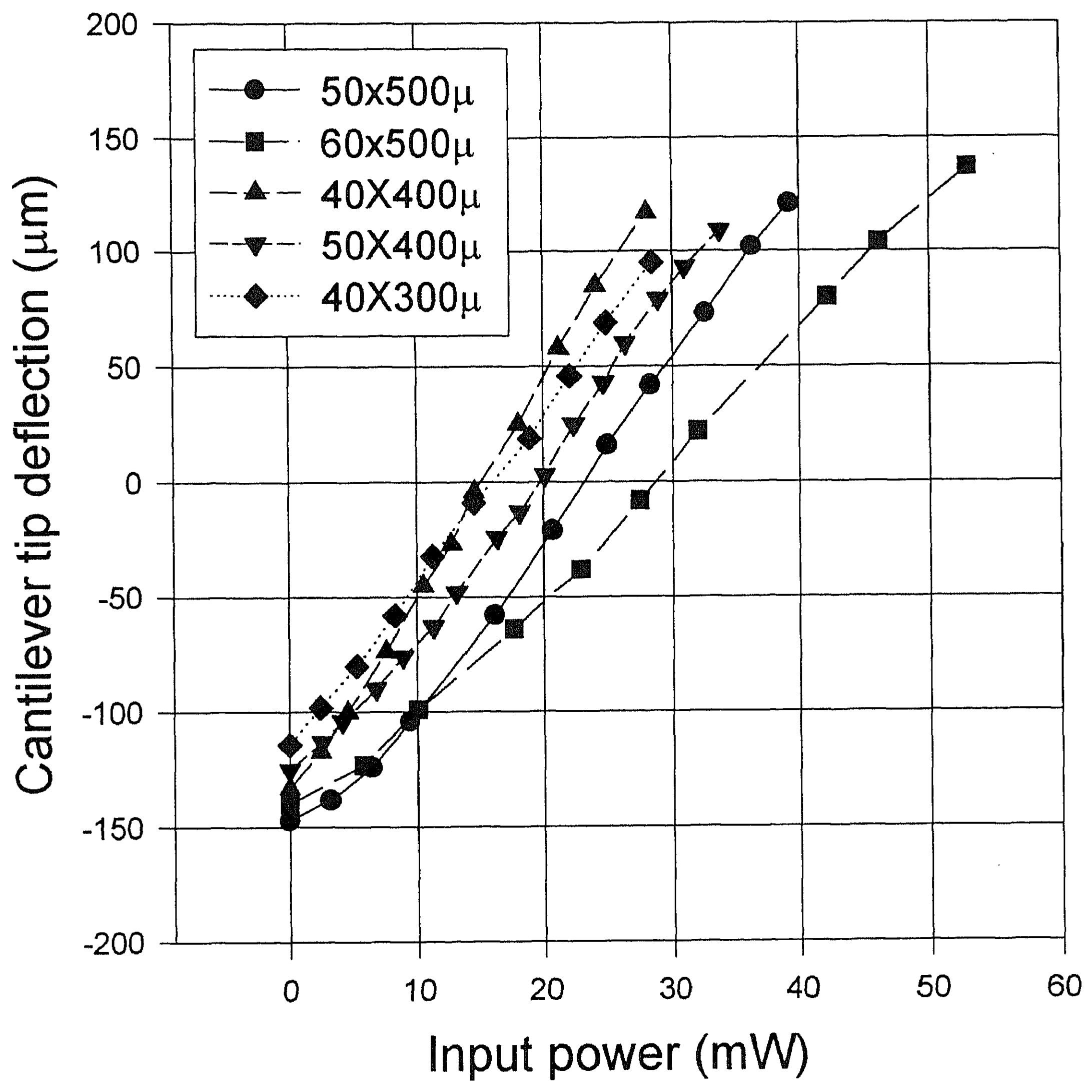

Figure 6.9 Tip deflection vs. applied power with Al (1.0 μm)-SiO_2 (1.0 μm) bimorph cantilevers. Inset shows cantilever widths and lengths for five devices.

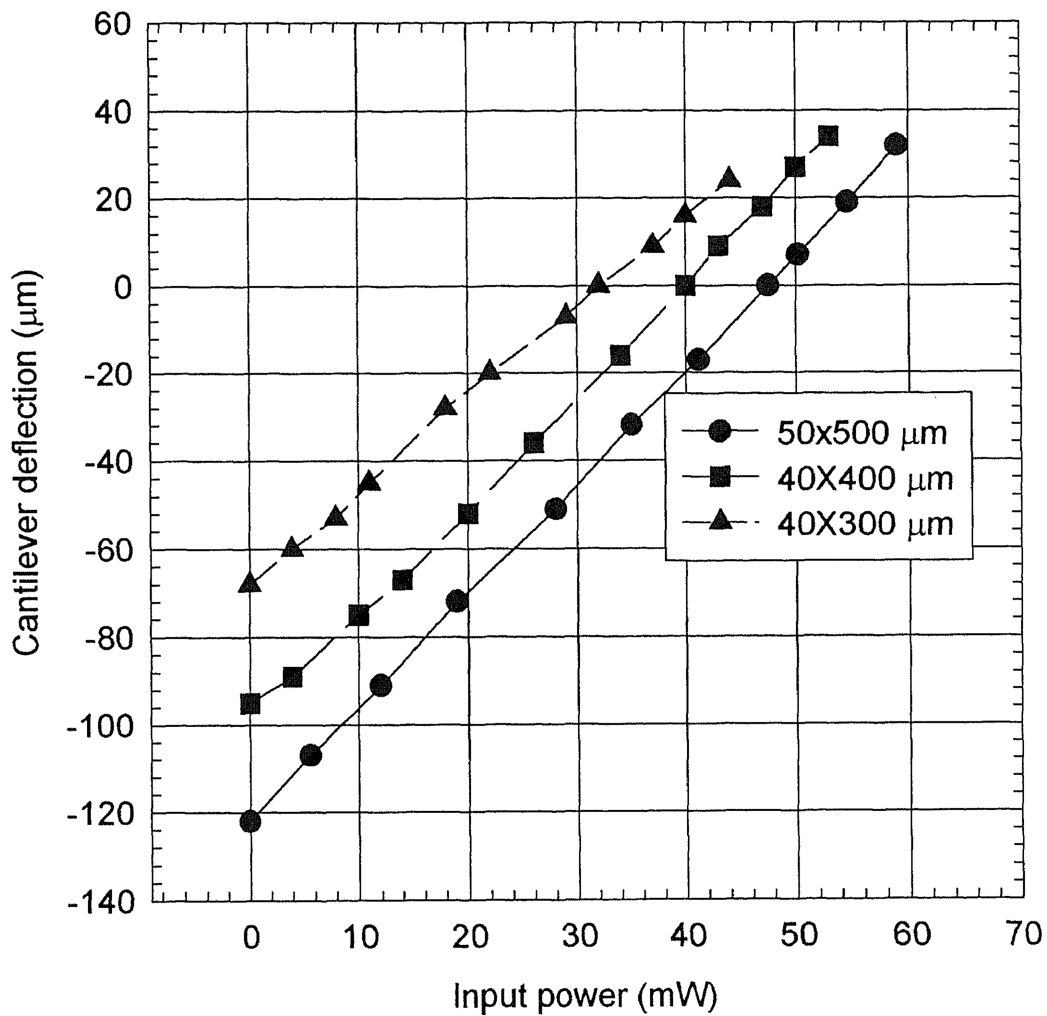

Figure 6.10 Tip deflection vs. applied power with W (1.0 μm)-SiO_2 (1.2 μm) bimorph structures. Inset shows cantilever widths and lengths for three devices.

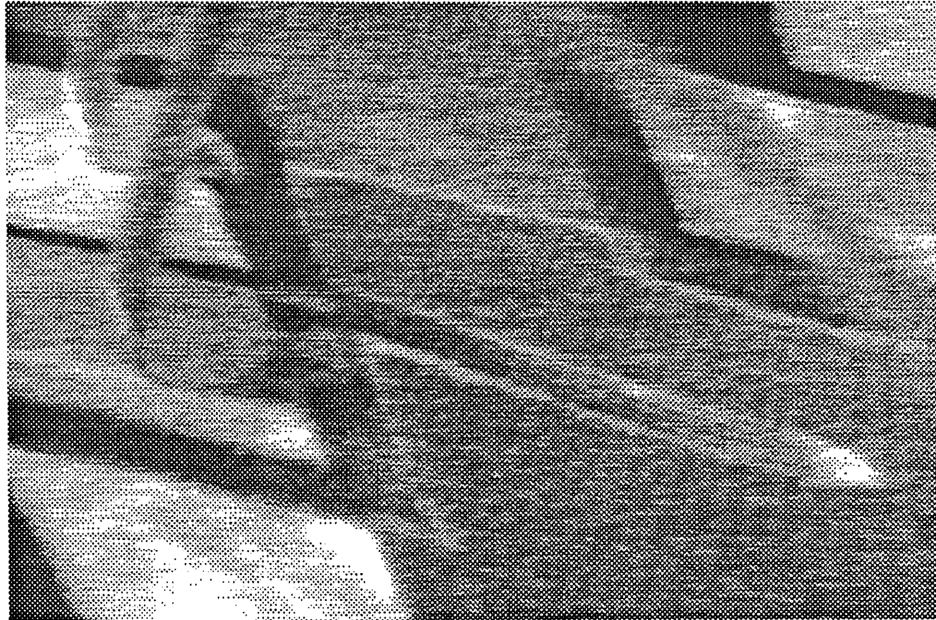

(a) the cantilever at a flat position

(b) The cantilever at a rest state over 100 μm below probe card surface

Figure 6.11 SEM side view of a 60 x 500 μm Al-SiO_2 cantilever at unpowered rest state (b) and actuated to a flat position (a). Photos were taken from a video tape during dynamic testing.

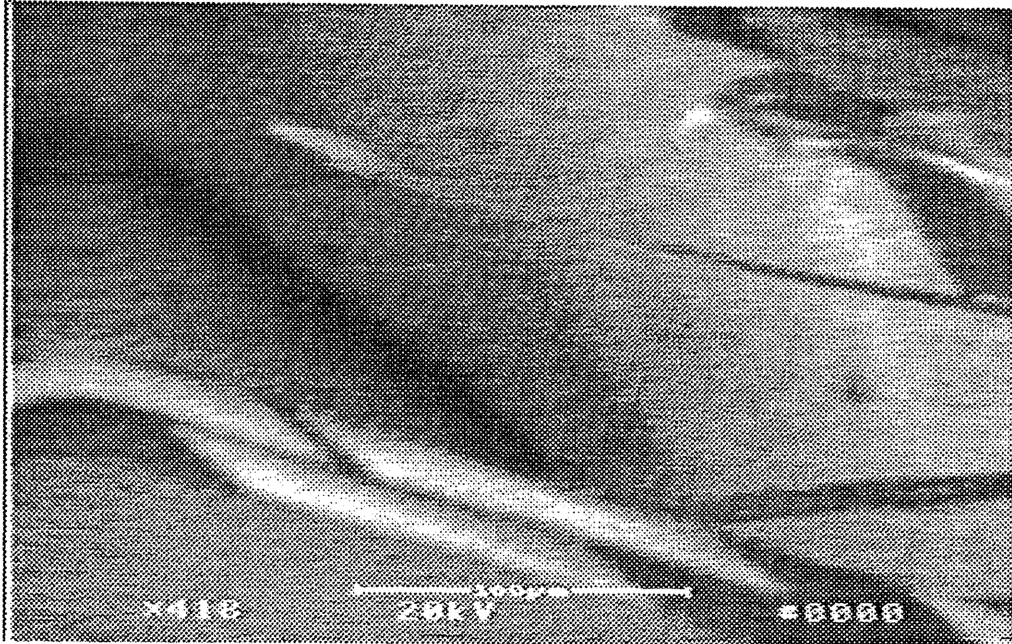

(a) CHIPP microprobe actuated upwards.

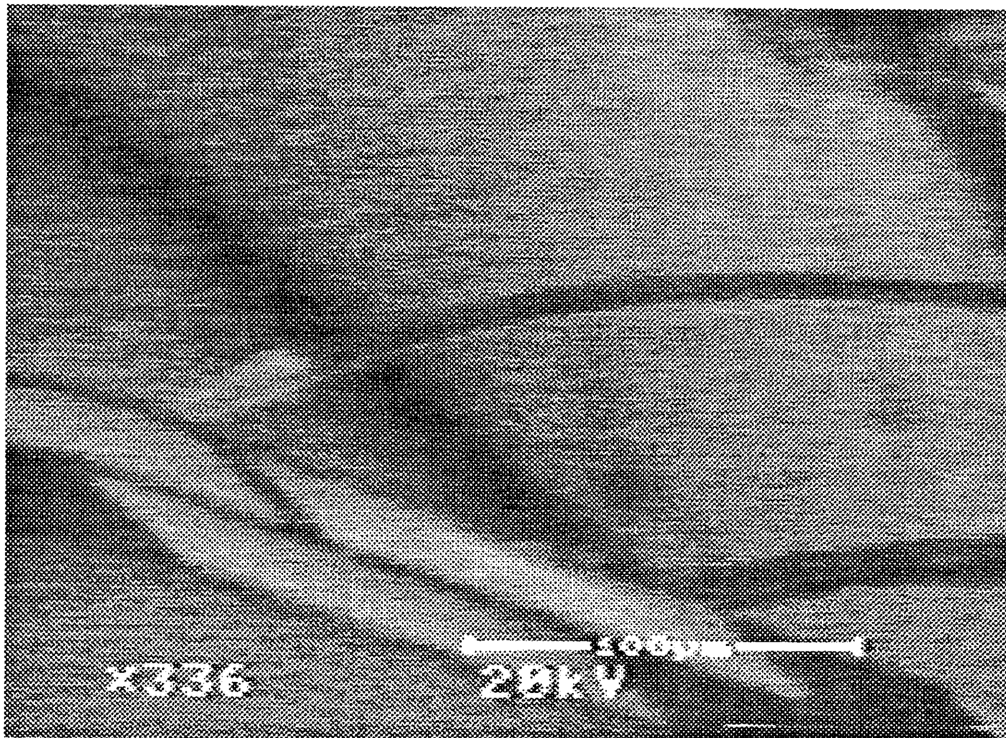

(b) CHIPP microprobe at unpowered rest position

Figure 6.12 SEM side view of a 40 x 400 µm Al-SiO_2 cantilever at unpowered rest state (b) and actuated to a upward position (a). Photos were taken from a video tape during dynamic testing

6.2.3 Response Frequency and Time of the Microprobe

The dynamic behavior of the cantilever has been tested with square-wave, sine-wave and ramp-wave input signals, which were made with a series connection to a d.c. input power supply. The devices were bonded to a silicon heater, wire bonds were attached, then the devices were put into an SEM chamber for the dynamic measurements. The electrical connection are made through a special flange with electrical feed-through. The cantilever motion was recorded through a VCR and measured later at slow motion. The deflection with high freqency was measured with SEM pictures compared with the ruler on the picture. All the data reported here were taken with a square-wave input signal; the sine-wave and ramp-wave signals were used to obtain "slow motion" video images.

A 60 x 500 μm Al-SiO_2 cantilever with t_{Al}=1.0 μm and t_{oxide} =1.0 μm and 40 x 300 μm was completely tested at an electrical input peak power of ~42 mW with a square wave input signal. Results are shown in Figures 6.13 and 6.14. From examination of the video tape it is seen that at fixed value of the maximum power, a dynamic deflection of ~134 μm is occurs up to frequencies of approximately 120 hertz, then decreases with frequency increase. The first cantilever resonant frequency was found at 6.48KHz with maximum deflection about 90 μm and the next frequency was found at 19.4KHz with maximum deflection over 210 μm. The dynamic defection distance is the distance the tip moves its minimum position to its maximum position. The dynamic deflection as a function of input signal frequency is shown in Figure 6.13, and deflection as a function of time with a fixed frequency of 1 Hz was measured and shown in Figure 6.14. From the know raster frequency both the rise and fall time were found to be less than 33ms. The cantilever resonant frequency has been calculated by using the following formula[47]:

$$f_{min} = 0.1604\sqrt{\frac{E(1-\sigma^2)}{\rho}} \cdot (\frac{t}{L^2}) \qquad (6.1)$$

Where E is Youngs' modulus, ρ is mass density and σ is Poisson's ratio of the beam meterial, t is thickness and L is length of the cantilever, respectively. For t = 2.8 μm and L = 500 μm, ρ = 2.5 g/cm^3, σ = 0.25 and E = 0.78 x 10^{11}N/m^2, f_{min} = 9.7 KHz.

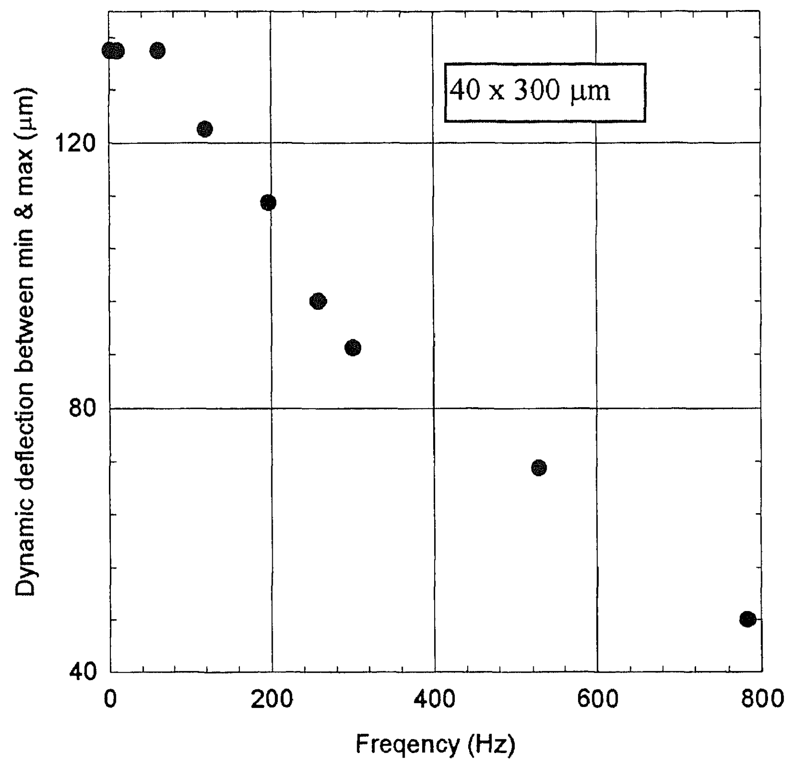

Figure 6.13 (a) Dynamic deflection of a Al-SiO_2 cantilever as a function of input signal frequency with square wave input for .

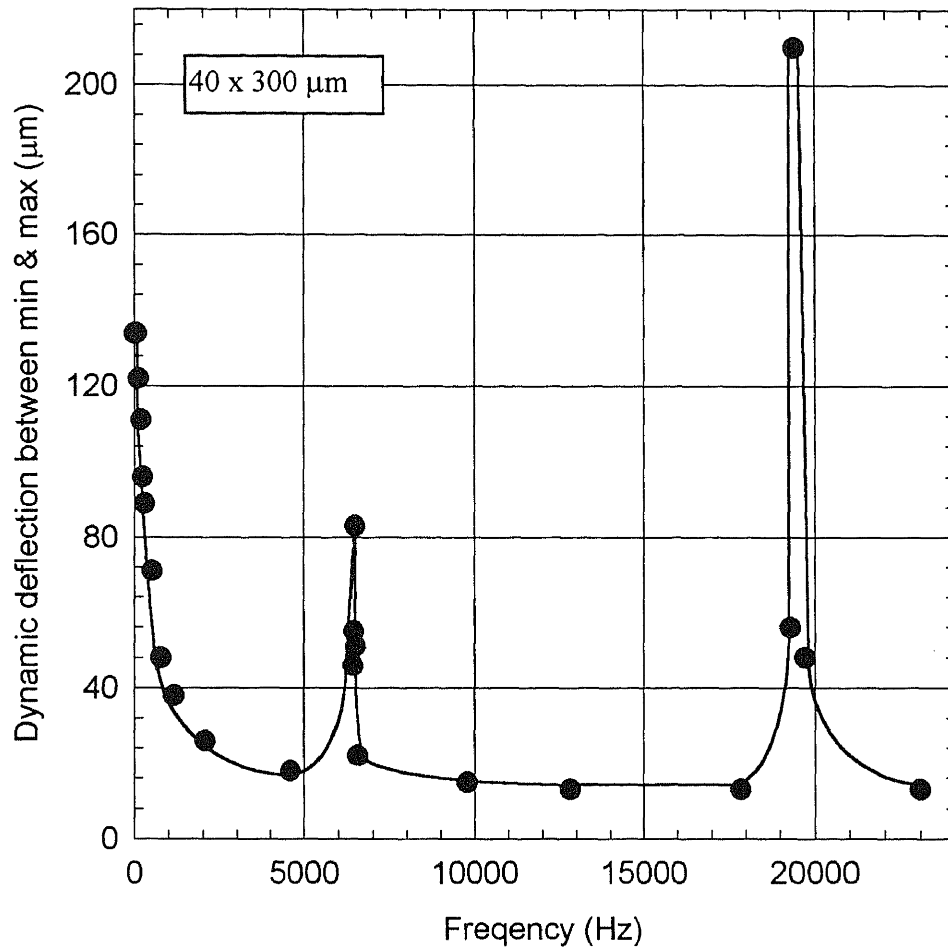

Figure 6.13 (b) Dynamic deflection of a Al-SiO_2 cantilever as a function of input signal frequency with square wave input.

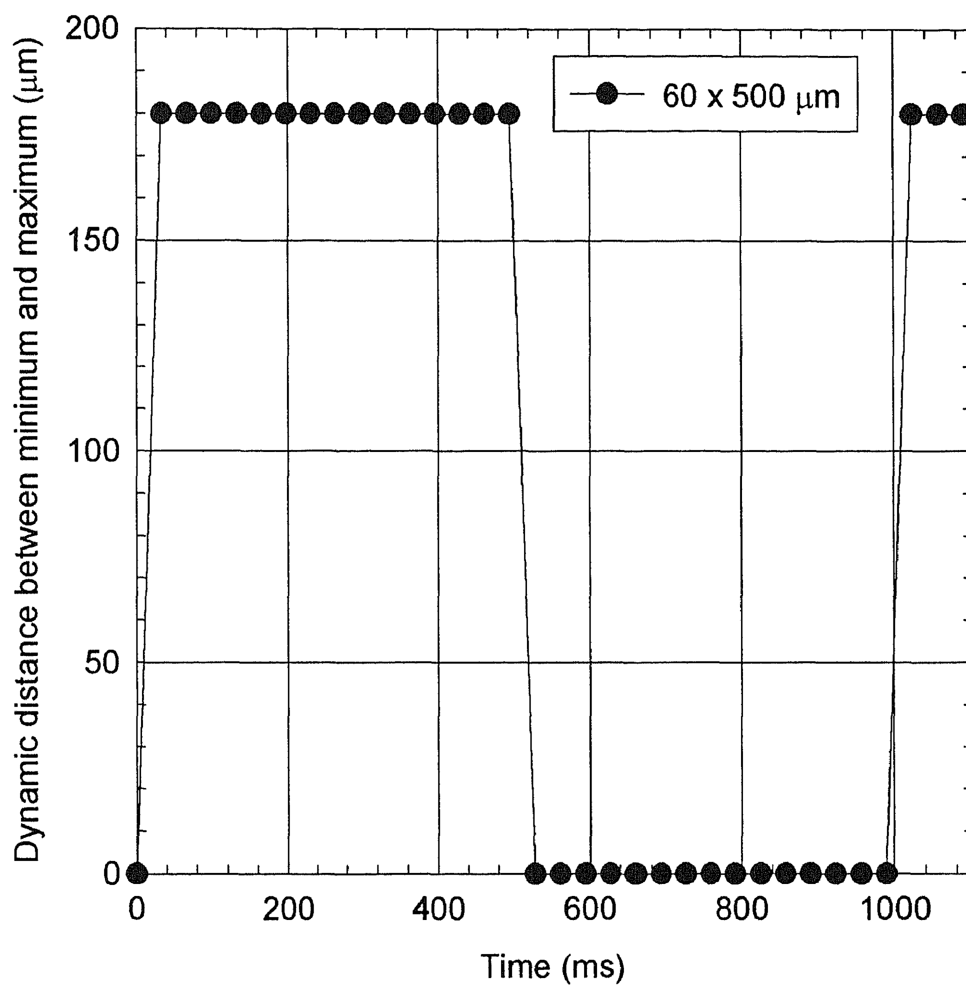

Figure 6.14 Dynamic deflection of a Al-SiO_2 cantilever as a function of input signal time with fixed square wave input of 1 Hz. This is the same cantilever described in Figure 6.13.

6.3 Ohmic Contact of CHIPP Microprobe

6.3.1 Ohmic Contact

Ohmic contact resistance has been measured using three different tips: gold, conducting diamond, and tungsten. Figure 6.15 shows a gold contact tip on a Al-SiO_2 cantilever with a 0.5 μm gold film deposited on aluminum. A 1.0 - 1.5 μm of conducting diamond was grown on the tip of the W-SiO_2 cantilever as shown in Figure 6.16. 1-3 μm crystals of conducting diamond (Figure 6.17) are ideal for scrub action to enable ohmic contact.

Contact resistance between a CHIPP probe tip and a test probe pad was measured through directly contacting them together in air. Results are shown in Table 6.4. Most contact resistances were less than 1 Ω.

Table 6.4 Measured contact resistance of CHIPP microprobes.

Cantilever structures	Contact type	Contact resistance R_c (Ω)
Gold tip Al-SiO_2 Cantilever	Gold - Gold	0.8 - 1
Gold tip W-SiO_2 Cantilever	Gold - Gold	0.25 - 0.5
Tungsten tip W-SiO_2 Cantilever	Tungsten - Tungsten	0.25-0.6

The tips of conducting diamond on W-SiO_2 cantilevers were also tested and gave a contact resistance of ~100 Ω, this may be because the conducting diamond is insufficiently doped. Highly doped conducting diamond on a tungsten tip has been reported with 0.25 Ω contact resistance [42].

In order to observe action between a probe tip and the test pad, some contact experiments were set up inside the SEM chamber. A gold probe tip with Al-SiO_2 cantilever was to contact a tungsten test pad. Two micromanipulators inside the SEM were used to independently move the CHIPP microprobe tip and the tungsten test pad. The test pad was moved to the position ~ 20-50 μm above the CHIPP probe tip. During the testing the CHIPP probe was first actuated upwards to contact the test pad, then ohmic contact was made by further increase in input power. Action was observed in the SEM TV mode and recorded a video tape. Figure 6.18 shows a SEM photo of a side view of an Al-SiO_2 cantilever probe unpowered, at rest, with the tungsten electrode (bright) above the tip. Figure 6.9 is a SEM photo showing same cantilever, fully deflected and making ohmic contact with the tungsten electrode (electrode is dark due to 'voltage contrast").

A slight scrub action was observed at 1200x magnification (unrecorded) and ohmic contact was made at the same time. A contact resistance of 1-3 Ω was measured between the gold tip and the tungsten probe pad. Tip bending was also observed; the narrow tip with w_1=50 μm h=50 μm, and w_2 = 20 μm was considerably bent, and the wide tip with w_1=60 μm h=30 μm, and w_2 = 44 μm gave less deformation and is probably the better choice.

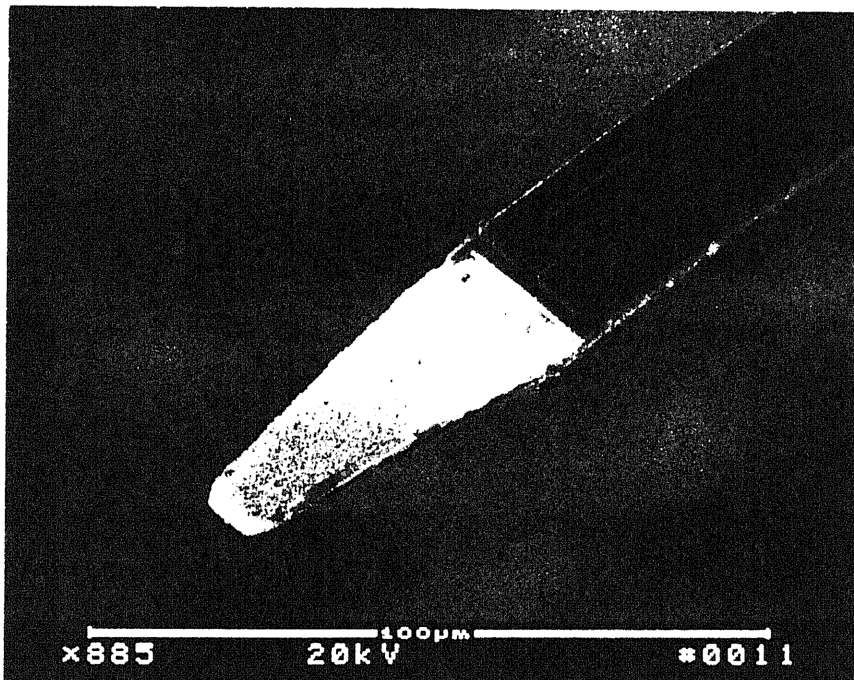

Figure 6.15 A gold contact tip on a Al-SiO_2 cantilever with 0.5 µm gold film.

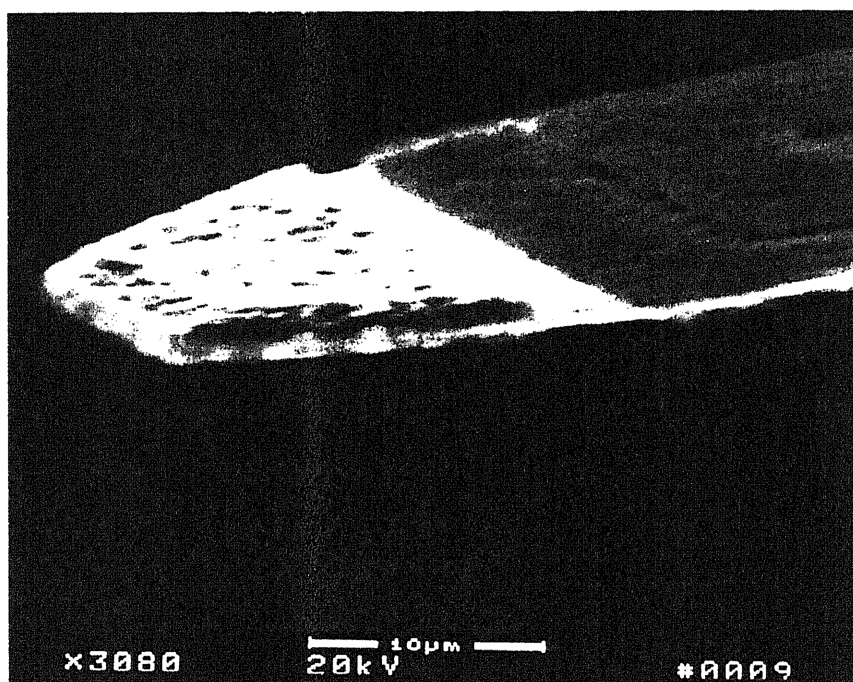

Figure 6.16 A conducting diamond tip on a $W\text{-}SiO_2$ cantilever.

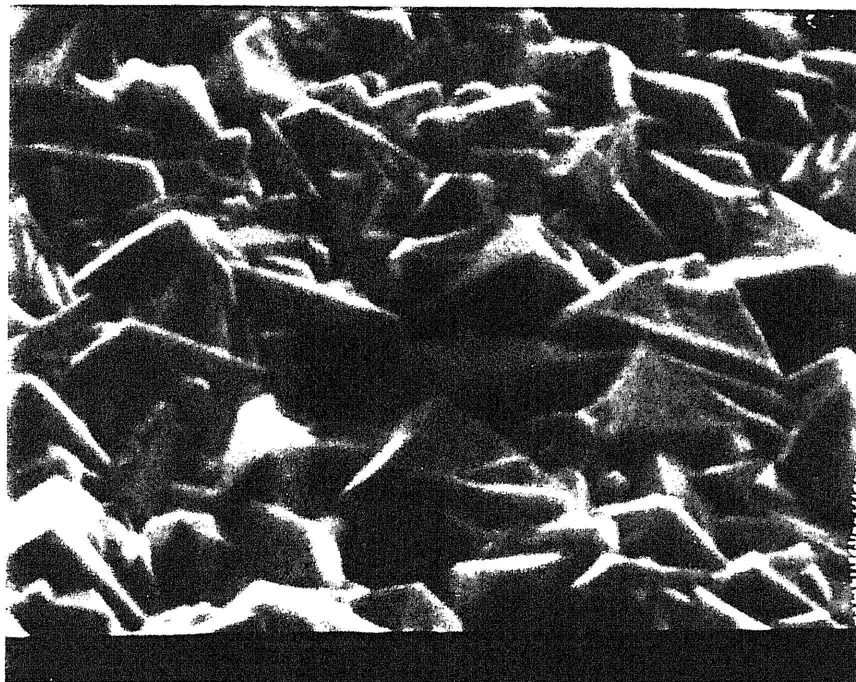

Figure 6.17 SEM photo showing crystals of conducting diamond (5000x).

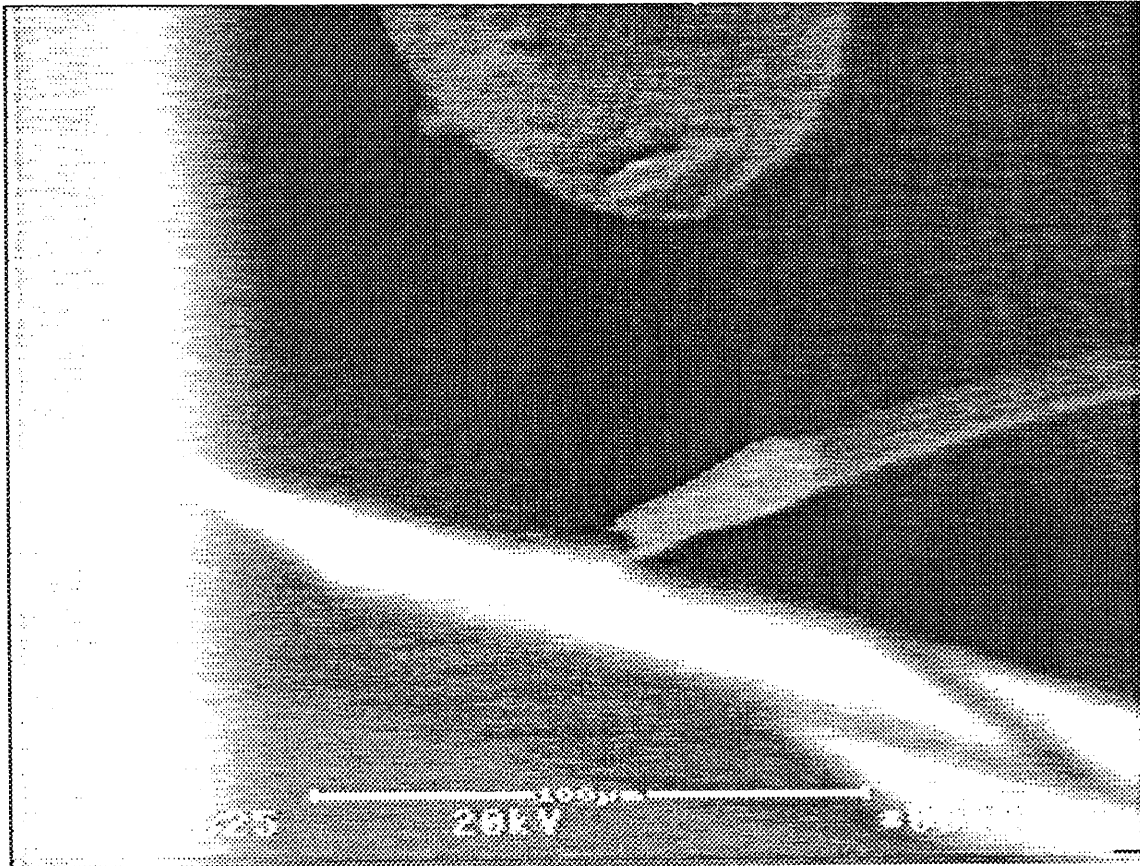

Figure 6.18 A SEM photo showing a side view of an Al-SiO_2 cantilever probe unpowered, at rest, with the tungsten electrode (bright) above the tip.

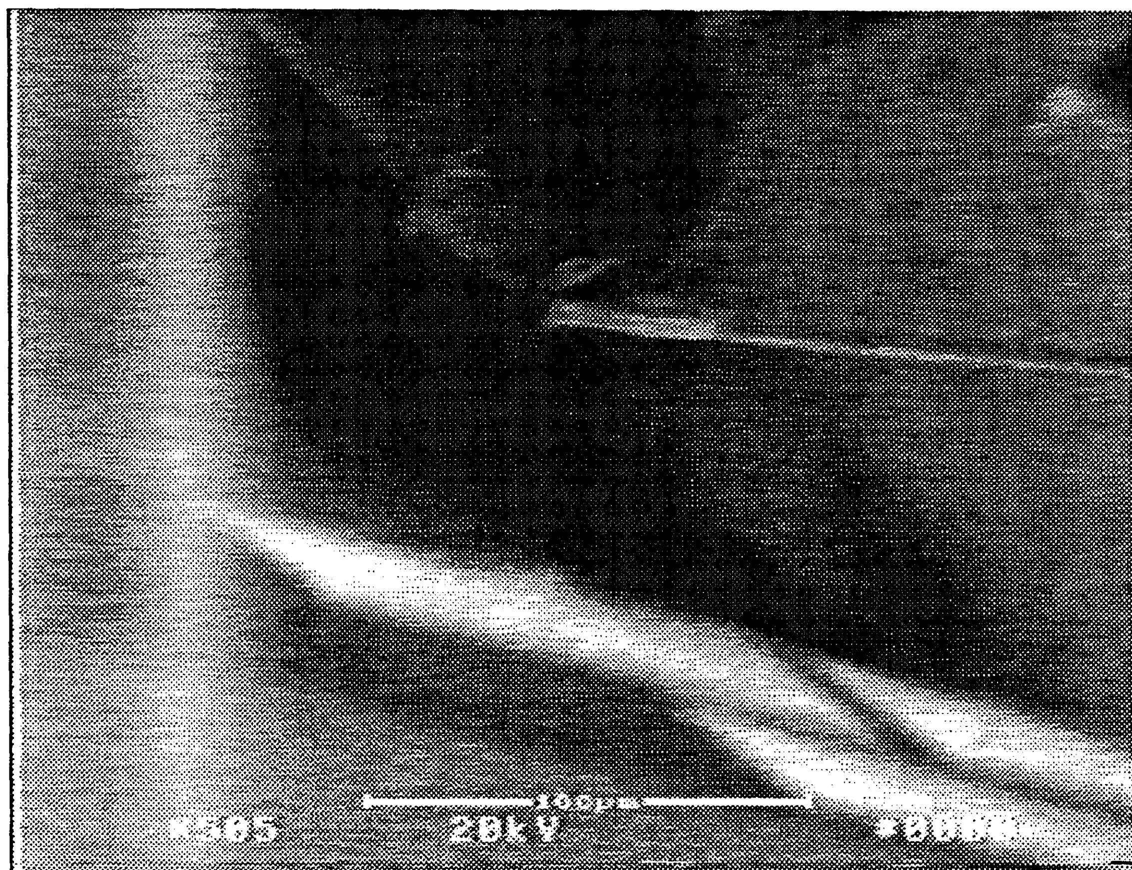

Figure 6.19 A SEM photo showing same cantilever as Figure 6.19, fully deflected and making ohmic contact with tungsten electrode (electrode is dark due to "voltage contrast").

6.3.2 Contact Force

Contact force can be calculated form the cantilever deflection. Figure 6.20 shows the calculated tip force as a function of tip motion. The calculated curves of Figure 6.20 are combined with the experimental data shown in Figure 6.9 to generate curves showing the amount of the force generated by applied heater power levels in a range up to 53 mW. Results are shown in Figure 6.21 and show that forces greater than of 100 μN can be obtained with structures made in this research.

From the data in Figure 6.21 the efficiency of the conversion of power to force α_p is calculated for the equation

$$F = \alpha_p P \tag{6.2}$$

The parameter α_p is shown in Table 6.5 for various values of W and L. The force efficiency varies over the range 1.4 to 5.5 μN/mW. The efficiency increases with decreasing width and length in part because greater cantilever surface area requires greater power input to achieve a given temperature. The forces calculated in reference [18] for 100 x 500 μm Au-Si cantilevers are 1.2 and 2.66 μN/mW for the thickness 5.8 and 6.5 μm, respectively. These results are similar to ours.

During ohmic test an additional power of 15-20 mW was required in order to make ohmic contact using a 50 x 400 cantilever; this is equivalent to an applied force of 45-60 μN. This results is within the range of published data (see discuss in section 3.3.1) where a contact force of less than 1 μN was needed for a gold-gold contact between AFM probe tip and a gold metal film [41], and a contact force of 100 μN was needed between two larger gold contacts [40].

Table 6.5 Force efficiency α_p for various values of W and L for bimorph with 1 μm Al and 1 μm SiO_2.

W (μm)	L (μm)	α_p (μN/mW)
50	500	1.4
60	500	1.2
40	400	2.7
50	400	3.0
40	300	5.5

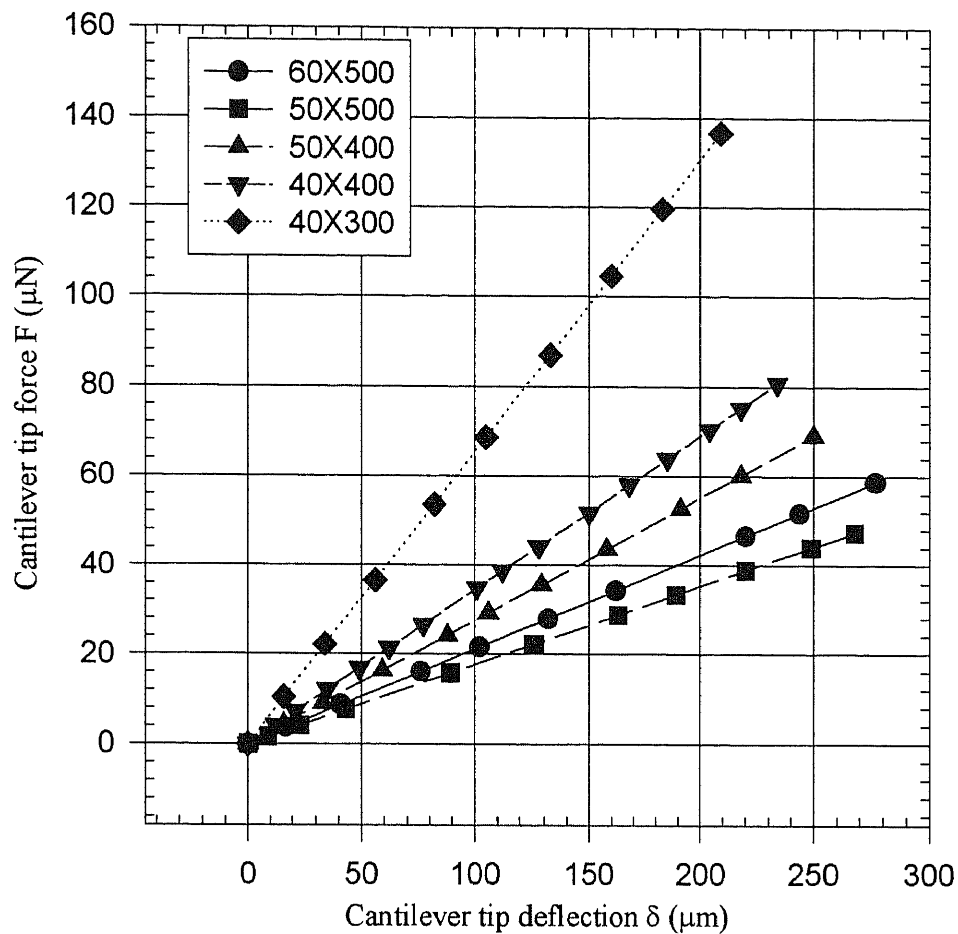

Figure 6.20 Force as a function of tip motion for various combination of aluminum and SiO_2 cantilever widths and lengths.

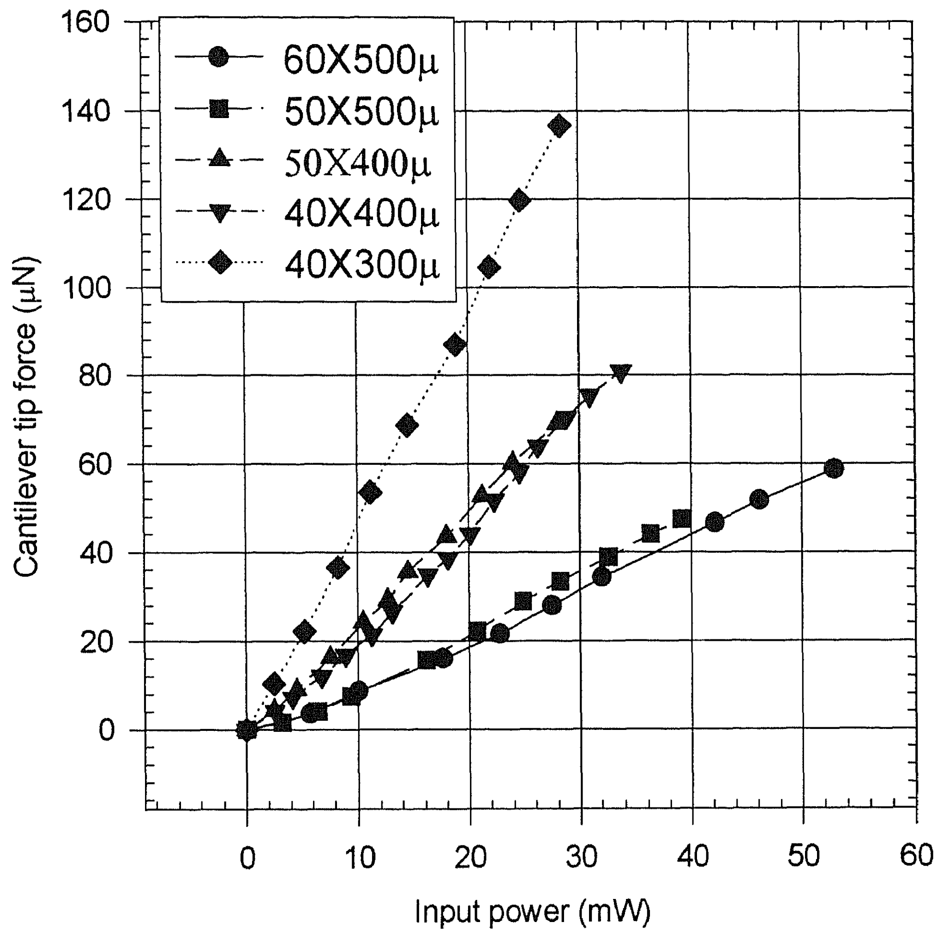

Figure 6.21 Force as a function of applied power for various combination of aluminum and SiO_2 cantilever widths and lengths.

6.4 Heat loss of CHIPP Microprobe

The deflection efficiency is used to measure the difference in heat loss for air and vacuum operation with a 60 x 500 μm Al-SiO_2 cantilever and t_{Al} =1.5 μm; the heater was sandwiched inside the cantilever; this structure is shown in Figure 6.22. The cantilever deflection was measured as a function of input power separately in 10^{-6} torr vacuum and at 1 atmosphere. The results are plotted in Figure 6.23 for both conditions and show the deflection efficiency is 6.17 μm/mW in vacuum and 3.13 μm/mW at 1 atmosphere. The heat loss ratio (ratio of deflection efficiencies in vacuum and at 1 atmosphere) is about 2. This result shows that heat loss to air during the cantilever heating is substantially high even with heater inside the cantilever structure.

Another Al-SiO_2 cantilever with the heater on the bottom of the cantilever (see Figure 6.24) in the same CHIPP probe array was also used to measure the deflection as a function of input power in vacuum and at 1 atmosphere. Results are shown in Figure 6.26. The deflection efficiency is 4.3 μm/mW in air and 18.3 μm/mW in vacuum, and the heat loss ratio is 4.25.

The two structures with heater inside and outside the cantilever have been compared. Results show that the outside heater structure consumes about 4.25 times more energy in air than that in vacuum in order to move same deflection because of heat loss directly to air; however, the inside heater structure only consumes 2 times more thermal energy in air than in vacuum. It is clear that having the heater inside the cantilever produces significantly less heat loss in air, although in vacuum the outside heater configuration is probably more efficient; the greater efficiency is most likely caused by the faster heating of the high-thermal expansion element.

Figure 6.22 Photo showing the inside heater structure.

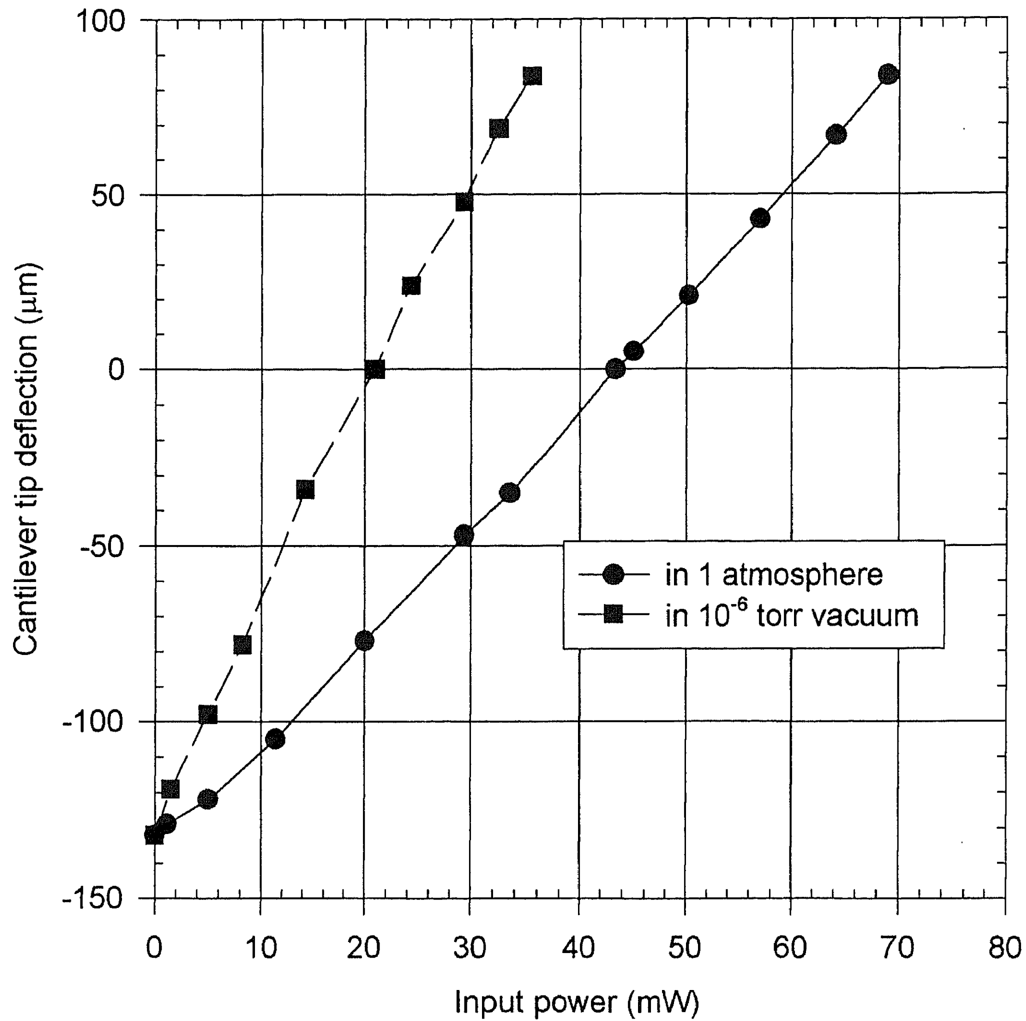

Figure 6.23 Tip deflection vs. applied power inside SEM vacuum and in air for Al-SiO_2 cantilever with heater inside. Cantilever length L=400μm, width W=50μm and t_{Al}=1.5 μm.

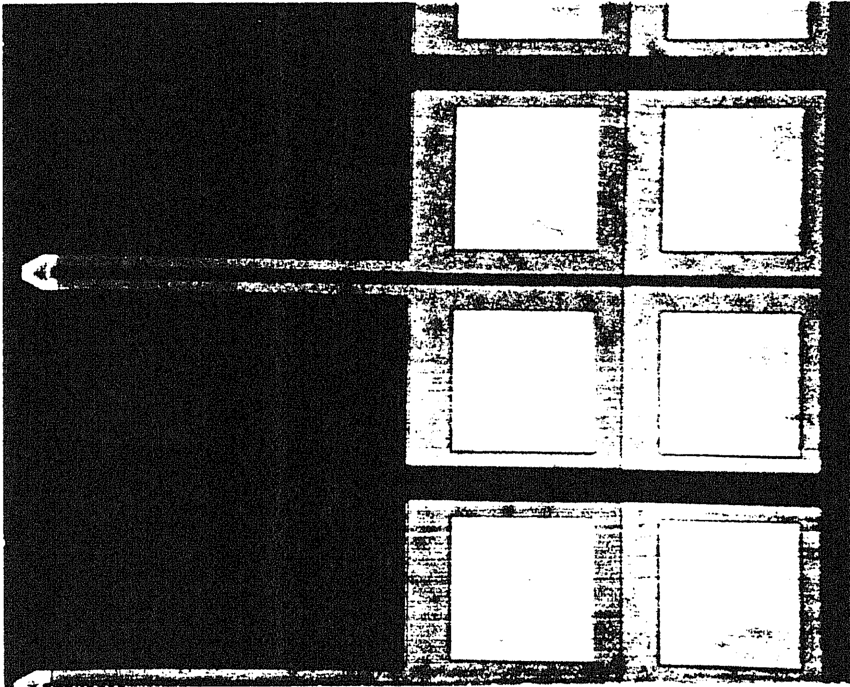

Figure 6.24 Photo showing the outside heater structure.

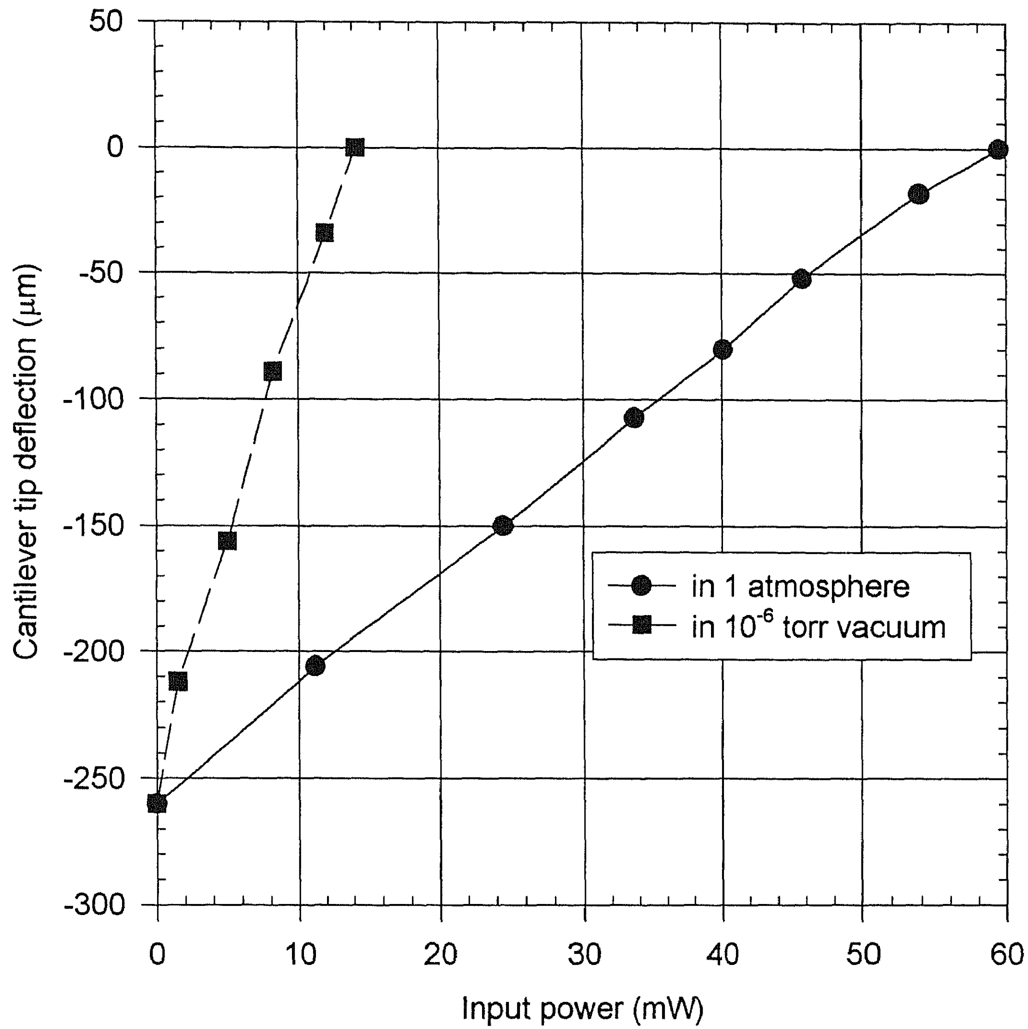

Figure 6.25 Tip deflection vs. applied power inside SEM vacuum and in air for Al-SiO_2 cantilever with heater on the bottom. Cantilever length L=500μm, width W=40μm and gap D=10 μm.

6.5 Failure Analysis and Device Improvement

During the ohmic contact experiments some contact tip failures caused. One failure happened during the dynamic switch test with the cantilever actuated with a square wave signal at 10 Hz to contact a W probe tip. The momentum is quit large during the contact because of the small actuation time. During dynamic testing (while video recording) the tip suddenly broke. Figure 6.26 shows a TV frame just after breaking. Figure 6.27 shows the same cantilever with the tip still weakly connected. From the TV raster frequency we know the tip break happened within a time period $\Delta t < 33$ ms. Because the fatigue must have gradually occurred before the break, this suggest the break must happen at the weakest point of the cantilever. The tip break happened right in the boundary between the gold tip and LTO layer. This was likely caused by the fact that the gold was deposited through a window at the cantilever tip using a lift off; the mask for gold lift-off was designed with the same size as the tip opening, so that there may have been a small gap due to mask alignment error. As a result this very thin region at the boundary becomes the weakest point of the cantilever. A large overlap structure between the lift-off gold and LTO is suggested for future design to solve this problem.

Additionally, a thick thermal steam oxidation film is also suggested to replace the Si_3N_4\LTO film for the KOH stop layer, because the Si_3N_4 film has too much stress and is easy to break when the KOH almost penetrates the silicon wafer. A thermal oxidation film has small stress and etches slowly in KOH.

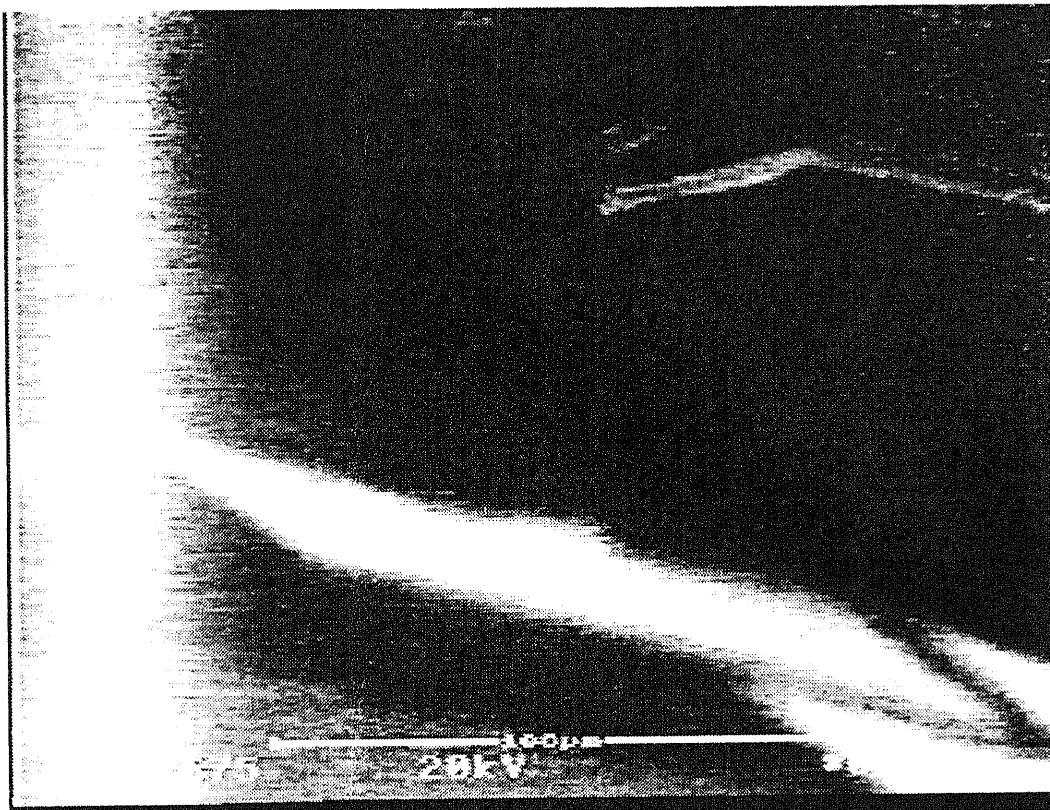

Figure 6.26 SEM photo showing a tip immediately after breaking.

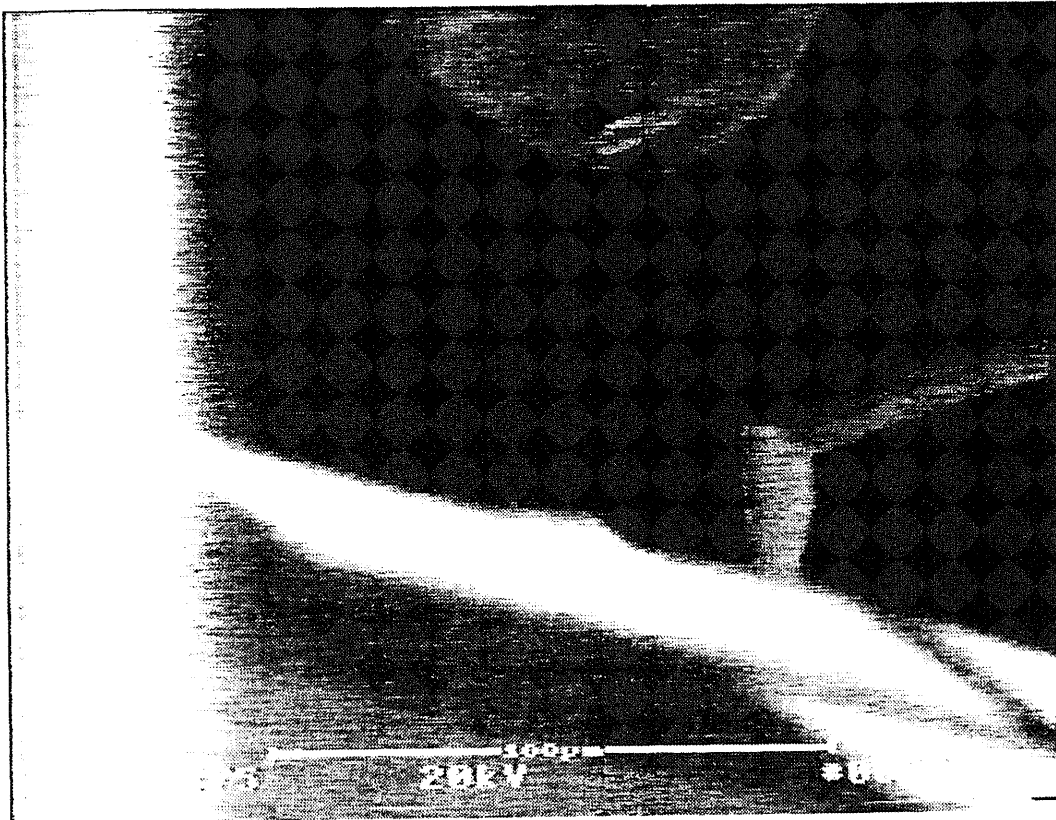

Figure 6.27 SEM photo showing the same tip as Figure 6.26 a 33 ms later.

CHAPTER 7

CONCLUSIONS

A new wafer probe card concept is presented which consists of an array of microcantilevers actuated by bimorph heating to make contact with the contact pads on a device chip during wafer-stage testing. Bending action is created through Joule heating of bimorph elements. The microcantilevers are meant to be operated either in air or in vacuum. The results has been summarized as follows:

1. The deflection efficiency $d\delta/dP$ ranges from 5.23-9.6 μm/mW (depending on lever parameters) for Al-SiO_2 bimorph cantilevers with 1.0 μm Al thickness and 2.4-2.8 for W-SiO_2 cantilevers with 1 μm thickness.
2. The force efficiency dF/dP ranges from 1.4 to 5.5 μN/mW for Al-SiO_2 cantilevers.
3. A full deflection (134 μm) occurs in response to input frequency up to 120 Hz, motion being to dampen at higher frequency, and the cantilever resonant frequency was found at 6.48KHz.
4. Heat loss for devices operating in air was found to be substantially higher than for vacuum operation. A heater inside the cantilever structure can be used to reduce the heat loss. Heat ratio is about 2:1 for operating in air and in vacuum with a heater inside structure; the ratio is 4.25:1 with a heater on the cantilever surface. An outside heater arrangement is probably more efficient for vacuum operation.
5. The maximum controllable (reversible) deflection is in the range of 200-300 μm for Al-SiO_2 cantilevers, and 100-150 μm for W-SiO_2 cantilevers.

6. Contact resistance with gold-gold contact is approximately 0.25-0.5 Ω for a $W\text{-}SiO_2$ cantilever, and 0.8-1 Ω for $Al\text{-}SiO_2$ cantilever. The contact resistance with conducting diamond is about 100 Ω.

These studies show that the CHIPP microactuator structures designed, made and evaluated in this research can be used to make CHIPP probe cards. The CHIPP probe card can be used for industry applications requiring a high pin count and high density features, and the ability to contact test pads with varying heights with a on/off speed greater than 33 ms. These features provide a new way to perform VLSI wafer stage testing, and could represent a new future for VLSI testing.

REFERENCES

[1] B. Newboe, "The probe card dilemma," *Semiconductor International*, pp. 64, September, 1992.

[2] R. Iscoff, "What's in the cards for wafer probing," *Semiconductor International*, pp. 76, June 1994.

[3] Accuprobe Inc., http://www.accuprobe.com.

[4] M. Beiley, and S. Wong, "Micro-machined array probe card", in *Proceedings of International Test Conference*, pp. 896, 1992.

[5] M. Beiley, and S. Wong, "Micro-machined array probe card", in *Proceedings of International Electron Devices Meeting*, pp. 509, 1992.

[6] M. Beiley, J. Leung and S. Wong, "A micromachined array probe card-fabrication process", *IEEE Transactions on Components, Packing, and Mafufacturing Technology*-Part B, vol 18, No. 1, pp. 179, 1995.

[7] M. Beiley, J. Leung and S. Wong, "A micromachined array probe card-characterization", *IEEE Transactions on Components, Packing, and Mafufacturing Technology*-Part B, vol 18, No. 1, pp. 184, 1995.

[8] Tada, et. Al., *Proceedings of International Test Conference*, pp900, 1990.

[9] R. B. Marcus and W. Carr, "Microprobe", U.S. Patent #5,475,318.

[10] Y. Zhang, Y Zhang, D. Worsham, D. Morrow and R. B. Marcus, "A new MEMS wafer probe card," in *Proceedings of IEEE 10th International workshop on MEMS*, Nagoya, Japan, Jan. 26-30, pp. 395-399, 1997.

[11] A. S. Brown, "MEMS: macro growth for micro systems", *Aerospace America*, pp32, Oct. 1994.

[12] R. Nass, "Tiny accelerometer IC reaches high sensitivity," *Electronic Design*, pp. 170, Sept., 1988.

[13] J. M. Younse, "Mirrors on chip", *IEEE Spectrum*, pp. 27, Nov., 1993.

[14] H. Fujita, "A Decade of MEMS and Its Future," Proceedings of IEEE 10th International workshop on MEMS, Nagoya, Japan, Jan. 26, pp. 1-8, 1997.

[15] W. Riethmuller and W. Benecke, "Thermally excited silicon micro-actuators", *IEEE Transactions on Electron Devices*, vol. 35, No.6, pp. 758, 1988.

[16] W. Benecke and W. Riethmuller, "Applications of silicon-microactuators based on bimorph structures," *Proceedings of IEEE MEMS Workshop*, pp. 116, Salt Lake City, Utah, 1989.

[17] Takeshima and H. Fujita, "Polyimide bimorph actuators for a ciliary motion system"' *Micromechanical Sensor, Actuators, and Systems* (DSC-vol.32), ASME Winter Annual Meeting, pp. 203-209, Atlanta GA, Dec. 1991.

[18] W-H. Chu, M. Mehregany, and R. L. Mullen, "Analysis of tip deflection and force for a bimetallic cantilever microactuator," *J. Micromech. Microeng.*, vol.3, pp. 4, 1993.

[19] H. Matoba, T. Ishikawa, C-J. Kim, and R. S. Muller, "A bistable snapping microactuator," in *Proceedings of IEEE MEMS*, pp. 45, Oiso, Japan, January 25-28, 1994.

[20] H. Guckel, J. Klein, T. Christeson, K. Skrobis, M. Laudon and E. G. Lovell, "Thermo-magnetic metal flexure actuators," in *Proceedings of Transducers'92*, San Fransisco, CA, pp. 73, June, 1992.

[21] S. F. Bar, T. A. Lober, R. T. Howe, J. H. Lang, and M. F. Schlecht, "Design considerations for micromachined electric actuators," *Sensors and Actuators A*, vol. 14, pp. 269, 1988

[22] K E. Peterson, "Dynamic micromechanics on silicon: technique and devices," *IEEE Transactions on Electron Devices*, vol. ED-25, pp. 1242, 1978.

[23] C. Linder, L. Paratte, M-A Grretillat, V. P. Jaecklin, and N. F. de Rooij, "Surface micromachining," *J. Micromech. Microeng.*, vol. 2, pp. 122, 1992

[24] J. J. Yao and M. F. Chang, "A surface micromachined miniature switch for telecommunications applications with signal frequencies from DC to 4 GHz," *IEEE Transducers'95 Eurosensors IX*, pp. 34, 1995.

[25] C. Linder, and N. F. de Rooij, Investigations on free-standing polysilicon beams in view of their application as transducers, " *Sensors and Actuators A*, vol. A21-A23, pp. 1053, 1990

[26] Drake, H. Jerman, B. Lutze, and M. Stuber, "An electrostatically actuated micro-relay," *The 8th International Conference on Solid-State Sensors and Actuators, and Eurosensors IX*, pp. 380, Stockholm, Sweden, June 25-29, 1995.

[27] S. Bouwstra, H. A. C. Tilmans, A. Selvakumar, and K. Najafi, "Base driven micromechanical resonators," *IEEE Trans. On Electron Devices*, ED-14, pp. 148, 1992.

[28] P. Osterberg, H. Yie, X. Cai, J. White, and S. Senturia, "Self-consistent simulation and modeling of electrostatically deformed diaphragms," *IEEE MEMS'94*, Japan, 1994.

[29] H. Hosaka, H. Kuwano, and K. Yanagisawa, "Electromagnetic micro relays: concepts and fundamental characteristics," *Sensors and Actuators A*, vol. 40, pp. 41, 1994.

[30] F. Cardol, J. Gobet, M. Bogdanski, and F. Rudolf, "Fabrication of a magnetic transducer composed of a high-density array of microelectromagnets with on chip electronics," *Sensors and Actuators A*," vol. 43, pp. 11, 1994.

[31] J. W. Judy, D. L. Polla, and W. P. Robbins, "a linear piezoelectric stepper motor with submicron step size and centimeter travel range," *IEEE Trans. On Ultrasonic, Ferroelectrics, and Frequency Control*, Vol. 37, No. 5, pp. 428-437, Sept., 1990.

[32] T. Tamagawa, D. L. Polla, and C. C. Hsueh, "Lead zirconate titanate (PZT) thin films in surface-micromachined sensor structures," *IEEE International Electron Device Meeting*, San Francisco, CA, Dec. 1990.

[33] H. Fujita, and K. J. Gabriel, "New opportunities for micro actuators," *IEEE Trans. On Electron Devices*, ED-35, pp. 14-20, 1991.

[34] S. Wolf and R. N. Tauber, *Silicon Processing for the VLSI Era*, Lattices Press, CA, 1986.

[35] C. Belove, *Handbook of Modern Electronics and Electrical Engineering,* Wiley, New York, NY, *1987.*

[36] *H. Bruce, American Institute of Physics Handbook,* Third Edition, McGraw Hill Inc., NY, 1972.

[37] *W. R.. Veazey, Handbook of Chemistry and Physics*, 58th Edition, CRC Press, Cleveland, OH, 1978.

[38] Solid State Measurements, Inc., Pittsburgh, PA.

[39] R. G. Mazur, in *Symposium on Materials Characterization in Microelectronics Processing* (The American Chemical Society), St. Louis, MO, April 9, 1984

[40] H. Hosaka, H. Kuwano and K. Yanagisawa, *IEEE MEMS'93*, pp. 12, 1993.

[41] J. Beale and R. F. W. Pease, *IEEE Elect-Contact*. Vol. 17, pp.45, 1994.

[42] J. E. Herlinger, sp^3, Inc., Mountain View, CA 94041.

[43] S. Timoshenko, "Analysis of bi-metal thermostats," *Journal of the Optical Society of America Review of Scientific Instruments*, vol. 11, pp. 233, 1925.

[44] Warren. C Young, *Roark's Forlulas for Stress & Strain*, McGraw-Hill Book Co. NY, pp.117, 1989.

[45] S. P. Timoshenko, *Mechanics of Materials*, 1972.

[46] G. Zheng and W. Carr, "Internal stress of thin bimorph microengineered structure", *Proceedings of the Third International Conference-Materials and Process Characterization for VLSI*, Kunming, China, pp. 498, 1994.

[47] S. M. Sze, *Semiconductor Sensors*, John Wiley & Sons, Inc., NY, 1994